


International School for Advanced Studies
Trieste

**DENSITY FUNCTIONAL THEORY OF FREEZING:
SOME APPLICATIONS**

*Thesis submitted for the degree of
"Doctor Philosophiae"*

CANDIDATE
Zeenet Badirkhan

SUPERVISOR
Prof. M.P. Tosi



October 1990

بِسْمِ اللَّهِ الرَّحْمَنِ الرَّحِيمِ

*To the memory of Kamran,
to Wafa', and all my family.*

Contents

INTRODUCTION	iii
1 THE MELTING / FREEZING TRANSITION: STRUCTURAL CRITERIA AND THEORETICAL AP- PROACHES	1
Introduction	2
1.1 Empirical Criteria for Freezing and Melting	3
1.2 Freezing for Model Systems with Inverse-Power Repulsive Potentials	6
1.3 Theories of Melting and Freezing	11
1.4 Density Functional Approach to Liquid Solid Coexistence . .	16
1.5 Application of the Density Functional Approach to the Hard Sphere System	18
1.5.1 Cluster Expansion and its Truncation (TCE)	18
1.5.2 Effective Liquid Approximation (ELA)	22
1.5.3 Weighted Density Approximation (WDA)	24
1.5.4 Parametrization of the Density Profile	27
1.6 Some Other Applications of the Density Functional Approach	28
1.6.1 Freezing of Soft Spheres and of the One Component Classical Plasma	28
1.6.2 Freezing of the Lennard-Jones System	32
1.6.3 Freezing of Alkali Halides and Binary Alloys	34
1.6.4 Freezing and Superionic Transition In $SrCl_2$	41
1.6.5 Extension to Shear Deformed and Dislocated Crystals	43
2 FREEZING OF A CLASSICAL PLASMA AND OF ALKALI METALS	46
Introduction	47
2.1 Classical One-Component Plasma as a Reference System . . .	49
2.2 Thermodynamic Potentials	59
2.3 The Density Functional Formalism	60
2.4 Density Functional Theory of Freezing	65
2.4.1 Entropy and Volume Changes Across the Phase Tran- sition	68
2.4.2 Gaussian Width and Lindemann's Ratio	71

2.5	Freezing of One-Component Plasma on a Rigid Background (OCP-RB)	72
2.5.1	Results with Exclusion of Equilibrium Equation for ρ_{G_2}	75
2.5.2	Calculations with Inclusion of ρ_{G_2}	78
2.5.3	Freezing of OCP-RB Into the F.c.c. Structure	80
2.6	Freezing of OCP on a Deformable Background (OCP-DB)	82
2.7	Freezing of Alkali Metals	89
3	FREEZING OF A BOND-PARTICLE MODEL FOR LIQUID GERMANIUM	94
	Introduction	95
3.1	Introduction to the Structure of Covalently Bonded Systems	96
3.1.1	Some Basic Experimental Facts Concerning Structure	100
3.1.2	Theoretical Approaches	104
3.2	Bond-Particle Model for Elemental Semiconductors	107
3.2.1	Bond-Charge Model for Lattice Dynamics	107
3.2.2	Melting of Elemental and III-V Semiconductors	112
3.2.3	Bond-Particle Models for Liquid Structure	113
3.3	Qualitative Discussion of Freezing of a Bond-Particle Model	117
3.4	Density Wave Theory of Freezing for a Bond-Particle Model	120
3.4.1	Pearson-Rushbrooke Relations and Bahatia-Thornton Structure Factors for Two Component Systems	120
3.4.2	Density Wave Theory of Freezing for a Two Component System	122
3.4.3	Results and Discussion	124
3.5	Evaluation of Freezing for a Liquid Having the Structure of Amorphous Germanium	130
	Summary	134
	Bibliography	136

INTRODUCTION

The present work is concerned with applications of the density functional theory of the liquid-solid equilibrium transition to various systems: (i) freezing of a classical one-component plasma and of alkali metals and (ii) freezing of a bond-particle model for elemental semiconductors, in particular for liquid germanium.

During the past decade, the density functional theory (DFT) has demonstrated its usefulness in relation to understanding the liquid-solid phase coexistence for a variety of systems. The main idea behind the DFT of freezing is that a good semiquantitative description of the thermodynamic properties of the solid phase can be obtained by using only structural properties of liquid phase as input. Knowledge of the free energies in both phases constitutes the basic prerequisite for solving the coexistence aspect of the phase transition problem. At the same time, the theory puts emphasis and physical interpretation behind empirical criteria for the phase transition, in particular the Lindemann criterion for melting and the Hansen-Verlet criterion for freezing. Many earlier attempts using different approaches have been devoted to predicting the conditions under which a solid will melt or a fluid will freeze, often regarding the first-order phase transition as if it were arising from an instability in either the liquid or the solid phase. The DFT can bypass most of the difficulties of these traditional approaches by expressing the thermodynamic potential of any system (say, liquid or solid) in terms of (i) its one-body density $\rho(\mathbf{r})$, which exhibits the system's observable symmetries, and (ii) its two-body direct correlation function $c(\mathbf{r}, \mathbf{r}'; [\rho])$, which plays the role of an effective pair potential self-consistently determined by $\rho(\mathbf{r})$ through its dependence (indicated by the square brackets) on the latter. Approximations must, of course, be brought in to concretely handle the above direct correlation function in practical calculations.

In this work, chapter 1 presents some basic experimental and theoretical facts concerning the freezing/melting phase transition. We start from the empirical rules for freezing and melting which have been developed for each individual phase, and the important relations that characterize the thermodynamics of the transition in model systems with inverse-power repulsive potentials. The various theories concerning this phenomenon are also summarized. The basic points of the density functional approach to liquid-solid coexistence are briefly reported, with main emphasis on the study of the hard-sphere systems by this approach and on the different approximations used in applications of the theory.

The DFT approach to crystallization is applied in chapter 2 to the freezing of the classical one-component plasma (OCP) and of alkali metals.

Freezing of the classical plasma on a rigid neutralizing background into the bcc structure is re-evaluated, taking account of the recent progress in the determination of the thermodynamic properties of this model fluid by computer simulation and of the known difficulties of the theory relating to the order parameter at the (200) star of reciprocal lattice vectors. Freezing into the fcc structure is also considered and found to be unfavoured.

The relationship between Wigner crystallization in the classical plasma and the liquid-solid transition of alkali metals is also examined in the same chapter. We show that on allowing for long-wavelength deformability of the background, the appearance of volume change on freezing into the bcc structure is accompanied by reduced stability of the fluid phase and by an increase in the entropy of melting. Freezing of alkali metals into the bcc structure is also evaluated, taking their ionic pair structure as that of an ionic plasma reference fluid screened by conduction electrons and asking that the correct ionic coupling at liquid-solid coexistence should be approximately reproduced. The values of the volume and entropy changes across the phase transition, as estimated from the theory by two alternative routes, are in reasonable agreement with the experiment. The order parameters of the phase transition, excepting the (200) one, conform rather closely to a Gaussian behaviour and yield a Lindemann ration in reasonable agreement with the empirical value for melting of bcc crystals.

Freezing of a bond-particle model for liquid germanium is evaluated in chapter 3. In a short introduction to the structure of covalently bonded systems in crystalline and disordered (liquid or amorphous) states, we recall some of the basic experimental facts relating mainly to medium-range order in the disordered states of these materials. Various theoretical approaches are also discussed, where we have introduced the bond-particle model and its early uses in lattice dynamics. The melting criteria which follow from the bond-particle model and its use in evaluation of the liquid structure are presented as a starting point to discuss the process of equilibrium freezing qualitatively, and to evaluate phase coexistence within the framework of the density wave theory of freezing. Finally, we report our evaluation of freezing for a liquid having the structure of amorphous germanium.

Chapter 1

THE MELTING/FREEZING TRANSITION : STRUCTURAL CRITERIA AND THEORETICAL APPROACHES

INTRODUCTION

The aim of this introductory chapter is to present some basic experimental and theoretical facts concerning the freezing/melting phase transition. Section 1 briefly reviews empirical criteria for freezing and melting, namely the Lindemann rule, the Ross rule and the Hansen-Verlet rule. The criteria are based on the 'universality' of the information gained from laboratory and computer experiments. These are one-phase approaches, in which one starts from the knowledge of the properties of one of the two phases (the solid or the liquid phase) and tries to predict from them the occurrence of the phase transition.

Section 2 deals with some important relations that characterize the thermodynamics of the transition in model systems with inverse-power repulsive potentials, along with recent results of computer simulation.

In section 3 we summarize various theories of melting and freezing, relating melting to 'avalanche' generation of lattice defects and freezing to the short-range order that is present in the liquid. A first-order melting transition was successfully predicted on the basis of a dislocation model by Edwards and Warner. The prediction of the solid-like state from the knowledge of the liquid distribution function was initiated by Kirkwood and Monroe, followed by many other authors who studied various systems of integro-differential equations. Finally, the first attempt towards the establishment of a density functional approach were made by Lovett and Buff.

The basic points of the density functional approach to liquid-solid coexistence are briefly discussed in section 4, whereas the application of this approach to the hard-sphere system is examined in section 5. Here we briefly review the main different approximations in the application of the theory, i.e. the cluster expansion, the effective-liquid approximation, the weighted-density approach and the parametrization of the density profile.

Finally, section 6 briefly covers applications of the density functional approach to other systems, namely the soft spheres and the one-component classical plasma, the Lennard-Jones system, alkali halides and binary alloys, and superionic fluorites in the example of $SrCl_2$. We conclude by recalling the extension of the theory to shear-deformed and dislocated crystals.

1.1 Empirical Criteria for Freezing and Melting

The freezing/melting transition has attracted attention for a long time and up to the present days. In this section we shall briefly survey some of the empirical rules that were proposed by various authors in different contexts.

In 1910 Lindemann¹ proposed his rule stating that along the melting curve the ratio between the root-mean-square displacement of a particle from its lattice site and the first-neighbour distance, $L = \sqrt{\langle(\Delta u)^2\rangle}/d$, is constant. It turns out that this ratio is about 10% for many different elements.

From an experiment point of view, it should be noted that, at least within the harmonic approximation, the above mean-square displacement is related to the well known Debye-Waller factor, measuring the intensity of the Bragg diffraction spots of the crystal as a function of temperature. Indeed, the harmonic approximation yields the intensity of the selective Bragg reflections as

$$I \propto \exp[-1/3\langle(\Delta u)^2\rangle |\mathbf{G}|^2] \quad , \quad (1.1.1)$$

where \mathbf{G} is the appropriate reciprocal lattice vector of the crystal. The exponential in eqn.(1.1.1) is known as the Debye-Waller factor and conventionally written as e^{-2W} ². Classically, if one expresses the crystal in the harmonic approximation, the mean-square displacement is

$$\langle(\Delta u)^2\rangle = \frac{9k_B T}{Mw^2}$$

where M is the atomic mass and w is the frequency of the oscillating atom, which can be expressed in terms of the Debye temperature Θ_D , i.e. $hw_D/k_B T \equiv \Theta_D/T$, then the Debye-Waller factor can be related to accessible experimental parameters as³

$$2W = \frac{3\hbar^2 G^2 T}{MK_B \Theta_D^2} \quad . \quad (1.1.2)$$

Hence, the Lindemann ratio at melting is

$$L = \frac{3\hbar}{d\Theta_D} \left(\frac{T_m}{MK_B}\right)^{1/2} \quad . \quad (1.1.3)$$

Table (1.1) shows the value of L calculated using eqn.(1.1.3)⁴ and from a full lattice-dynamics calculation⁵ for certain elements, as well as the value of the Debye-Waller factor for the alkali metals at the first reciprocal lattice point⁶, based on a standard harmonic-lattice calculation which uses values of the inverse second moment of the phonon spectrum^{7,8}.

<i>Elements</i>	L^4	L^5	e^{-2w}
B.C.C.			
Li	0.125	0.116	0.64
Na	0.119	0.111	0.66
K	0.125	0.112	0.65
Rb		0.115	0.67
Cs		0.111	0.63
F.C.C.			
Al	0.100	0.072	
Cu	0.117	0.069	
Ag	0.105	0.071	
Au	0.100	0.073	
Pb	0.111	0.065	

Table 1.1: Values of the Lindemann ratio L for some B.C.C. and F.C.C. elements calculated in two different roots from ref.[4,5], and the Debye-Waller factor for the alkali metals near melting from ref.[6].

The Lindemann melting rule was extended by Ross ⁹ in terms of the statistical mechanical partition function. With his reformulation, Ross considered the excess part of a free energy, F_{ex} , and concluded that this should be constant along the melting curve. That is

$$\frac{F_{ex}}{Nk_B T} = \frac{F}{Nk_B T} - \ln \frac{N}{V} + 1 - \frac{V_o}{Nk_B T} \equiv const. . \quad (1.1.4)$$

Where F is the free energy of the solid and V_o is the potential energy of the solid if all the particles are fixed at their lattice sites. This equation is actually exact for the inverse power repulsive potentials, and has been tested by Hoover et al ¹⁰ as a function of the softness of the interaction. It was found that $F_{ex} \simeq 6Nk_B T$ in all different cases, as can be seen in Fig. 1.1.

From the above discussion, it is clear that the two approaches to melting that we have discussed consider only one phase, i.e. they treat the solid and say nothing about the liquid. A freezing criterion based on the liquid structural properties of the liquid phase has instead been formulated by Hansen and Verlet ¹¹. They have obtained a simple ‘law’ for crystallization, which states that along the freezing curve the height of the main peak of the liquid static structure factor, $S(k)$, is constant. This constant reaches the value $S(k_{peak}) = 2.85$ for the Lennard-Jones system. Finally, the liquid structure factors at melting for fluids of particles interacting through the inverse-power repulsive potentials, to be discussed in more detail in the following section (1.2), have been studied by Hansen and Shiff ¹², generalizing

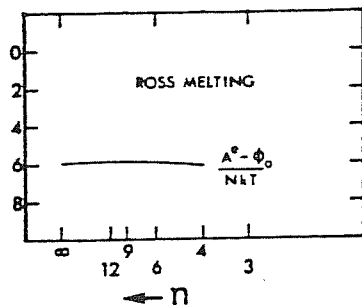


Figure 1.1: Ross's melting rule as a function of softness of the inverse power potential, which indicates a proportionality constant $6Nk_B T$. From ref. [10].

the crystallization criterion of the Lennard-Jones system to systems with $n = \infty$ ($S(k_{peak}) = 2.85$), $n=12$ ($S(k_{peak}) = 3.05$), $n=6$ ($S(k_{peak}) = 2.99$), and finally $n=1$ ($S(k_{peak}) = 2.57$). Table 1.2 shows the experimental values of $S(k)$ at the first peak for various elements near freezing ¹³, and the corresponding values of the direct correlation function $c(k)$ which is related to $S(k)$ through $S(k) = [1 - c(k)]^{-1}$.

Elements	$S(k)$	$c(k)$
B.C.C.		
Li	2.64	0.62
Na	2.80	0.64
K	2.73	0.63
Rb	2.80	0.64
Cs	2.50	0.60
F.C.C.		
Al	2.48	0.60
Cu	2.53	0.61
Ag	2.59	0.61
Au	2.49	0.60
Pb	2.42	0.59

Table 1.2: experimental values of $S(k)$ at the first peak for some B.C.C. and F.C.C. elements near freezing, and the corresponding values of the direct correlation function $c(k)$. From ref.[13]

1.2 Freezing for Model Systems with Inverse-Power Repulsive Potentials

The liquid-solid transition is a first order phase transition, and the pioneering work of Alder and Wanwright¹⁴ on hard-sphere and hard-disk systems showed that freezing is essentially governed by the repulsive part of the potential, while the attractive part (though crucial for the liquid-vapour transition) is not crucial for freezing. A simple generalization of hard-sphere system is the 'soft-sphere' model of atoms interacting through purely repulsive inverse-power potentials: (fig. 1.2)

$$\phi = \epsilon \left(\frac{\sigma}{r} \right)^n, \quad (1.2.1)$$

in which ϵ and σ are constants with the dimensions of energy and length and r is the distance between particles. The steepness of the repulsion is governed by the exponent n : the two particularly interesting limiting cases are the hard-sphere model ($n = \infty$) and the classical one-component-plasma (OCP) of point ions interacting via the Coulomb potential ($n = 1$).

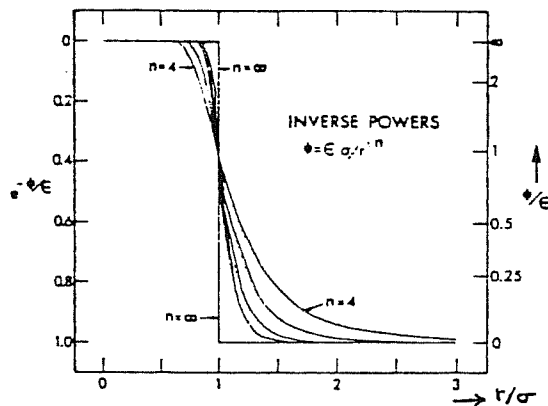


Figure 1.2: *Interparticle potential energy functions for five inverse power potentials, corresponding to $n=4,6,9,12$ and ∞ . From ref [10].*

An inverse-power potential actually introduces simple scaling property, reducing the number of independent thermodynamic variables from two (volume and temperature, say) to one, $x = \rho \left(\frac{\epsilon}{k_B T} \right)^{3/n}$ with $\rho \equiv \frac{N}{V} \sigma^3$ (Klein's theorem^{15,16}). Indeed, the canonical function can easily be written in terms of a reduced distance $s = r \left(\frac{N}{V} \right)^{1/3}$, given by

$$Z(T, V, N) = \frac{V^N}{N! \lambda^{3N}} \int \int \exp \left(-\rho^{3/n} \frac{\epsilon}{k_B T} \sum_{i,j} s_{i,j}^{-n} \right) ds_i ds_j, \quad (1.2.2)$$

where $\lambda = \left(\frac{h^2}{2\pi m k_B T} \right)^{1/2}$, and then all thermodynamic properties obtained by differentiating the partition function $Z(T, V, N)$, depend only on the

variable x ¹⁷. If one introduces z_s and z_l for the corresponding pure-phase compressibility factors, $(\frac{PV}{Nk_B T})_s$ and $(\frac{PV}{Nk_B T})_l$ in the solid and liquid phase. A state equation of the form

$$z_i = 1 + \Phi_i \left(\rho \left(\frac{\epsilon}{k_B T} \right)^{3/n} \right) , \quad (1.2.3)$$

follows, where i stands for either s (solid) or l (liquid).

The liquid-solid coexistence curve is then entirely determined by two universal values of x , for the solid (x_s) and for the liquid (x_l), given by

$$x_s = \rho_s \left(\frac{\epsilon}{k_B T} \right)^{3/n} , \quad x_l = \rho_l \left(\frac{\epsilon}{k_B T} \right)^{3/n} . \quad (1.2.4)$$

Here ρ_s and ρ_l are the density of the solid and liquid phase, respectively. The equation of the melting curve and the volume and entropy discontinuities across the phase transition can be expressed in terms of x_i and z_i , i.e. by combining eqns.(1.2.3) and (1.2.4):

$$\frac{P\sigma^3}{\epsilon} = \left(\frac{k_B T}{\epsilon} \right)^{n+3/n} z_i x_i \quad (1.2.5)$$

$$\frac{\Delta v}{v} = \text{constant} \quad (1.2.6)$$

$$\frac{\Delta S}{R} = \text{constant} . \quad (1.2.7)$$

In the case of hard spheres, the relations (1.2.6) and (1.2.7) remain unchanged, while relations (1.2.4) and (1.2.5) become

$$x_s = \rho_s \quad ; \quad x_l = \rho_l \quad (1.2.8)$$

and

$$P = \text{const.} \times T . \quad (1.2.9)$$

In the other extreme case, i.e. the OCP (system of point-like charged particles embedded in a uniform background), the canonical partition function becomes

$$Z(T, V, N) = \frac{V^N}{N! \lambda^{3N}} \int \int \exp(-\Gamma \eta(s_1, \dots, s_N)) ds_1 ds_N . \quad (1.2.10)$$

in which $\eta(s_1, \dots, s_N)$ is a function that characterizes the spatial arrangement of the ions, and the coupling constant Γ defined as

$$\Gamma = \frac{(Ze)^2}{ak_B T} , \quad (1.2.11)$$

which is a function that expresses the ratio between Coulomb energy and thermal energy with a being the radius of the sphere containing one ion ($a = (4\pi\rho/3)^{-1/3}$). The thermodynamics of the phase transition in the OCP is then determined by Γ parameter, with zero volume change and the density at the phase coexistence is given by

$$\rho_{s,l} \propto (k_B T)^3 . \quad (1.2.12)$$

The fluid-solid coexistence for the model systems mentioned above has been determined by computer simulation for several values of n , as well as for a system of particles interacting via a Lennard-Jones potential ^{11,18- 21} and for the OCP ^{22- 25}. In addition, the preceding thermodynamic relations have been proved for all the systems having different values of n ¹⁰.

In the thermodynamic theory of freezing, the Gibbs free energy of the two phases at coexistence should be the same at equal pressure and temperature. From computer experiments the free energies of the two phases cannot be calculated directly, and will also depend on the number of particles included in the run, since the fraction of particles in the interface between the two phases is of the order $N^{2/3}$, which is not negligible for the systems that can be studied with the computer. So, in order to determine the free energy one has to start from a reference system in which the free energy is exactly known (for instance, the ideal gas) and then calculate the free energy difference between the free energy of the liquid (or solid) phase and that of the reference system.

Hoover and Ree ²⁶ were able to locate two-phase coexistence by developing an efficient method, where the reference system is the ideal gas and the solid is artificially stabilized at low densities by dividing the whole volume into Wigner-Seitz cells, and imposing that only one particle should occupy each cell. In fig. 1.3 the thermodynamic equations of state for three inverse power potentials is shown, and in fig. 1.4 the phase boundaries for the same systems. It is evident that the melting and freezing densities for hard spheres ($n = \infty$) are temperature independent, as expected from equation (1.2.8).

Fig. 1.5 shows the phase diagram of the Lennard-Jones system ($\Phi(r) = Ar^{-12} - Br^{-6}$). The region corresponding to the phase separation between liquid and vapour is generated by the introduction of an attractive part in the potential. The resulting freezing characteristics are summarized in table (1.3) for several of these model systems, along with the Lindemann ratio and the height of the structure factor at the first peak from computer simulation work ^{10,12,21,27,28}.

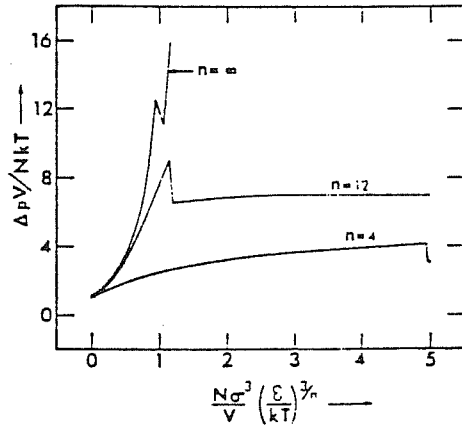


Figure 1.3: *Thermodynamic equations of state for three inverse power potentials from computer experiments. $\Delta PV/Nk_B T$ is the increase in the compressibility factor over that of a perfect static lattice at the same density and temperature. The discontinuities in the slopes of the three curves correspond to the melting and freezing transition. From ref [17].*

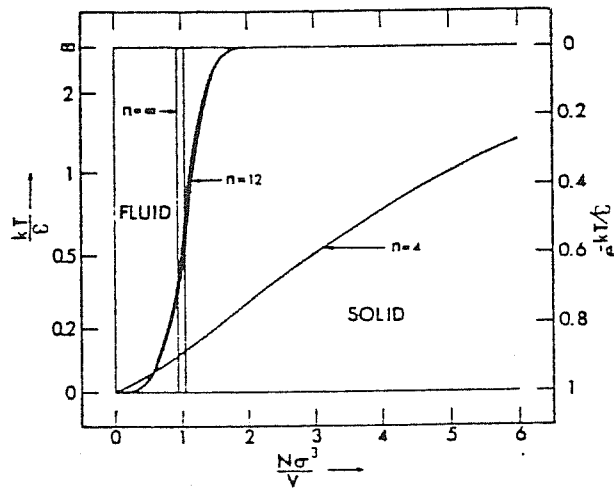


Figure 1.4: *Boundaries of the two phases, fluid and solid, for inverse power potentials. The narrow strips (clear for $n=\infty$. and black for $n=12$) correspond to the two phase region where fluid and solid can coexist. This region is very narrow for the case $n=4$. From ref [17].*

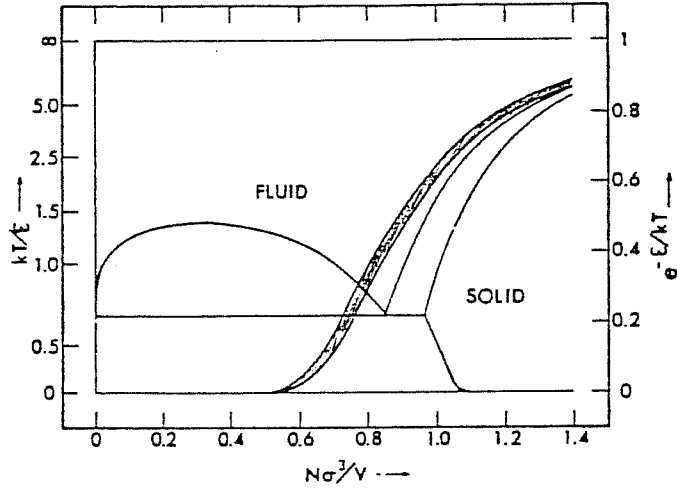


Figure 1.5: *The Lennard-Jones phase diagram. Superimposed on this diagram is the soft-sphere phase diagram resulting when only repulsive forces are used. The fluid-solid two-phase region for the soft-sphere potential is lightly shaded. From ref [17]*

n	x_l	x_s	$\Delta v/v 10\%$	$\Delta S/Nk_B T$	L	$S(k_{peak})$
∞	0.95	1.05	10.	1.16	0.14	2.90
12	1.14	1.19	3.8	0.90	0.15	3.05
9	1.33	1.37	3.0	0.84	0.16	3.02
6	2.17	2.21	1.3	0.75	0.17	2.99
4	5.53	5.57	0.5	0.80	0.18	2.70
1	Γ_{exp}	178	0.0	0.82	0.15	2.70

Table 1.3: *calculated parameters of the liquid-solid transition for different value of the steepness n . Where $x_l = \rho_l(\frac{\epsilon}{k_B T})^{3/n}$, $x_s = \rho_s(\frac{\epsilon}{k_B T})^{3/n}$ and the densities (ρ_l, ρ_s) are in units of (diameter)³. From ref. [27,28]*

In conclusion, one can summarize the general characteristics at freezing as follows:

- The relative volume change on melting, $\Delta v/v_s = (v_l - v_s)/v_s$, decreases with n , from $\simeq 10\%$ for the hard spheres system to zero in the case of OCP.
- The change in entropy at melting, $\Delta S/R$, is relatively insensitive to n .
- The lindemann ratio L is constant for a given potential and depends weakly on the steepness of the parameter n .
- The height of the main peak of the static structure factor $S(k)$ of the fluid is approximately constant along the freezing curve for a given potential and is nearly universal, i.e. essentially independent of the steepness n .

1.3 Theories of Melting and Freezing

As evident from the discussion in the preceding section, a theory of the liquid-solid phase transition can be developed for relatively simple systems by starting from assumed pair-wise interactions between the component atoms and evaluating the Helmholtz free energy and the pressure of the two phases. While such an evaluation is best done nowadays by computer simulation, various theoretical approaches have also been developed for such thermodynamic calculations in the literature. These usually require approximations of unclear relative accuracy for the two phases—for instance, one has to resort to the harmonic or weakly anharmonic approximation for the solid and to the several statistical mechanical approximations that are available for liquid structure and thermodynamics. Interesting results have nevertheless been obtained not only for Lennard-Jones-like systems such as argon, but also for simple liquid metals like sodium or aluminium.

Our main interest here, however, lies in the theoretical approaches that are directly related to the criteria for melting and freezing discussed in section (1.1). As already noted there, these are one-phase approaches, in the sense that one starts from knowledge of properties of one of the two phases and tries to predict from them the occurrence of the phase transition. In the early work along this direction the phase transition tended to be viewed as an instability of the phase being explicitly considered: for instance, an instability of the liquid phase would be signalled by the height of the main peak in the liquid structure factor diverging to infinity as a function of the thermodynamic state variables, or melting could be viewed as an instability of the solid phase arising from an avalanche production of crystalline defects like vacancies or dislocation ²⁹. Though a number of interesting ideas have

been emerged from this type of work, a single-phase instability is clearly in conflict with the experimental fact that the phase transition is of the first order. This basic aspect of the solid-liquid transition has been successfully incorporated in the more recent theoretical developments.

In relation to melting, we should like to briefly mention here the approach developed by Edwards and Warner³⁰, which was based on the idea that a liquid can be described in terms of a highly faulted solid. They successfully predict a first-order melting transition on the basis of a dislocation model in which a crucial contribution arises from mutual 'screening' in a dense of dislocations.

The main contribution to the free energy of a dislocation arises from the long-range elastic distortions induced in the material, but when dislocations of opposite Burgers vectors are brought together most of this distortion is eliminated. In fact, a dense assembly of dislocations can arrange itself so as to maximize this reduction. Edwards and Warner find that the free energy of the dislocation assembly can be expressed schematically as

$$F_d = \rho F_1 + \rho^2 F_2 - \rho^{3/2} F_{3/2} \quad , \quad (1.3.1)$$

where ρ is the length of dislocation lines per unit volume and F_i are temperature-independent coefficients. The first term on the right-hand side represents the core energy and the entropy of the dislocations, the second term is the energy associated with dilation induced by the dislocations, and the last negative term arises from many-dislocation effects representing reduction in the free energy due to 'screening' and leading to a first-order transition. This latter term is evaluated by writing the energy of interaction of two dislocation lines as

$$E_{12} \propto \int (\mathbf{b}_1 \cdot d\mathbf{l}_1)(\mathbf{b}_2 \cdot d\mathbf{l}_2)/r_{12} \quad , \quad (1.3.2)$$

where \mathbf{b}_i are the Burgers vectors, and by calculating the corresponding contribution to the partition function with techniques taken from the theory of networks of random walks. Introducing a dimensionless variable $y \propto \rho/T$, the free energy is calculated as a function of this variable y and has the form indicated in fig. 1.6 for various values of the temperature.

The melting temperature T_m is identified with the temperature at which the equilibrium condition $\partial F_d/\partial y = 0$ yields a finite concentration of dislocations with no excess free energy over the undislocated crystal ($F_d = 0$). The first-order character of the predicted transition is apparent from the fact that such a finite concentration of dislocations at equilibrium arises suddenly in the theory. Over a finite range of temperatures below T_m , one still has a local minimum of F_d at finite y , but corresponding to a metastable situation ($F_d > 0$), which may be thought to describe a supercooled liquid or a glass.

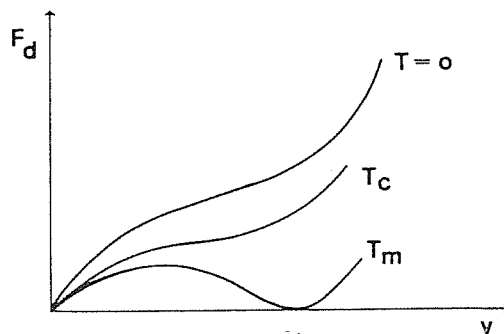


Figure 1.6: Qualitative shape of F_d in equation (1.3.1) vs $y \propto \rho/T$ for various values of T ; T_m is the melting temperature and T_c the lowest temperature for supercooling of the liquid (after Edwards and Warner[30]).

A freezing theory, which tries to predict the solid-like states from the knowledge of the liquid distribution function, is the Kirkwood- Monroe theory of the liquid-solid transition ³¹. This was based on the BBGKY hierarchy for inhomogeneous systems, which requires at the simplest level of approximation the knowledge of both the pair potential $V(r)$ and the homogeneous pair distribution function $g(r)$. They formulated their theory in the classical canonical ensemble and introduced an integral equation for a distribution function $\rho(\mathbf{r})$ specifying the average density at a point \mathbf{r} , as

$$\rho(\mathbf{r}) = \rho_l \exp\left[\int d\mathbf{r}' K_l(|\mathbf{r} - \mathbf{r}'|)[\rho(\mathbf{r}') - \rho_l]\right] , \quad (1.3.3)$$

where ρ_l is the density of the homogeneous phase. The kernel $K_l(|\mathbf{r}|)$ is evaluated in the liquid phase and contains both the pair potential and the pair distribution function, i.e.

$$K_l(|\mathbf{r}|) = \beta \int_{|\mathbf{r}|}^{\infty} d\mathbf{r}' g_l(\mathbf{r}') \frac{dV(r')}{dr'} . \quad (1.3.4)$$

For density distribution functions with the period of a specified lattice, the determination of periodic solutions of the integral eqn.(1.3.3) is equivalent to determining the solution of the set of transcendental equations for the Fourier coefficients $\rho_{\mathbf{G}}$ of the periodic distribution function $\rho(\mathbf{r})$,

$$\rho(\mathbf{r}) = \sum_{\mathbf{G}} \rho_{\mathbf{G}} \exp[i\mathbf{G} \cdot \mathbf{r}] , \quad (1.3.5)$$

where \mathbf{G} is a reciprocal lattice vector of the structure under consideration (the sum includes the case $\mathbf{G}=0$). The spirit of the approach is similar to the later density functional theory of freezing, which will be discussed in the following section (1.4) and chapter 2.

The stable periodic structure in the Kirkwood-Monroe theory was selected as the one of minimum Helmholtz free energy. The coexistence of the liquid and solid phases is determined with the aid of the thermodynamic criteria of heterogeneous equilibrium, i.e. the equality of the chemical potential and pressure in the two phase. Their theory predicts no critical point for the face-centered lattice and they conclude that within their framework the liquid-solid transition is of the first order.

The relation between the Kirkwood-Monroe theory and the modern theory of freezing has been discussed by Baus ⁷, who showed that the Kirkwood-Monroe theory misses a term related to the density derivative of the pair correlation function. Baus starts from the first member of the Yvon-Born-Green (YBG) hierarchy in the form

$$\nabla(\ln \rho(\mathbf{r}) + \beta\phi(\mathbf{r})) = -\beta \int d\mathbf{r}' \rho(\mathbf{r}') g(\mathbf{r}, \mathbf{r}') \nabla V(|\mathbf{r} - \mathbf{r}'|) \quad , \quad (1.3.6)$$

where $\rho(\mathbf{r})$ is the local number density and $\phi(\mathbf{r})$ is the external potential. Applying equation (1.3.6) to both the liquid phase having the singlet density ρ_l and the solid phase with the singlet density $\rho_s(\mathbf{r})$ in the limit of vanishing $\phi(\mathbf{r})$, one gets the following equation,

$$\nabla(\ln[\rho_s(\mathbf{r})/\rho_l]) = -\beta \int d\mathbf{r}' [\rho(\mathbf{r}') g(\mathbf{r}, \mathbf{r}') - \rho_l g(|\mathbf{r} - \mathbf{r}'|)] \nabla V(|\mathbf{r} - \mathbf{r}'|) \quad . \quad (1.3.7)$$

Expanding the difference in the right-hand side of (1.3.7) around the liquid as

$$\rho_s(\mathbf{r}) = \rho_l + \Delta\rho_s(\mathbf{r}) \quad (1.3.8)$$

$$g(\mathbf{r}, \mathbf{r}') = g_l(|\mathbf{r} - \mathbf{r}'|) + \int \left. \frac{\delta g(\mathbf{r}, \mathbf{r}')}{\delta \rho(\mathbf{r}'')} \right|_l \Delta\rho(\mathbf{r}'') + \dots \quad (1.3.9)$$

one obtains

$$\begin{aligned} \nabla(\ln[\rho_s(\mathbf{r})/\rho_l]) &= -\beta \int d\mathbf{r}' [g_l(|\mathbf{r} - \mathbf{r}'|) \Delta\rho(\mathbf{r}') + \\ &+ \rho_l \int d\mathbf{r}'' \left. \frac{\delta g(\mathbf{r}, \mathbf{r}')}{\delta \rho(\mathbf{r}'')} \right|_l + \dots] \nabla V(|\mathbf{r} - \mathbf{r}'|) \quad . \quad (1.3.10) \end{aligned}$$

With a proper choice of integration constant, eqn.(1.3.10) can be transformed in to

$$\rho_s(\mathbf{r}) = \rho_l \exp\left[\int d\mathbf{r}' K_l(|\mathbf{r} - \mathbf{r}'|) + H_l(|\mathbf{r} - \mathbf{r}'|) \Delta\rho(\mathbf{r}') \right] \quad , \quad (1.3.11)$$

where

$$\nabla K_l(|\mathbf{r} - \mathbf{r}'|) = -\beta g_l(|\mathbf{r} - \mathbf{r}'|) \nabla V(|\mathbf{r} - \mathbf{r}'|) \quad (1.3.12)$$

$$\nabla H_l(|\mathbf{r} - \mathbf{r}'|) = -\beta \rho_l \int d\mathbf{r}'' \left. \frac{\delta g(\mathbf{r}, \mathbf{r}')}{\delta \rho(\mathbf{r}'')} \right|_l \nabla V(|\mathbf{r} - \mathbf{r}'|) . \quad (1.3.13)$$

Equation (1.3.11) is to be compared with the basic equation of the modern theory of freezing, that is

$$\rho(\mathbf{r}) = \rho_l \exp\left[\int d\mathbf{r}' c_l(|\mathbf{r} - \mathbf{r}'|) \Delta \rho(\mathbf{r}')\right] . \quad (1.3.14)$$

It is also clear that if one neglects the second term on the right-hand side of eqn.(1.3.11) one can recover the average density that was introduced by Kirkwood and Monroe (eqn.1.3.3.). Hence, neglecting the density dependence of the pair correlation function, i.e. the term $H_l(|\mathbf{r} - \mathbf{r}'|)$, may explain the qualitatively poor results obtained from the Kirkwood-Monroe approximation ³³.

Various forms of integro-differential or non-linear integral equations have been considered for distribution functions. Developments in this direction have been carried out by various authors: by Tyablikov ³⁴ on the basis of the Bogoliubov hierarchy, Vlasov ³⁵ using the Vlasov equation, Raveché - Stuart ³⁶ and Raveché-Kayser ³⁷ using the YBG hierarchy, Weeks et al ³⁸ and Jancovici ³⁹ with a modified version of the Kirkwood-Monroe theory. None of these attempts has been applied to real systems, and in fact when they were applied to hard spheres, the results are often contradictory. There are three reasons behind these failures:(i) the linearization of the equations is obtained by treating the liquid-solid transition as a "soft bifurcation" problem while the first-order character of the transition requires the use of a "hard bifurcation" treatment; (ii) the closure of hierarchical equations leads one to put great emphasis on the first peak of the pair correlation function while the phase transition is linked to the oscillation which follow the first peak; (iii) in hierarchical equations the interparticle potential appears explicitly, while the experimental data show a non-critical dependence on the potential details in the transition phenomenon.

These difficulties are solved within the framework of the density functional theories. This approach to the transition began with Lovett ⁴⁰ and Lovett and Buff ⁴¹, who tried to determine the bifurcation point by investigating the stability of the liquid compared to the crystalline state through a relation that connects the one-particle distribution function with the direct correlation function. Their approach still requires a pair potential and the solutions found are characteristic of a second-order transition. The discontinuous character in the density change at the liquid- solid transitions was reexamined by Ryzhov and Tareeva ⁴² and Bagchi et al ⁴³: their results

are not qualitative and connections between the numerical instability of the liquid, the bifurcation points and the transition point are not yet clear. In the following section (1.4) we will give in brief the essential equations of density functional theory, whereas in chapter 2 a full derivation of the set of equilibrium equations for the freezing phenomenon will be given.

1.4 Density Functional Approach to Liquid Solid Coexistence

A description of the crystalline solid as a microscopically inhomogeneous system is provided by the cluster expansion ⁴⁴⁻⁴⁶. In particular, this considers the solid as a perturbation (in principle, to infinite order) about the uniform liquid, and is closely related to the density functional formalism ^{47,48}. The formalism is based on a theorem by Mermin, proving that the Helmholtz free energy F is a functional of the density profile $\rho(\mathbf{r})$, reaching its minimum value for the equilibrium profile. The general aim in the implementation of the theory is an approximate evaluation of the free energy functional $F[\rho(\mathbf{r})]$ for a given inhomogeneous system from knowledge of the thermodynamic and correlation-response properties of a corresponding homogeneous system.

The use of the density functional methods in the theory of freezing was opened by the work of Ramakrishnan and Yussouff ⁴⁹, in which the two bulk phases were treated in the grand canonical ensemble and hence it was easy to keep the temperature and the chemical potential constant in the two phases at coexistence. At the same time the interparticle potential (pair-wise or more complex) was not explicitly involved. The theory involves only the direct correlation function $\tilde{c}_l(k)$ [$\tilde{c}_l(k) = 1 - 1/S(k)$] of the liquid at freezing. Haymet and Oxtoby ⁵⁰ have reformulated the Ramakrishnan and Yussouff theory in the scheme of the density functional theory of non-uniform system ⁴⁷. March and Tosi ⁵¹ have developed a scheme for the application of the theory to more complex systems like alkali-halides and alkaline-earth halides. We will briefly report some applications of the density functional theory for different systems in the following sections.

In a theory of freezing one starts from the fluid phase side, described by a uniform density ρ_l . Then the existence of crystalline solutions will be searched by looking for the presence of a density profile $\rho_s(\mathbf{r})$ which is a periodic function of position, represented by the Fourier series

$$\rho_s(\mathbf{r}) = \rho_s + \sum_{\mathbf{G} \neq 0} \rho_{\mathbf{G}} \exp[i\mathbf{G} \cdot \mathbf{r}] \quad , \quad (1.4.1)$$

where \mathbf{G} are the reciprocal lattice vectors (RLV) of a crystal structure. At coexistence with the liquid at density ρ_l , the order parameters of the phase transition, which are the mean density change $(\rho_s - \rho_l)/\rho_l \equiv \eta$ and the Fourier

components $\rho_{\mathbf{G}}$, take spontaneously finite values. The quantities $|\rho_{\mathbf{G}}|^2$ measure the Debye-Waller factor at the Bragg reflections and are therefore related, at least in the harmonic approximation for lattice vibrations, to the mean-square atomic displacement entering Lindemann's criterion for melting.

The Helmholtz free energy functional for a classical system in an external potential $U(\mathbf{r})$ reads:

$$F[\rho(\mathbf{r})] = k_B T \int d\mathbf{r} \rho(\mathbf{r}) [\ln(\lambda^3 \rho(\mathbf{r})) - 1] + \int d\mathbf{r} \rho(\mathbf{r}) U(\mathbf{r}) + F_e[\rho(\mathbf{r})] , \quad (1.4.2)$$

where λ is the thermal de Broglie wavelength and F_e is the excess free energy functional. Introducing suitable Lagrange multipliers allows one to take into account some constraints in the minimization of the free energy leading to the equilibrium conditions, in particular, one needs to consider variations of the density profile while keeping constant the number of particle in the system. Thus, one introduces the chemical potential μ and minimize the grand potential $\Omega = F - N\mu$, obtaining formal equations for the equilibrium density profile,

$$\frac{\delta \Omega}{\delta \rho(\mathbf{r})} = \frac{\delta F}{\delta \rho(\mathbf{r})} - \mu + U(\mathbf{r}) = 0 \quad . \quad (1.4.3)$$

Satisfying eqn.(1.4.3) leads to a mechanical stable density profile, whereas thermodynamic stability requires the stronger condition that $\Omega[\rho(\mathbf{r})]$ be at its absolute minimum.

The equilibrium condition can also be obtained in a differential form by taking advantage of the one-to-one correspondence between the density $\rho(\mathbf{r})$ and the external potential $U(\mathbf{r})$. By considering an infinitesimal rigid translation of the whole system, one finds ⁵²

$$\nabla(\mu - U(\mathbf{r})) = - \int d\mathbf{r}' \chi^{-1}(\mathbf{r}, \mathbf{r}') \nabla \rho(\mathbf{r}') \quad (1.4.4)$$

which reduces in the classical limit to ⁵³

$$\nabla(\mu - U(\mathbf{r})) = \nabla \rho(\mathbf{r}) / \rho(\mathbf{r}) - \int d\mathbf{r}' c(\mathbf{r}, \mathbf{r}') \nabla \rho(\mathbf{r}') \quad . \quad (1.4.5)$$

This form of the equilibrium condition emphasizes the role of the linear density response function $\chi(\mathbf{r}, \mathbf{r}')$ of the inhomogeneous system at density $\rho(\mathbf{r})$ to a weak external potential, or equivalently of the two-body direct correlation function $c(\mathbf{r}, \mathbf{r}')$ in the classical case, in determining the density profile. In relation to freezing, the external potential $U(\mathbf{r})$ is to be considered as an external potential of the desired lattice periodicity, which is applied to the liquid approaching crystallization and hence modulates its density through generation of density waves. At liquid-solid coexistence the modulating potential can be allowed to vanish, while the amplitude of the

density waves, ρ_G , will have finite values, giving the order parameters of the new phase.

The above discussion presents the main ideas behind the density functional approach. In the following two sections (1.5 , 1.6) we will briefly review tests of the approximations to the free energy functional and some applications to various systems.

1.5 Application of the Density Functional Approach to the Hard Sphere System

Freezing of the hard-sphere fluid has been studied extensively by different authors using different approximations and different approaches to the free energy functional. A common approximation concerns, of course, the expansion (1.4.1) for the density profile, $\rho(\mathbf{r})$. The sum that appear in it is, in principle, over an infinity of reciprocal lattice vectors but for purposes of calculation it must be truncated after a finite number of terms.

In this section we are going to discuss different approximations to the free energy functional, which have been tested on the hard sphere system.

1.5.1 Cluster Expansion and its Truncation (TCE)

In the cluster expansion ^{44- 46,50,54} the excess free energy functional $F_e[\rho(\mathbf{r})]$ is expanded to infinite order around a homogenous fluid. It was noticed by Yang et al ⁵⁵ that the function

$$c(\mathbf{r}) = \frac{\delta F_e[\rho(\mathbf{r})]}{\delta \rho(\mathbf{r})} \quad (1.5.1)$$

plays the role of an effective one-body potential. Then the coefficients of the expansion are the Ornstein-Zernike ⁵⁶ two-body and higher direct correlation functions of the fluid. A truncation of the expansion at the lowest order yields the equilibrium condition for the density profile in the crystal at coexistence with the liquid, at the same temperature and chemical potentials as

$$\ln[\rho(\mathbf{r})/\rho_l] = \int d\mathbf{r}' c_l(|\mathbf{r} - \mathbf{r}'|)[\rho(\mathbf{r}') - \rho_l] \quad (1.5.2)$$

where $c_l(\mathbf{r})$ is the two-body correlation function of the liquid. By comparison with eqn.(1.4.5), we see that eqn.(1.5.2) can be obtained from it through the replacement of $c(\mathbf{r}, \mathbf{r}')$ by the liquid direct correlation function ⁵¹. At the same time eqn.(1.5.2) is in essence equivalent to the hypernetted-chain theory (HNC) of bulk liquid structure.

At this level of approximation, and in relation to density profile of the crystal in eqn.(1.4.1), one needs to invoke only the Fourier transform of $c_l(\mathbf{r})$

evaluated at the stars of reciprocal lattice vectors and at $\mathbf{k} = 0$. The value of $\bar{c}_l(0)$ is determined by the isothermal compressibility K_T of the liquid. In terms of the liquid structure factor $S(k)$, we have for a classical system

$$\bar{c}_l(k) = 1 - 1/S(k) \quad (1.5.3)$$

and

$$\bar{c}_l(0) = 1 - 1/S(0) = 1 - \frac{1}{\rho_l k_B T K_T} \quad (1.5.4)$$

Inclusion of higher-order terms, say at the level of three-body correlation functions, involves nonlinear physical properties:

1. $\bar{c}_l^{(3)}(0, 0)$, i.e. the density dependence of the compressibility.
2. $\bar{c}_l^{(3)}(\mathbf{G}, 0)$, i.e. the density dependence of the liquid structure factor at the reciprocal lattice vectors.
3. $\bar{c}_l^{(3)}(\mathbf{G}, \mathbf{G}')$, i.e. the coupling between microscopic order parameters, where the angular dependence may start to play a role in determining the stable crystal structure.

Haymet⁵⁴ has been able to predict the liquid and solid densities at which the hard sphere system freezes into a face centre lattice. In his work he used Thiele-Wertheim^{57,58} exact solution of the Percus-Yevick equation for the liquid structure, which is a well defined approximate closure of the Ornstein-Zernike equation, to reproduce the liquid structure to obtain the coefficients $\bar{c}_l(\mathbf{G})$ and $\bar{c}_l^{(3)}(\mathbf{G}, 0)$. He took the coefficient $\bar{c}_l^{(3)}(\mathbf{G}, \mathbf{G}')$ equal to zero for non vanishing \mathbf{G} and \mathbf{G}' , which means a further approximation. In fact the evaluation of third-order coefficients involves a large and delicate numerical effort. Following this scheme we have in Fourier transform

$$\bar{c}_l(k) = -4\pi\rho\sigma^3(k\sigma)^{-1}[\lambda_1 I_1(k) + 6\zeta\lambda_2 I_2(k) + 1/2\zeta\lambda_4 I_2(k)] \quad (1.5.5)$$

$$\bar{c}_l^{(3)}(k, 0) = -c_l(k) + \rho(\partial/\partial\rho)c_l(k) \quad (1.5.6)$$

where

$$I_n(k) = \int_0^1 dx x^n \sin(k\sigma x)$$

$$\lambda_1 = (1 + 2\zeta)^2(1 - \zeta)^{-4} \quad ; \quad \lambda_4 = (1 + 1/2\zeta)^2(1 - \zeta)^{-4} \quad ,$$

with the packing fraction ζ defined as $\zeta = \pi/6\rho\sigma^3$. In this calculation, fifteen stars of reciprocal lattice vectors have been used to obtain convergence. Table(1.4) and fig. 1.7 show the freezing results for the hard sphere fluid into

the fcc lattice. In fig. 1.8 the structures factor $S(k) = [1 - \bar{c}_l(k)]^{-1}$ is plotted at a density $\rho = 0.95$ (in units of σ^3) near the freezing density, and the positions of the 15 shells of RLV (once the first one has been fixed at the first peak position of $S(k)$) are also indicated. At the end of this section we will give the results available for the freezing of the hard sphere system as obtained by different approximations, in comparison with computer simulations.

$ \mathbf{G} ^2$	$s_{\mathbf{G}}$	\mathbf{G}	$\rho_{\mathbf{G}}$	$x_{\mathbf{G}}$	$A_{\mathbf{G}}$
0			0.060	- 5.096	
3	8	(111)	0.998	0.719	0.895
4	6	(200)	0.891	- 0.027	0.436
8	12	(220)	0.918	- 0.151	- 1.483
11	24	(311)	0.875	0.244	0.898
12	8	(222)	0.863	0.080	0.425
16	6	(400)	0.805	- 0.252	- 1.138
19	24	(331)	0.773	0.005	- 0.188
20	24	(420)	0.760	0.079	0.164
24	24	(422)	0.717	0.079	0.383
27	8	(333)	0.686	- 0.061	- 0.237
27	24	(511)	0.680	- 0.060	- 0.237
32	12	(440)	0.636	- 0.068	- 0.407
35	48	(531)	0.608	0.017	0.017
36	24	(442)	0.601	0.039	0.146
36	6	(600)	0.593	0.039	0.146

Table 1.4: Freezing parameter for hard spheres at the density 0.976 from the PY structure factor. $x_{\mathbf{G}}$ is defined as $x_o = c(0)\eta + 1/2 \sum_{\mathbf{G} \neq 0} \bar{c}^{(3)}(\mathbf{G}, 0)\rho_{\mathbf{G}}$, $x_o = [\bar{c}(\mathbf{G}) + \bar{c}^{(3)}(\mathbf{G}, 0)\eta]\rho_{\mathbf{G}}$. $A_{\mathbf{G}}$ is defined as $\bar{c}(\mathbf{G}) + (2\eta + 1)\bar{c}^{(3)}(\mathbf{G}, 0)$, $s_{\mathbf{G}}$ is the number of RLV in each star. From ref. [54]

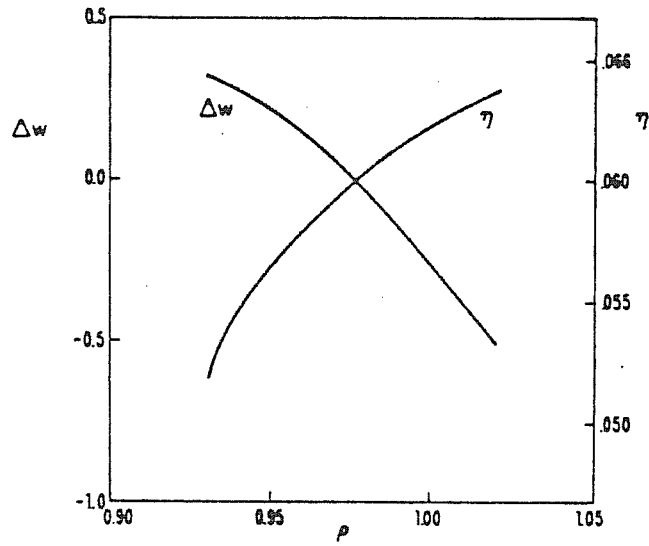


Figure 1.7: *The thermodynamic potential ΔW and the fractional density change on freezing η for the hard sphere system. From ref. [54]*

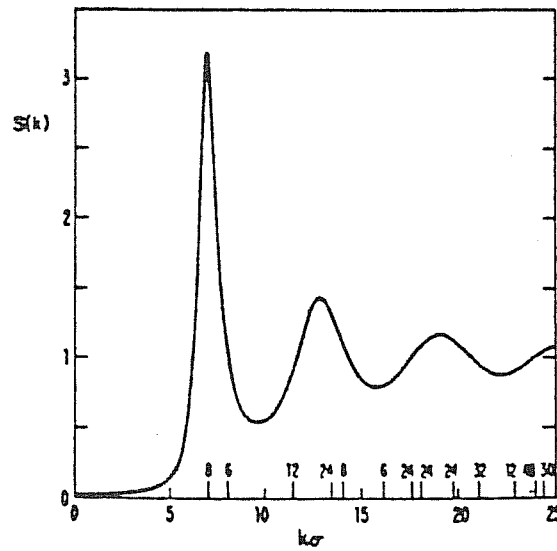


Figure 1.8: *The structure factor, $S(k)$, for hard spheres at density close to the freezing one, $\rho = 0.95$, and the relative magnitudes of the RLV of the fcc crystal. From ref. [54]*

1.5.2 Effective Liquid Approximation (ELA)

Another line of approach was developed by Baus and Colot^{60,61} and by Iglói and Hafner⁶², in which they used a reference liquid to describe the transition to the crystalline phase. Since the excess free energy $F_e[\rho_s(\mathbf{r})]$ is related to the two-body direct correlation function by;

$$c(\mathbf{r}, \mathbf{r}'; [\rho_s]) = -\frac{\delta^2 \beta F_e[\rho_s(\mathbf{r})]}{\delta \rho_s(\mathbf{r}) \delta \rho_s(\mathbf{r}')} \quad (1.5.7)$$

they expand the excess free energy around the reference liquid, rather around the real one:

$$\begin{aligned} F_e[\rho_s(\mathbf{r})] &= F_e[\rho_R] + \int d\mathbf{r} \Delta\rho(\mathbf{r}) \frac{\delta F_e[\rho_R]}{\delta \rho_R(\mathbf{r})} - \\ &- k_B T \int d\mathbf{r} \int d\mathbf{r}' \int_0^1 d\lambda \int_0^\lambda d\lambda' \\ &c(\mathbf{r}, \mathbf{r}'; [\rho_R + \lambda' \Delta\rho(\mathbf{r}')]) \Delta\rho(\mathbf{r}) \Delta\rho(\mathbf{r}'). \end{aligned} \quad (1.5.8)$$

The solid phase is thus reached by starting from a reference state ($\lambda = 0$) of density $\rho_R(\mathbf{r})$ and “charging” its density gradually along the path $\rho_R(\mathbf{r}) + \lambda \Delta\rho(\mathbf{r})$ up to the solid density $\rho_s(\mathbf{r})$ ($\lambda = 1$). Here, $\Delta\rho(\mathbf{r}) = \rho_s(\mathbf{r}) - \rho_R(\mathbf{r})$, and the double integral over λ and λ' can be simplified by using the identity

$$\int_0^1 d\lambda \int_0^{\lambda'} d\lambda' h(\lambda') = \int_0^1 d\lambda (1 - \lambda) h(\lambda) \quad ,$$

which is valid for any function $h(\lambda)$. The first term in eqn.(1.5.8) is known since it corresponds to the chosen reference liquid, while the second term can be dropped by taking $\rho_R \equiv \rho_R(\mathbf{r})$ to be equal to the average density of the solid; i.e. $\int d\mathbf{r} \Delta\rho(\mathbf{r}) = 0$. One is then left with evaluating the direct correlation function of the solid density $\rho_R + \lambda \Delta\rho(\mathbf{r})$ with $0 \leq \lambda \leq 1$ and $\Delta\rho(\mathbf{r}) = \rho_s(\mathbf{r}) - \rho_R$. This direct correlation function was approximated by that of an effective liquid of density $\bar{\rho}$, say $c_l(|\mathbf{r} - \mathbf{r}'|; \bar{\rho})$, hence the name effective-liquid approximation (ELA) is given to this approach. If the effective-liquid density $\bar{\rho}$ corresponding to the solid of density $\rho_s(\mathbf{r})$ depends only on the average density of the solid ρ_s ,

$$\rho_s = \frac{1}{V} \int d\mathbf{r} \rho_s(\mathbf{r}) \quad ,$$

then the effective liquids corresponding to $\rho_s(\mathbf{r})$ and $\rho_R + \lambda \Delta\rho(\mathbf{r})$ are the same because here $\rho_R = \rho_s$. The excess free energy equation (i.e. eqn.1.5.8) reduces to

$$\beta F_e^{ELA}[\rho_s] = \beta F_e(\rho_R) - \frac{1}{2} \int d\mathbf{r} \int d\mathbf{r}' c(|\mathbf{r} - \mathbf{r}'|; \bar{\rho}(\rho_R)) \Delta\rho(\mathbf{r}) \Delta\rho(\mathbf{r}'). \quad (1.5.9)$$

where $\bar{\rho} = \bar{\rho}(\rho)$ is the density of the effective liquid corresponding to a solid of average density ρ . Finally in order to fix $\bar{\rho}(\rho)$, they choose the effective liquid in such a way that its direct correlation function will mimic that of the solid. The choice of $\bar{\rho}(\rho)$ used by Baus and Colot⁶⁰ was obtained by imposing the condition that the position of the main peak of the static structure factor of the effective liquid of density $\bar{\rho}$ coincide with the smallest reciprocal lattice vectors of the solid of average density ρ . The results obtained from the ELA for the hard sphere system are quite good as shown in table (1.5).

	<i>Theory</i>	<i>Monte Carlo simulation</i>
ρ_s	1.035	1.036-1.041
ρ_l	0.976	0.939-0.948
η	0.060	0.090-0.110

Table 1.5: Numerical and computer predictions for freezing of hard spheres into fcc lattice. The values are in units of σ^3 , where σ is the hard sphere diameter and η the density change on freezing. From ref.[60]

Recently a modified ELA (MELA), proposed by Baus⁶³, has taken into account the possibility of extending the definition of the effective liquid to other non-uniform system besides the solid, which was not obvious in the ELA. This modified scheme is based on using the exact equation for the excess free energy, (eqn.1.5.8), with $\rho_R \equiv 0$, i.e.

$$\beta F_e[\rho_s] = - \int d\mathbf{r} \int d\mathbf{r}' \int_0^1 d\lambda \int_0^\lambda d\lambda' c(\mathbf{r}, \mathbf{r}'; [\lambda' \rho_s]) \rho_s(\mathbf{r}) \rho_s(\mathbf{r}') \quad (1.5.10)$$

and introducing the ELA into this equation:

$$\beta F_e^{MELA}[\rho_s] = - \int d\mathbf{r} \int d\mathbf{r}' \int_0^1 d\lambda \int_0^\lambda d\lambda' c_l(|\mathbf{r} - \mathbf{r}'|; \lambda' \bar{\rho}) \rho_s(\mathbf{r}) \rho_s(\mathbf{r}'). \quad (1.5.11)$$

Then one can obtain the MELA by requiring that the effective liquid density $\bar{\rho}$ of eqn(1.5.11) be determined self-consistently from equating the excess free energy per particles of the solid to that of the effective liquid itself ($\psi_l(\bar{\rho})$):

$$\begin{aligned} \frac{1}{\rho_s V} F_e^{MELA}[\rho_s] &= \psi_l(\bar{\rho}) \\ &\equiv -k_B T \bar{\rho} \int d\mathbf{r} \int_0^1 d\lambda \int_0^\lambda d\lambda' c_l(|\mathbf{r}|; \lambda' \bar{\rho}). \end{aligned} \quad (1.5.12)$$

This determines $\bar{\rho}$ in terms of $\rho_s(\mathbf{r})$ at any given $c_l(|\mathbf{r}|; \rho)$. This modified version seems simple to implement and has been shown to yield better results than those obtained by ELA⁶⁴.

1.5.3 Weighted Density Approximation (WDA)

A new line of approach initiated by Tarazona⁶⁵ and later extended by Curtin and Ashcroft⁶⁶, proposes an alternative approximation to the free energy functional of the crystal. It is based on a refinement of the well-known local-density approximation for the quantal electron gas⁴⁸, whereby the free energy density for a non-uniform system (say, the solid) is approximated by evaluating it on the uniform phase (say, the liquid) at a density equal to the local density of the non-uniform phase. In this refined approach the free energy density of the non-uniform (inhomogeneous) phase is represented as that of a uniform (homogeneous) phase, taken at an auxiliary density which depends parametrically on the chosen point. The appropriate density is obtained by weighting the physical density over a physical relevant range about the given point. Thus the resultant weighted-density approximation (WDA) takes into account the short-ranged, nonlocal effects present in the real system. The WDA has an analogue in the quantal electron-gas problem, where effective densities are frequently used to construct an approximate exchange-correlation energy functional that has been analyzed in that context⁶⁷.

The Helmholtz free energy $F[\rho_s]$ is thus given by

$$F[\rho_s] = \int d\mathbf{r} \rho_s(\mathbf{r}) \{ \ln[\lambda^3 \rho_s(\mathbf{r})] - 1 \} + \int d\mathbf{r} \rho_s(\mathbf{r}) U(\mathbf{r}) + F_e[\rho_s] \quad (1.5.13)$$

the excess free energy functional $F_e[\rho_s]$ is approximated as

$$F_e^{WDA} = \int d\mathbf{r} \rho_s(\mathbf{r}) \psi_l(\bar{\rho}(\mathbf{r})) \quad (1.5.14)$$

Here, $\psi_l(\rho)$ is the excess free energy per particle of the uniform phase of density ρ , while $\bar{\rho}(\mathbf{r})$ is the weighted solid density,

$$\bar{\rho}(\mathbf{r}) = \int d\mathbf{r}' \rho_s(\mathbf{r}') \omega(\mathbf{r} - \mathbf{r}'; \bar{\rho}(\mathbf{r})) \quad , \quad (1.5.15)$$

with $\omega(\mathbf{r}; \rho)$ the weighting function. The difficulty now appears in the appropriate choice of the weighting function $\omega(\mathbf{r}; \rho)$, and the technical

problem of solving eqn.(1.5.15), which is an implicit equation for $\bar{\rho}(\mathbf{r})$. At this stage a connection is made with the exact density functional relation between the direct correlation function of the solid and its excess free energy, eqn.(1.5.7), in the limit of a uniform phase, $\rho_s(\mathbf{r}) \rightarrow \rho$. In addition, one has to impose that $\omega(\mathbf{r}; \rho)$ be normalized for any ρ ,

$$\int d\mathbf{r} \omega(\mathbf{r}; \rho) = 1 \quad .$$

Curtin and Ashcroft considered the non-linear differential equation for $\omega(\mathbf{r}; \rho)$ that follows from

$$-\left(\frac{\delta^2 \beta F_e^{WDA}[\rho_s(\mathbf{r})]}{\delta \rho_s(\mathbf{r}) \delta \rho_s(\mathbf{r}')} \right)_{\rho_s \rightarrow \rho} = \hat{c}(|\mathbf{r} - \mathbf{r}'|; \rho) \quad . \quad (1.5.16)$$

In Fourier transform, this leads to

$$-\beta^{-1} \hat{c}(k; \rho) = 2\psi'_i(\rho) \omega(k; \rho) + \rho \frac{\partial}{\partial \rho} (\psi'_i(\rho) [\omega(k; \rho)]^2) \quad , \quad (1.5.17)$$

where $\psi'_i(\rho) = \partial \psi_i(\rho) / \partial \rho$. This approach yields good results, but is elaborate. A modified WDA (or MWDA) has recently proposed by Denton and Ashcroft⁶⁸, in which almost all the technical difficulties of the WDA can be avoided by replacing eqn.(1.5.14) by

$$\left[\frac{1}{\rho_s V} \right] F_e^{MWDA}[\rho_s] = \psi_i(\bar{\rho}) \quad , \quad (1.5.18)$$

where $\bar{\rho}$ is a uniform weighted density in terms of a new weighting function $\bar{\omega}(\mathbf{r}; \rho)$

$$\bar{\rho} = \frac{\int d\mathbf{r} \int d\mathbf{r}' \rho(\mathbf{r}) \rho(\mathbf{r}') \bar{\omega}(\mathbf{r} - \mathbf{r}'; \bar{\rho})}{\int d\mathbf{r}'' \rho(\mathbf{r}'')} \quad . \quad (1.5.19)$$

Then eqn.(1.5.17) will lead to simpler equation, that is

$$-\beta^{-1} \hat{c}(k; \rho) = 2\psi'_i(\rho) \bar{\omega}(k; \rho) + \rho \psi''_i(\rho) \delta_{k,0} \quad , \quad (1.5.20)$$

with $\psi''_i(\rho) = \partial^2 \psi_i(\rho) / \partial \rho^2$. The results obtained from this MWDA compare well with those obtained from WDA. At this level Baus⁶⁹ has found an unexpected relation between the MELA (section 1.5.2) and MEDA, that the effective-liquid density $\bar{\rho}$ appearing in eqn.(1.5.11) and eqn.(1.5.12) in the MELA, can be written in the form of eqn.(1.5.19) with

$$\bar{\omega}(\mathbf{r}; \rho) = \frac{\int_0^1 d\lambda \int_0^\lambda d\lambda' \hat{c}(|\mathbf{r}|; \lambda' \rho)}{\int d\mathbf{r}' \int_0^1 d\lambda \int_0^\lambda d\lambda' \hat{c}(|\mathbf{r}'|; \lambda' \rho)} \quad . \quad (1.5.21)$$

This is an explicit expression for the weighting function in terms of the direct correlation function $c(|\mathbf{r}|; \rho)$. The MELA will thus have the same structure as the WDA or the MWDA, but with weighting functions that are no longer given by eqn.(1.5.17) or eqn.(1.5.20). The weighting functions are different because in the (M)WDA the “weighted” density is introduced through the thermodynamic of the solid and required to reproduce the structure of the liquid, whereas in the (M)ELA the “effective” density is introduced through the structure of the solid and required to produce the thermodynamics of the liquid.

In conclusion, we present in table (1.6) the results for the freezing of the hard sphere fluid into an fcc crystal, as obtained by the different available approximation approaches.

	ζ_l	ζ_s	ρ_l	ρ_s	$\Delta S/k_B$	$S(k_{peak})$	L
<i>MC</i> ²⁶	0.494	0.545	0.939	1.036	1.16	2.85	0.126
			$\div 0.948$	$\div 1.045$			
<i>TCE – VW</i> ⁷²	0.495	0.543	0.946	1.037	1.05	2.92	0.070
<i>TCE – PY</i> ⁷²	0.506	0.541	0.966	1.033	0.94	3.35*	
<i>ELA – PY</i> ^{60,61}	0.520	0.567	0.993	1.083	1.03	3.65	0.074
					,1.36		
<i>ELA – PY</i> ⁶²	0.510	0.563	0.975	1.076	1.10	3.44	0.070
					,1.42		
<i>MELA</i> ⁶⁴	0.484	0.538	0.924	1.027	1.21		0.098
<i>WDA – PY</i> ⁶⁶	0.497	0.547	0.905	1.025	1.41	2.82	0.093
<i>MWDA</i> ⁶⁸	0.476	0.542	0.909	1.035	1.35		0.097

Table 1.6: Coexistence data for the freezing of hard sphere into an fcc crystal as obtained from the different approximate approaches in the literature, compared with Monte Carlo (MC) results. ζ_l and ζ_s are the packing fractions of the liquid and solid at coexistence. The densities ρ_l and ρ_s are in units of (diameter)³. ΔS is the change in the entropy. $S(k_{peak})$ the value of the structure factor at its first peak (values marked with an asterisk have been calculated from the value of ρ_l reported). L is the Lindemann ratio. All theories used the Percus–Yevick theory (PY) for liquid phase, but from TCE calculations of Haymet and Oxtoby[72] we notice a dependence of the results on the description of the bulk liquid structure, the Verlet–Weis parametrization (VW) being more accurate than the PY theory.

1.5.4 Parametrization of the Density Profile

The Fourier series for the right-hand side of eqn(1.5.2), which describes the density profile of the solid, converges rather slowly, thus requiring explicit calculation of rather large number of order parameters $\rho_{\mathbf{G}}$. Haymet ⁵⁴ has retained all these terms of the Fourier expansion up to fifteen stars of reciprocal lattice vectors. Later, Iglói and Hafner ⁶² showed that the slow convergence of the Fourier series (up to forty stars were retained) leads to an oscillatory behaviour of the results. These oscillations will disappear when sixty stars are retained (Barrat et al ⁷⁰).

Haymet ⁵⁴ was the first to show that in the hard sphere system, excepting the first few order parameters, a harmonic formula is approximately correct. The implication is that, although the theory involves an infinite set of order parameters, the first few ones dominate and 'enslave' the rest. Later workers have often assumed this relationship between the first order parameter and all the others, by representing the density profile $\rho_s(\mathbf{r})$ in real space as a superposition of Gaussians centered at the various sites and with a width that is to be evaluated variationally. That is,

$$\rho_s(\mathbf{r}) = (\alpha/\pi)^{3/2} \sum_{\mathbf{R}} \exp[-\alpha(\mathbf{r} - \mathbf{R})^2] \quad , \quad (1.5.22)$$

where $\{\mathbf{R}\}$ are the Bravais lattice vectors and α is the inverse width of the Gaussian, which will be the only parameter describing the solid. The order parameters of eqn.(1.4.1), $\rho_{\mathbf{G}}$, can easily be related to the inverse of the Gaussian width by

$$\rho_{\mathbf{G}} = \exp(-|\mathbf{G}|^2/4\alpha) \quad . \quad (1.5.23)$$

Representing the density profile as a superpositions of Gaussian guarantees a priori the positive character of $\rho(\mathbf{r})$, a property which might be lost by using eqn(1.4.1) truncated at a finite number of reciprocal lattice vectors ⁷¹. Fig. 1.9 shows the average solid phase density for the hard sphere system at freezing using both eqns.(1.5.22) and (1.4.1).

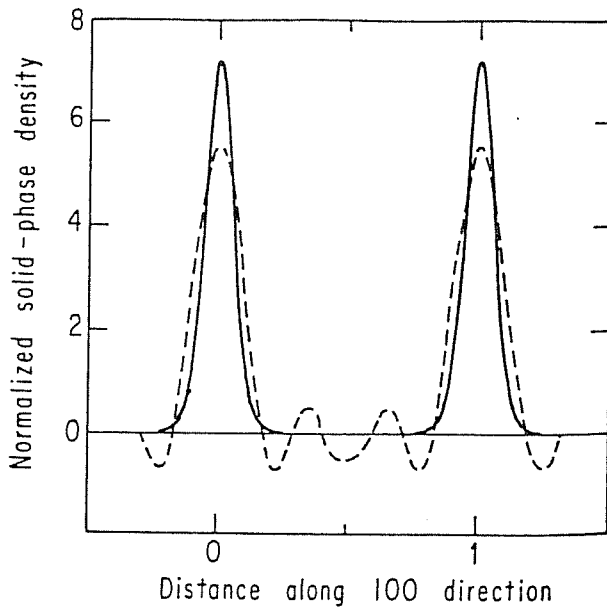


Figure 1.9: *The solid phase density in the (100) direction for the hard sphere system at freezing, averaged over perpendicular planes. The solid line is the result of eqn.(1.5.22) and the dashed line of eqn.(1.4.1), both truncated at the same order of reciprocal lattice vectors. From ref [71]*

1.6 Some Other Applications of the Density Functional Approach

The density functional theory (DFT) of freezing has been successfully applied to the hard sphere system by different authors in a test of different approximate approaches, as we have seen in section (1.5). In the last five years, the use of the density functional approach has been extended to more “realistic” potential models, such as the Lennard-Jones system. In this section we are going to discuss the application of the DFT to the freezing of soft spheres, the Lennard-Jones, alkali halides, binary alloys and ionic melts, and finally we will discuss the extension of the DFT to shear-deformed and dislocated crystals.

1.6.1 Freezing of Soft Spheres and of the One Component Classical Plasma

The simplest family of potentials describing purely repulsive “soft” cores are the inverse power (or soft sphere) potentials. These r^{-n} potentials have been studied extensively by Monte Carlo simulation for several values of the steepness n , as we have seen in section (1.2). The equation of state and the freezing results are available for $n = 12$ ^{21,74}, 9, 6, and 4^{10,12}.

Barrat et al⁷⁰ have investigated freezing in the cases $n = 12, 6$ and 4, using the density functional theory on the basis of two different implementations: (i) treating the two phases in the grand canonical ensemble following Haymet and Oxtoby⁵⁰ and truncating the expansion of the difference in the grand potential after the second-order terms; (ii) following the approach formulated by Baus and Colot^{60,61} and relating the thermodynamic properties of the solid, characterized by the one-particle density $\rho_s(\mathbf{r})$, to those of the homogenous fluid of equal mean density ($\rho_f = \rho_s$), i.e. using the ELA

approximation. Both implementations require as input the direct correlation function of the soft sphere fluid, which were obtained from two schemes. The first scheme was based on an interpolation between the hypernetted chain equations (HNC) and the Percus-Yevick (PY) closure, whereas the second approach was the modified HNC scheme.

In their calculation, the density profile of the solid in real space is described as a superposition of Gaussians centered at lattice sites. They have included sixty stars in the RLV summation. Their results are reported in table (1.7) for various values of the steepness and compared with Monte Carlo data. It is clear that both approaches overestimate the densities of the coexisting fluid and solid phases, and the disagreement with computer simulation data worsen as the steepness n decreases. They found that including higher terms in their first approach, i.e. the three-body correlation function, is important in the case of the soft sphere system. Finally the two approaches predict that the fcc phase is more stable than the bcc phase for all n , which contradicts the behaviour expected for soft repulsions, and the values of the Lindemann ratio in the different cases were smaller than their Monte Carlo counterparts. The Lindemann ratio is found to be practically independent of n .

Crystallization of the classical one-component plasma (OCP) on a uniform background (where the steepness of the potential is $n = 1$) was first noted in Monte Carlo simulation by Brush et al ⁷⁵. Later and more accurate computer simulation work ^{22-25,27} has determined the free energies of the liquid and the body-centered cubic solid phases and has led to a refined assesment of the value Γ_c of the coupling strength $\Gamma = \beta e^2/a$, where $\beta = (k_B T)^{-1}$ and $a = (4\pi\rho/3)^{-1/3}$ in terms of the particle density ρ , at which crystallization into the bcc structure occurs, the best recent estimate being $\Gamma_c = 178$. On the basis of Lindemann's criterion for melting van Horn ⁷⁷ had estimated theoretically, assuming analogy with melting of alkali metals, that $\Gamma_c \simeq 170$.

A microscopic calculation on the crystallization of the OCP, which involves a functional expansion of the free energy of the ordered phase around homogenous liquid similarly to the density-wave theory of freezing, was presented by Bagchi et al ⁷⁸. They used a restricted set of order parameters and went through a bifurcation analysis. Instead Haymet ⁷⁹ was the first to apply the standard DFT approach to this problem, using an extended set of order parameters. Unfortunately his description of the liquid structure was not sufficiently accurate ⁸⁰.

Within the truncated cluster expansion, Rovere and Tosi ⁸⁰ gave a careful treatment of the freezing of the OCP into the bcc lattice. They considered the phase transition in the OCP as occurring at constant temperature and density, in order to make contact with the simulation evidence ^{22,24,25}. In this case the coexistence point (i.e. the value of Γ_c , fixing the melting curve

	x_f	x_s	$\Delta v/v_f$	$S(k_{peak})$	L
n=12					
Theory 1a	1.280	1.370	0.070	3.85	0.07
Theory 1b	1.300	1.380	0.060	3.85	0.07
Theory 2	1.305	1.380	0.060	3.85	0.07
MC	1.150	1.190	0.035	3.05	0.15
n=6					
Theory 1a	3.430	3.520	0.026	4.44	0.07
Theory 1b	3.450	3.540	0.026	4.44	0.07
Theory 2	3.330	3.390	0.020	4.10	0.07
MC	2.180	2.210	0.013	2.99	0.17
n=4					
Theory 1a	12.30	12.47	0.014	4.44	0.07
Theory 1b	12.33	12.50	0.014	4.44	0.07
Theory 2	11.34	11.43	0.007	4.30	0.07
MC	5.540	5.570	0.005	2.68	0.18

Table 1.7: Freezing properties of the soft sphere system $\phi\epsilon(\sigma/r)^n$, for $n=12$, 6 and 4 . where $x_f = (\rho_F\sigma^3)(\epsilon/k_B T)^{3/n}$, $x_s = (\rho_S\sigma^3)(\epsilon/k_B T)^{3/n}$. The static structure factor at the first peak and the lindemann ratio are also shown. Theory 1a \equiv following Haymet and Oxtoby, and truncation of the expansion at second-order terms. Theory 1b \equiv including the three body correlation function in the expansion. Theory 2 \equiv using the ELA approximation. MC \equiv Monte Carlo simulation. From ref[70]

$T_m \propto \rho_m^{1/3}$) is determined by the equality of the Helmholtz free energies for the two bulk phases. Since one is dealing with a system characterized by long-range Coulomb forces, the chemical potential of a single phase on uniform background is to be referred to the spatial average V_M of the Madelung potential in the thermodynamic limit⁸¹. Indeed, the value of V_M depends on the boundary condition assumed in taking the limit, so that it is crucial in phase equilibrium to distinguish between the full electrochemical potential μ and the quantity $\mu^* = \mu - V_M$ for a single bulk phase. Referring to the freezing transition of the OCP at fixed background density ρ , the coexistence of the two phases at the same temperature requires $F_s = F_l$ and $\mu_s = \mu_l$. Hence the equilibrium between two phases is maintained by an interfacial potential drop equal to $\Delta V_M = V_M^s - V_M^l = -(\mu_s^* - \mu_l^*) \equiv -\Delta\mu^*$. This balances an interfacial pressure drop $P_s - P_l = \rho\Delta\mu^*$, since $\Delta F = 0$ at coexistence.

The microscopic condition for equilibrium and coexistence in the OCP, to second order, are

$$\begin{aligned}\beta(F_s - F_l)/N &= \rho\beta(\mu_s^* - \mu_l^*) + \frac{1}{2V} \int \int d\mathbf{r}d\mathbf{r}'c_l(|\mathbf{r} - \mathbf{r}'|)(\rho(\mathbf{r}) + \rho)(\rho(\mathbf{r}') - \rho) + .. \\ &= 0\end{aligned}\quad (1.6.1)$$

and

$$\rho(\mathbf{r}) = \rho \exp \left[\beta(\mu_s^* - \mu_l^*) + \int' d\mathbf{r}'c_l(|\mathbf{r} - \mathbf{r}'|)(\rho(\mathbf{r}') - \rho) + \dots \right] , \quad (1.6.2)$$

where the suffixes s and l denote properties of the bulk solid and fluid phase at zero Madelung potential and the prime attached to the integral in eqn.(1.6.2) is to indicate that the integral, which contains a contribution from the Madelung potential at point \mathbf{r} , is to be evaluated with $V_M = 0$, as in the Ewald method⁸². The quantity $\beta(\mu_s^* - \mu_l^*)$ can be taken from computer simulation data, or through the spatial average of eqn.(1.6.2), which yields

$$\beta(\mu_s^* - \mu_l^*) = -\ln \left(\int d\mathbf{r} \exp \left[\int' d\mathbf{r}'c_l(|\mathbf{r} - \mathbf{r}'|)(\rho(\mathbf{r}') - \rho) + \dots \right] \right) . \quad (1.6.3)$$

The search for the coexistence point was carried out using nineteen stars, of RLV, but excluding the order parameter $\rho_{\mathbf{G}}$ at the (200) star, i.e. setting $\rho_{\mathbf{G}_{200}} = 0$ and excluding the equilibrium equation for this order parameter, since a self-consistent full solution of the equation was otherwise impossible. The value of the direct correlation function in the liquid phase were calculated using the modified hypernetted chain (MHNC) or alternatively the generalized mean spherical (GMSA) approximation, which are both in excellent agreement with simulation data on the fluid structure. The solid-liquid coexistence point was found at $\Gamma_c \simeq 142$ in the MHNC and at $\Gamma_c \simeq 142$ in the GMSA. These values for the coupling parameter Γ_c are not too far from the value $\Gamma_c \simeq 178$ obtained from computer simulation by Slattery et al²⁵, and should be regarded as a lower limit for the theoretical coupling strength of bcc solid-liquid coexistence, since the order parameter $\rho_{\mathbf{G}_2}$ at the star (200) was suppressed as already noted.

The reason behind the theoretical difficulties associated with the order parameter $\rho_{\mathbf{G}_2}$ at the star (200) can be seen from the values of the direct correlation function in the Fourier space $\bar{c}(\mathbf{G})$ which is strongly negative in this region of wave numbers (fig. 1.10). Alternatively, the liquid structure factor $S(k)$ has a deep minimum near the (200) star. The order parameter $\rho_{\mathbf{G}_2}$ had been excluded also in the earlier application of DFT to freezing into bcc lattice, both for sodium in the work of Ramakrishnan and Yussouff⁴⁹ and for the classical plasma in the work of Bagchi et al⁷⁸. The rationale behind this procedure is that, since the liquid structure factor shows that

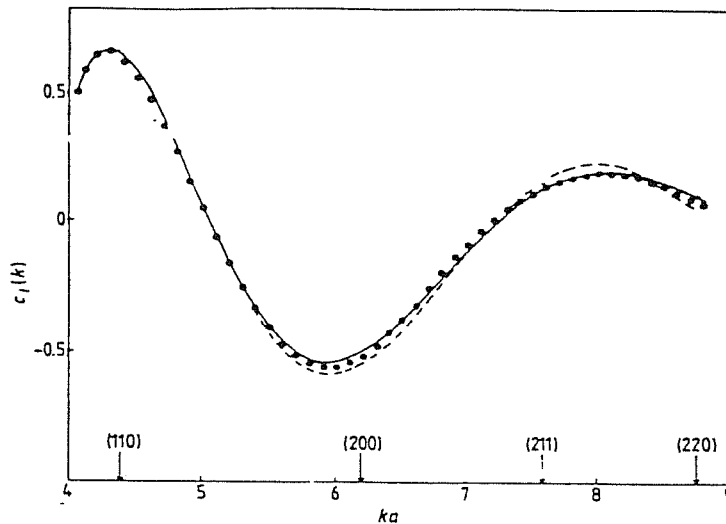


Figure 1.10: The direct correlation function $\bar{c}_l(k)$ of the classical plasma in the fluid phase at $\Gamma = 160$ as a function of ka in the region of the first stars of reciprocal lattice vectors for the body centered cubic lattice at density $n = (4\pi a^3/3)^{-1}$. The full circles are from computer simulation; the full curve gives the GMSA results and the broken curve gives the results for the MHNC approximation. From ref.[80]

the homogenous liquid is rather rigid against a modulation by a density wave with wave vector \mathbf{G}_2 , then the order parameter $\rho_{\mathbf{G}_2}$ can only be small and likely arises from a cooperative process which is lost on decoupling the various order parameters through the TCE. The indication arising from these results is that some coupling between order parameters is playing a role in the phase transition: more precisely, it is suggested that the order parameter $\rho_{\mathbf{G}_2}$ may be driven by the order parameter $\rho_{\mathbf{G}_1}$ associated with the (110) star, i.e. that the three body function $c^{(3)}(\mathbf{G}_2, \mathbf{G}_1)$ may have an important role. When these couplings are neglected, agreement with the known coexistence point requires either an implausibly low value of $\rho_{\mathbf{G}_2}$ or a value of $\bar{c}(\mathbf{G}_2)$ which disagrees from the simulation evidence by roughly 30%.

The inclusion of terms of third order was considered by Barrat^{83,84}. Knowledge of three-body direct correlation function $c^{(3)}$ is needed, and a factorization ansatz for this function was combined with the exact relation between $c^{(3)}$ and the derivative of the two-body direct correlation function with respect to the density. Accuracy is limited, but still the conclusion could be reached that such non-linear couplings tends to stabilize the bcc structure for the OCP.

1.6.2 Freezing of the Lennard-Jones System

Solid-liquid coexistence in the Lennard-Jones system (LJ) was examined using the density functional approach by Marshall et al⁸⁵ and by Curtin and Ashcroft⁸⁶. The calculated phase diagram for the LJ is in good agreement with simulation data, except at the highest temperatures. Curtin and Ashcroft used the weighted density approximation (WDA) extended to systems characterized by potentials for which hard sphere perturbation

theory is an appropriate starting point. In fact, they have expanded the excess free energy per particle $F_e[\rho]$ for the inhomogeneous system about a reference system, that of hard spheres of diameter d , i.e.

$$F_e[\rho] \simeq F_{HS}[\rho; d] + \frac{1}{2N} \int \int d\mathbf{r} d\mathbf{r}' \phi(\mathbf{r}' - \mathbf{r}) \rho_{HS}^{(2)}[\mathbf{r}', \mathbf{r}; \rho, d] \quad (1.6.4)$$

where $\phi(\mathbf{r})$ is the full pair potential, $F_{HS}[\rho; d]$ and $\rho_{HS}^{(2)}[\mathbf{r}', \mathbf{r}; \rho, d]$ are the excess free energy per particle and the pair distribution function of the HS system. They used the WDA for the HS reference energy and obtained an approximation concerning the second term in eqn.(1.6.4), where they first expand $F_e[\rho]$ about that of the liquid to all orders:

$$F_e[\rho] = F^l(\rho_o) - \sum_{n=2}^{\infty} \frac{1}{N\beta n!} \int \dots \int d\mathbf{r}_n \dots d\mathbf{r}_1 c^{(n)}(\mathbf{r}_n \dots \mathbf{r}_1) \Delta\rho(\mathbf{r}_n) \dots \Delta\rho(\mathbf{r}_1). \quad (1.6.5)$$

The $c^{(n)}$ are the n^{th} direct correlation functions of the liquid, which was written as $c^{(n)} = c_{HS}^{(n)} + \Delta c^{(n)}$ as the difference between the actual $c^{(n)}$ of the full system and that of the HS reference system. At this point they used the homogenous limit of eqn.(1.6.4) for the liquid free energy, sum the hard sphere contribution to all orders, and neglecting the higher-order terms $\Delta c^{(n)} (n > 2)$. Following this sequence the excess free energy of inhomogeneous liquid is

$$F_e[\rho] = F_{HS}^{WDA}[\rho; d] + \frac{1}{2\rho_o} \int d\mathbf{r} \phi(\mathbf{r}) \rho_{HS}^{(2)l}(\mathbf{r}) - \frac{1}{2\beta N} \int \int d\mathbf{r} d\mathbf{r}' \Delta c^{(2)}(\mathbf{r}' - \mathbf{r}) \Delta\rho(\mathbf{r}') \Delta\rho(\mathbf{r}) , \quad (1.6.6)$$

where $\rho_{HS}^{(2)l}$ is the pair distribution function of HS liquid of diameter d . They added the ideal gas contribution to the excess energy, i.e.

$$\beta F_{id}[\rho] = \ln(\rho_o \lambda^3) - 1 + \frac{1}{V} \int d\mathbf{r} \frac{\rho(\mathbf{r})}{\rho_o} \ln \left[\frac{\rho(\mathbf{r})}{\rho_o} \right] , \quad (1.6.7)$$

with λ the thermal wavelength, and the last term in this equation vanishes in the liquid and is positive for any spatial distributions in $\rho(\mathbf{r})$, reflecting the loss of entropy arising from the restriction of available phase space upon localizing particles.

Applying the above procedure to the LJ system, and assuming the solid density profile in real space as a superposition of Gaussian centered on the observed fcc lattice, fig. 1.11 shows the structure dependent parts of the total free energy, $F = F_{id} + F_{HS}^{WDA} + \Delta F$, as a function of the Gaussian

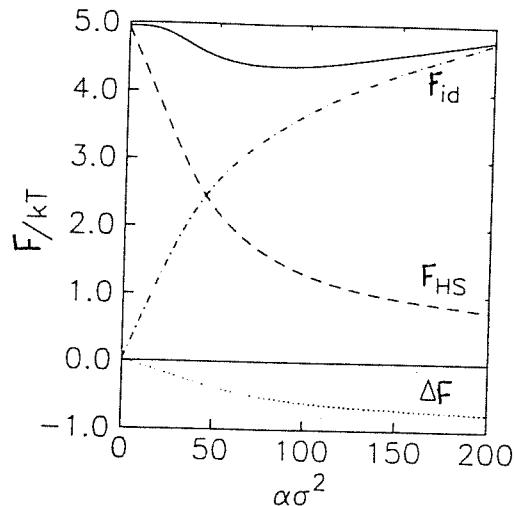


Figure 1.11: *Structure dependent part of the free energy per particle F vs structural parameter $\alpha\sigma^2$ for the fcc LJ solid at $kT = 0.75\epsilon$ and average density $\rho_o\sigma^3 = 1.0$. The different constituents parts of F are shown as discussed in the text. The total free energy exhibit a minimum at $\alpha \neq 0$ indicating the existence of particle localization. From ref.[86]*

widths α . A minimum at $\alpha \neq 0$ occurs, indicating the existence of particle localization, due to the competition between the monotonically increasing F_{id} and monotonically decreasing F_{HS}^{WDA} . The contribution ΔF from the attractive part in the potential has only minor effect of shifting the minimum to slightly higher values of α .

1.6.3 Freezing of Alkali Halides and Binary Alloys

In the preceding sections we have reviewed applications of the density functional approach to freezing of monatomic systems. The extension of the theory to multi-component systems presents no difficulty and we are going to discuss this extension, in brief, to system such as alkali halides and hard sphere mixtures.

The crystalline alkali halides are commonly regarded as the prototype of ionic insulators, and the molten alkali halides as a prototype of dense ionic liquids. As a starting point it is reasonable to assume that the interionic forces for these systems are not changed qualitatively across melting. The short-range order in the dense ionic melt primarily reflects (a) Coulombic attractions and closed-shell overlap repulsions between unlike ions, leading to a sharp region of excluded volume and to a first-neighbour shell of unlike ions around any given ions, and (b) Coulombic repulsions between like ions which are pushed into second-neighbour shells with a less sharply defined region of excluded volume. Ionic alternation in space thus preserved to a considerable extent across melting, and the ionic screening is oscillatory rather than monotonically decaying as in the Debye-Hückel theory. These features of liquid structure are clearly shown in X-ray and neutron diffraction patterns. They imply that the simplest description of liquid structure and freezing is in terms of the Bahatia-Thornton concentration-number (Q-N)

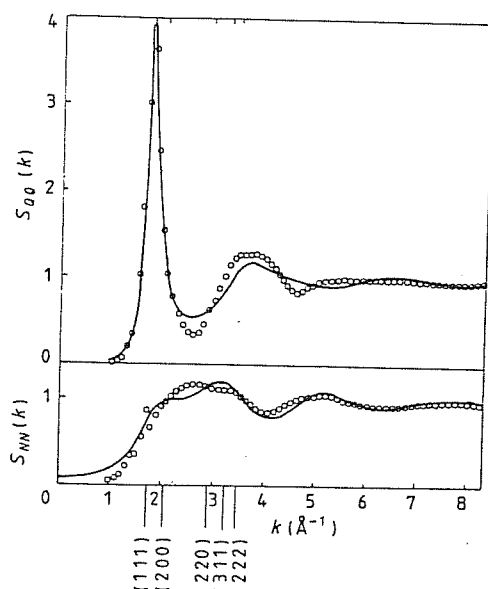


Figure 1.12: The Bahatia-Thornton structure factors $S_{QQ}(k)$ and $S_{NN}(k)$ of molten $NaCl$ near freezing, from neutron diffraction data (circle) and from MHNC theory of a pair potentials model (curves). The location of the first few stars of reciprocal lattice vectors of the $NaCl$ type structure, after adjustment of the (111) star to the peak of $S_{QQ}(k)$, is shown on the horizontal axis. From ref. [83]

structure factors⁸⁸. A detailed discussion of these structure factors will be given in chapter 3, where we are going to use them in discussing freezing for a bond-particle model of covalently bonded systems.

The most prominent feature in the concentration-concentration structure factor $S_{QQ}(k)$, describing the relative short-range order of the two species, is the main peak, which may be put in correspondence with the first odd-index Bragg reflection of the solid, i.e. the (111) reflection that distinguishes the $NaCl$ type structure (fcc lattice with a two-ion basis) from the simple cubic lattice. Figure 1.12 shows the Bahatia-Thornton structure factors $S_{QQ}(k)$ and $S_{NN}(k)$ of molten $NaCl$ near freezing. As already noted, the main peak of the $S_{QQ}(k)$ reflects the short-range relative order of the two species from Coulombic interactions in correspondence to the (111) star of RLV, whereas $S_{NN}(k)$ shows a broad maximum overlying several of the even-index Bragg reflections (Sc lattice). Its shape mainly reflects the low compressibility of the molten salt. The available data suggest $S_{QQ}(k_{peak}) \simeq 4$ as freezing criterion⁸⁹ and freezing arises primarily from a balance between charge ordering, reflected in the main peak of $S_{cc}(k)$, and a relatively large volume change in the order of 15 – 20%, reflected in the low value of $S_{NN}(k \rightarrow 0)$ ⁹⁰.

The basic equations needed to study freezing of alkali halides within the DFT framework have been developed by March and Tosi⁹¹, and it has been shown⁹² that these equations, when reduced to monatomic systems, are closely related to those in the work of Ramakrishnan and Yussouff⁴⁹. The basic set of equations relates the singlet densities $\rho_1(\mathbf{r})$ and $\rho_2(\mathbf{r})$ of a binary system to the partial direct correlation functions $\tilde{c}_{ij}(k)$. The basic input is, within the TCE, the knowledge of $\tilde{c}_{ij}(k)$, or more conveniently their charge-

number (Q-N) counterparts. All these are directly related to the structure factors and hence obtainable either from theory or directly from diffraction experiments.

The singlet densities $\rho_i(\mathbf{r})$ of a system with ν components⁹³ satisfy the equilibrium conditions

$$\frac{\nabla \rho_i(\mathbf{r}_1)}{\rho_i(\mathbf{r}_1)} = \sum_{j=1}^{\nu} \int d\tau c_{ij}(\mathbf{r}_1, \mathbf{r}) \nabla \rho_j(\mathbf{r}) \quad , \quad (1.6.8)$$

leading in the TCE to

$$\ln \frac{\rho_{is}(\mathbf{r}_1)}{\rho_{il}} = \sum_{j=1}^{\nu} \int d\tau c_{ij}(|\mathbf{r}_1 - \mathbf{r}|) [\rho_{js}(\mathbf{r}) - \rho_{jl}] \quad . \quad (1.6.9)$$

The two ionic components in the case of an alkali halide ($\nu = 2$) play essentially equal roles and the most important structural parameters are $\bar{c}_{NN}(k = 0)$ (namely the compressibility) and $\bar{c}_{QQ}(G_1)$ at the first set of reciprocal lattice vectors $\{\mathbf{G}\}$. The corresponding equation for the difference in thermodynamic potential ($\Omega_s - \Omega_l = \Delta\Omega$) that must vanish at coexistence between liquid and solid (for a system with ν components) is

$$\frac{\Delta\Omega}{k_B T} = - \sum_i^{\nu} \int d\mathbf{r}_1 [\rho_{is}(\mathbf{r}_1) - \rho_{il}] + \frac{1}{2} \sum_{i,j}^{\nu} \iint d\mathbf{r}_1 d\mathbf{r}_2 [\rho_{is}(\mathbf{r}_1) + \rho_{il}] c_{ij}(\mathbf{r}_1, \mathbf{r}_2) [\rho_{js}(\mathbf{r}_2) - \rho_{jl}] \quad . \quad (1.6.10)$$

The Fourier expansions for the solid phase densities read

$$\rho_{1s}(\mathbf{r}) = \frac{1}{2} \rho_l \left(1 + \eta + \sum_{\mathbf{G} \neq 0} \rho_{\mathbf{G}} \exp[i\mathbf{G} \cdot \mathbf{r}] \right) \quad (1.6.11)$$

and

$$\rho_{2s}(\mathbf{r}) = \frac{1}{2} \rho_l \left(1 + \eta + \sum_{\mathbf{G} \neq 0} \rho_{\mathbf{G}} \exp[i\mathbf{G} \cdot (\mathbf{r} + \mathbf{h})] \right) \quad , \quad (1.6.12)$$

where ρ_l is the density of the liquid, \mathbf{h} is the vector joining the two ions in the unit cell of the crystal, and η is the volume change upon freezing.

In applying this set of equations to the prediction of freezing for $NaCl$ and $RbCl$ ⁹⁰, the inclusion of first two sets of lattice vectors $\{\mathbf{G}_1\}$ and $\{\mathbf{G}_2\}$ was sufficient. The set $\{\mathbf{G}_1\}$ are reciprocal lattice vectors of type (111) and correspond to the main peak in the charge-charge structure factor $S_{QQ}(k)$ in the liquid. For the second set $\{\mathbf{G}_2\}$ they have chosen the vectors of the type (220) corresponding to the main peak in $S_{NN}(k)$. Experimental data on $\bar{c}_{QQ}(G_1)$ and $\bar{c}_{NN}(k = 0)$ were used as input in order to determine the volume change η , and the theory was used to predict the values of $\bar{c}_{NN}(G_2)$

and of the Fourier components of the single particle densities at \mathbf{G}_1 and \mathbf{G}_2 . Non-linear effects were included via the three-body quantity $\bar{c}_{NNN}(0,0)$ at long wavelengths. Table (1.8) contains the results obtained for both *RbCl* and *NaCl*.

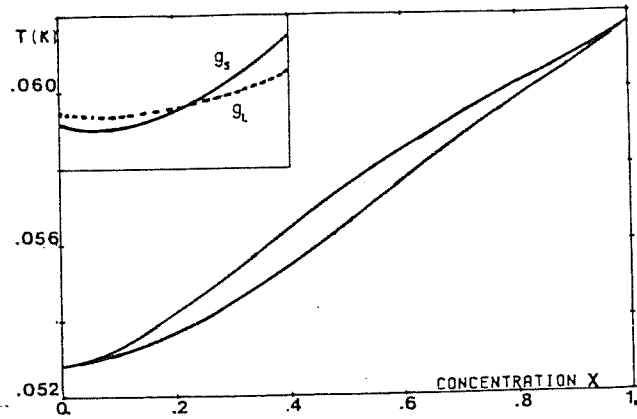
	<i>RbCl</i>	<i>NaCl</i>
$\bar{c}_{NN}(0)$	-7.33 (-7.33)	-6.30 (-6.30)
$\bar{c}_{QQ}(\mathbf{G}_1)$	0.75 (0.75)	0.72 (0.72)
$\bar{c}_{NN}(\mathbf{G}_2)$	0.29 (0.29)	0.28 (0.15)
$\bar{c}_{NNN}(0,0)$	-105	-31
η	0.140 (0.142)	0.250 (0.250)
$\rho_{\mathbf{G}_1}$	0.46	0.53
$\rho_{\mathbf{G}_2}$	0.36	0.42

Table 1.8: Detailed numerical predictions on $\bar{c}_{NN}(\mathbf{G}_2)$, $\bar{c}_{NNN}(0,0)$, $\rho_{\mathbf{G}_1}$, and $\rho_{\mathbf{G}_2}$ for *RbCl* and *NaCl* compared with experimental data in bracket. From ref.[90]

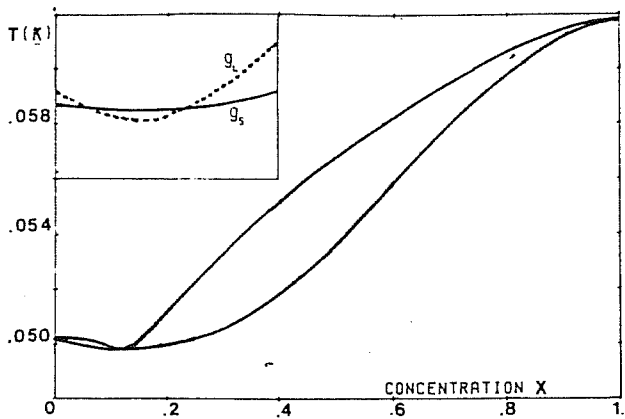
The predicted value of $\bar{c}_{NN}(\mathbf{G}_2)$ for *RbCl* is in good agreement with experiment, and the value of $\bar{c}_{NNN}(0,0) = -105$ is of the same order of magnitude as that found by Ramakrishnan and Yussuoff for the corresponding three-body function in liquid argon. In the case of *NaCl* the prediction of $\bar{c}_{NN}(\mathbf{G}_2)$ is semiquantitative where the value of $\bar{c}_{NNN}(0,0)$ is only 1/3 of that for *RbCl*. In both cases the fourier components of the density are quit similar in magnitude and behaviour^{90,94}.

Barrat et al⁸⁷ have examined the effective liquid approximation (ELA) the freezing of hard-sphere binary mixtures. The fluid-solid phase diagram for disordered allows changes character on varying the relative sizes of the components. This results are shown in fig. 1.13. As the size ratio α is lowered from unity the phase diagram in the temperature-concentration plane is found to evolve from a spindle shape (full miscibility in both phases with solid enriched in large spheres, fig.(1.13a), for $1 > \alpha > 0.94$) into an azeotropic diagram (fluid mixture stable below melting temperature of pure components over a finite concentration range, for $0.94 > \alpha > 0.92$, fig.(1.13b)) and finally into an entectic diagram (with phase separation in the solid, for $0.92 > \alpha > 0.85$, fig(1.13c)). As the size ratio approaches 0.85, the solubility of the large spheres into the solid of small ones shrinks to zero. Partial contact is thus made with the empirical Hume-Rothery rule, which state that the formation of a disordered solid alloy is very unlikely if the atomic sizes differ by more than 15%.

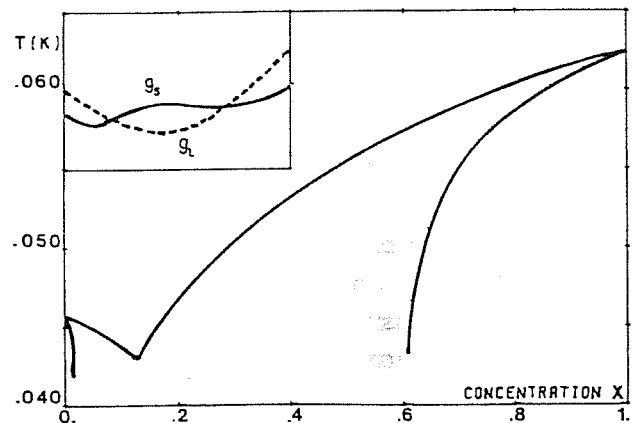
The liquid-solid phase diagram of the restricted primitive model (RPM) for ionic liquids, i.e. a mixture of charged hard spheres of the same diameter



(a)



(b)



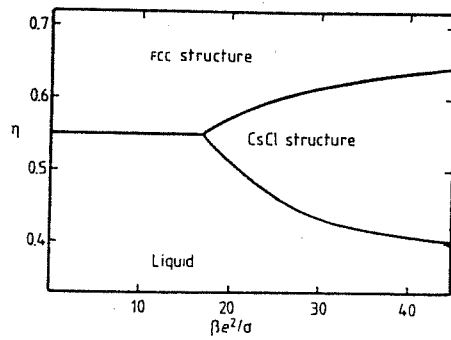
(c)

Figure 1.13: Fluid solid phase diagram for a hard sphere mixture under atmospheric pressure. T is the freezing temperature while $x = x_2$ is the number concentration of large spheres. Inset: schematic representation of the concentration dependence of the solid and fluid free enthalpies at a given pressure and temperature. (a): for $\alpha = 0.95$, (b): for $\alpha = 0.93$ and (c): for $\alpha = 0.90$. From ref.[87].

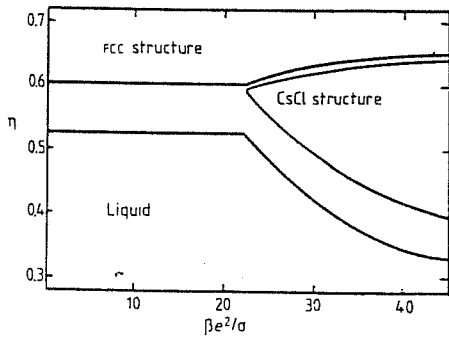
σ and opposite charges, was carried out by Barrat ⁹⁵. He applied the generalized form of the effective-liquid approximation (ELA) ⁶⁰ which was given by Barrat et al ⁹⁶. The thermodynamic equations hence, were given in terms of the following linear combination:

$$\begin{aligned} \rho_s^N(\mathbf{r}) &= \rho_s^+(\mathbf{r}) + \rho_s^-(\mathbf{r}) && \text{(number density)} \\ \rho_s^Z(\mathbf{r}) &= \rho_s^+(\mathbf{r}) - \rho_s^-(\mathbf{r}) && \text{(charge density)} \\ c^{NN}(\mathbf{r}) &= \frac{1}{2}(c_{++}(\mathbf{r}) + c_{+-}(\mathbf{r})) && \text{(number number direct correlation function)} \\ c^{ZZ}(\mathbf{r}) &= \frac{1}{2}(c_{++}(\mathbf{r}) - c_{+-}(\mathbf{r})) && \text{(charge charge direct correlation function)} \end{aligned}$$

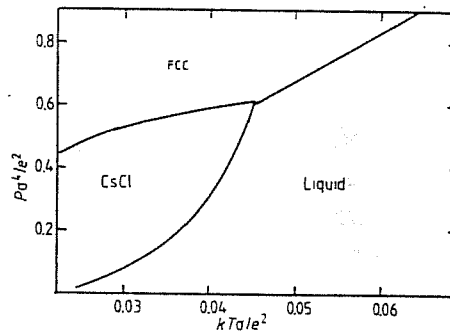
Three different solid structure were considered in this work: a fcc disordered structure, a *CsCl* type structure (a bcc if the charges are removed) and the *NaCl* type structure. The latter was never found to be stable and the main results of this calculation are shown in fig. 1.14. Fig(1.14a) shows the stability limits of the three structures in the β^*, η plane ($\beta^* = \beta e^2 / \sigma$ is the reduced coupling constant). In the low β^* limit (high temperature), the fcc and the liquid phase are stable, whereas in the high β^* limit (low temperature) a stable *CsCl* phase appears. Fig.(1.14b and c) shows the phase diagram in the β^*, η plane and in the T^*, P^* plane respectively ($T^* = k_B T \sigma / e^2, P^* = P \sigma^4 / e^2$). The point $\beta^* = 22, P^* \simeq 0.6$ where the three coexistence lines intersect in the T^*, P^* plane is the liquid-solid-solid triple point of the system.



(a)



(b)



(c)

Figure 1.14: The stability limits of the liquid, CsCl and fcc phases in the β^* , η plane is shown in (a), whereas in (b) the phase diagram in the β^* , η plane and in (c) the phase diagram in the T^* , P^* plane. From ref.[95]

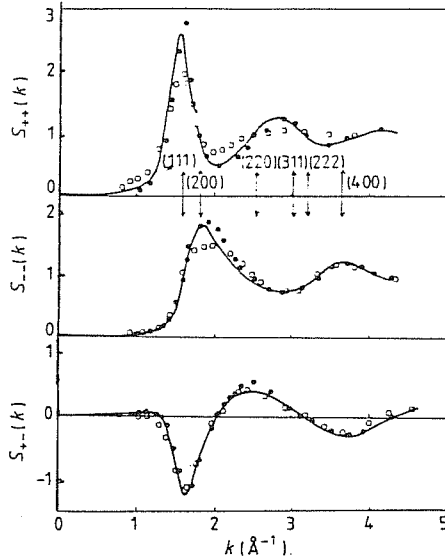


Figure 1.15: *Partial structure factors of molten $SrCl_2$ near freezing, from diffraction data of McGreevy and Mitchell [97, circles], RI simulation of de Leeuw [99, dots] and MHNC theory (curves). The location of the first few stars of reciprocal lattice vectors of the fluorite type structure is indicated, after adjustment of the (111) star to the peak of $S_{++}(k)$.*

1.6.4 Freezing and Superionic Transition In $SrCl_2$

Partial structure factors have also been determined by neutron diffraction for a number of divalent metal-ion halides in the liquid state. We refer in particular to the data on molten strontium chloride by McGreevy and Mitchell⁹⁷. From an examination of the data on the main features of the pair correlation function $g_{\alpha\beta}(r)$ and the partial structure factors, one can already perceive a correlation with the fact that molten $SrCl_2$ freezes into superionic phase anion-disordered, having the fluorite structure. In particular, the main peak in the $Sr-Sr$ partial structure factor is very strong, reflecting ordering of the cations under Coulomb repulsions⁹⁸, and may be put in correspondence with the (111) star of RLV in the fluorite structure (fcc lattice with a two-ion basis). On the other hand the Cl-Cl structure factor shows a relatively broad and low peak overlying the (200) star, indicating a noticeably poorer state of ordering for the halogens in the melt. Fig. 1.15 illustrates the partial structure factors. In contrast with the alkali chlorides, which freeze into a normal fcc phase with a volume change of order 20 – 30%, the volume change on freezing for superionic fluorites is small, of order a few percent.

Application of the density functional approach to freezing has been first made for $SrCl_2$ ⁹⁰ by including only the (111) star. The Fourier expansion of the singlet densities in the solid was expressed by

$$\rho_{is}(\mathbf{r}) = \rho_{is} + \rho_{is} \sum_{\mathbf{G} \neq 0} \rho_{i\mathbf{G}} \exp[i\mathbf{G} \cdot \mathbf{r}] \quad (1.6.13)$$

for $i = 1, 2$. The equation for the difference in the thermodynamic potentials $\Delta\Omega$ between the two phases, which should be equated to zero at coexistence, is

$$\frac{\Delta\Omega}{k_B T} = -(\rho_s - \rho_l)V + \frac{1}{2}\left(\frac{\rho_s^2}{\rho_l^2} - 1\right)\bar{c}_{NN}(0) + \frac{1}{2}\sum_{i,j}\sum_{\mathbf{G}\neq 0}\bar{c}_{ij}(\mathbf{G})\rho_{i,\mathbf{G}}\rho_{j,\mathbf{G}}, \quad (1.6.14)$$

the compressibility appearing through $\bar{c}_{NN}(0)$. Table (1.9) reports the numerical results obtained, where one can see that the agreement with experiment is not quantitative for the values of $\bar{c}_{+-}(\mathbf{G}_1)$ and $\bar{c}_{--}(\mathbf{G}_1)$, and probably this is due to the use of only one set of reciprocal lattice vectors. The negative value of $\bar{c}_{NQ}(0)$ indicates that the molar volume of the cations is greater than that of the anions.

$SrCl_2$	theory	experiment
$\bar{c}_{NQ}(0)$	-12	
$S_{NN}(0)$	0.066	0.066
$\bar{c}_{++}(\mathbf{G}_1)$	-0.46	-0.46
$\bar{c}_{+-}(\mathbf{G}_1)$	-2.90	-2.50
$\bar{c}_{--}(\mathbf{G}_1)$	-1.20	-1.80
η	0.024	0.024
$\rho_{+,\mathbf{G}}$	0.42	
$\rho_{-,\mathbf{G}}$	0.24	

Table 1.9: *Numerical results of microscopic theory for $SrCl_2$. From ref.[90,94]*

It is suggested that the negative sign may originate from the large charge (+2e) on the cations, which tends to lead to a “classical Wigner lattice” in the high temperature solid. The hole generated around a cation is related to Coulomb repulsion rather than to the ionic core radius.

Although a non-linear set of equations was solved in this calculation, the values of the Fourier components $\rho_{i,\mathbf{G}}$ agree with those obtained by a linearisation scheme that was proposed by March and Tosi¹⁰⁰ in the case of $BaCl_2$, also freezing into superionic phase, namely

$$\rho_{-,\mathbf{G}} = \frac{\bar{c}_{+-}(\mathbf{G})\rho_{+,\mathbf{G}}}{(\rho_l/\rho_{-,s}) - \bar{c}_{--}(\mathbf{G})} \quad (1.6.15)$$

The main conclusion is that the anionic order parameters are only a fraction of the dominant cationic order parameters associated with (111) star, as if phase transition is caused by primary freezing of the cationic component, at the same time modulating the anionic singlet density.

An extended calculation to include both the first two stars of reciprocal lattice vectors, i.e. the (111) which is placed in correspondence with the

main peak in measured cation-cation structure factor in the liquid and the (200) which falls near the main peak in the anion-anion structure factor, has been carried out by Rovere and Tosi¹⁰¹. They confirm the conclusion of D'Aguanno et al, that yields $|\rho_{-,G}| \gg |\rho_{+,G}|$. They have also considered the superionic-to-normal transition with cooling of solid $SrCl_2$, viewing it as a process of continuous freezing of modulated anionic component in the field of the metal-ion sublattice, i.e. a continuous growth of the (200) anionic order parameter from its finite value near melting. The evaluation of this continuous transition yields semiquantitative agreement with the observed behaviour of Bragg diffraction intensities and the heat capacity anomaly across the superionic transition.

1.6.5 Extension to Shear Deformed and Dislocated Crystals

The density functional theory seems to describe well the freezing transition, as we have seen in the previous subsections, for different systems. Since the perfect crystalline solid and the liquid are both covered by this theory, density configuration representing intermediate state can also be explored usefully. The extension of the DFT to shear-deformed and dislocated crystals will be discussed here in brief.

Michael et al¹⁰² has proposed a systematic method for calculating the elastic constant of a dense medium in terms of the particle correlation function which characterize the structure of that medium. When a stress is applied to a crystal the strain which develops, measured by the elastic constants, can be described in terms of changes in the reciprocal lattice vectors of the unstressed, unstrained lattice.

Within the frame of DFT the change in the grand thermodynamic potential between the unstressed solid and the uniform liquid, eqn.(1.6.10), can be written in Fourier analysis (for one component system) as

$$\frac{\Delta\Omega}{Nk_B T} = (-1 + \bar{c}(0))\eta + \frac{1}{2}\bar{c}(0)\eta^2 + \frac{1}{2} \sum_{\mathbf{G} \neq 0} \bar{c}(\mathbf{G})\rho_{\mathbf{G}}^2, \quad (1.6.16)$$

where η is fractional volume change upon freezing, $\bar{c}(\mathbf{G})$ are the Fourier components of the direct correlation function of the liquid, and $\rho_{\mathbf{G}}$ are the Fourier components of the spatial density expressed in eqn.(1.6.11). A homogenous shear deformation ϵ changes the reciprocal lattice vectors \mathbf{G} to $\mathbf{G} \cdot (\mathbf{1} + \epsilon)^{-1}$. Then the difference in the grand thermodynamic potential between the deformed solid and the undeformed solid is

$$\frac{\Delta\bar{\Omega}}{Nk_B T} = -\frac{1}{2} \sum_{\mathbf{G} \neq 0} \left(\bar{c}(\mathbf{G} \cdot (\mathbf{1} + \epsilon)^{-1}) \rho_{\mathbf{G} \cdot (\mathbf{1} + \epsilon)^{-1}}^2 - \bar{c}(\mathbf{G}) \rho_{\mathbf{G}}^2 \right). \quad (1.6.17)$$

Using the fact that $\rho_{\mathbf{G}} \rightarrow \rho_{\mathbf{G}} + O(\epsilon)$ and that the first derivative of the Fourier components $\bar{c}(\mathbf{G})$ with respect to the reciprocal lattice vector is zero when $\bar{c}(\mathbf{G})$ correspond to a peak in the structure factor, eqn.(1.6.17) can be simplified to read

$$\frac{\Delta\bar{\Omega}}{Nk_B T} = \frac{1}{4} \sum_{\mathbf{G} \neq 0} \sum_{i,j} \sum_{k,l} \mathbf{G}_i \mathbf{G}_j \epsilon_{ij} \epsilon_{kl} \left(\frac{\partial^2 \bar{c}(\mathbf{G})}{\partial \mathbf{G}_j \partial \mathbf{G}_l} \right) \rho_{\mathbf{G}}^2. \quad (1.6.18)$$

But to the order in which eqn.(1.6.18) is valid, the change in molar Helmholtz free energy is related to $\Delta\Omega$ via

$$\begin{aligned} \Delta a &= -\Delta\Omega/N \\ &= \frac{1}{2} \sum_{ij} e_{ij} \epsilon_i \epsilon_j \quad (\text{vigot notation}) \quad . \end{aligned} \quad (1.6.19)$$

Then by combining eqn(1.6.19) with eqn.(1.6.18) one gets the elastic constants e_{ij} of the solid. This results can be compared with the one first derived by Ramakrishnan ¹⁰³, namely

$$e_{ij} = k_B T_m \sum_{\mathbf{G} \neq 0} A_{ij} \mathbf{G}^2 \bar{c}''(\mathbf{G}) \rho_{\mathbf{G}}^2 \quad (1.6.20)$$

where A_{ij} are geometric coefficients, \mathbf{G} is the reciprocal lattice vector corresponding to the first peak in the structure factor, and T_m is the melting temperature.

Michael et al ¹⁰² have extended their formulation to binary mixtures, where the difference in the grand potential between the solid and the liquid was introduced in terms of the charge-charge, number-number and number-charge correlation functions that were first introduced by March and Tosi ¹⁰⁰ for binary systems in the course of studying freezing of alkali halides and binary systems. They have also considered the nematic state of a liquid crystal, where the molecular centers of gravity are disordered as in a liquid, but with a statistically parallel orientation of the long axes of the molecules along an axis (the director \mathbf{n}). The nematic phase was also studied by Singh ¹⁰⁴ using the basic idea of the density functional approach.

In the case of dislocated crystals, Ramakrishnan ¹⁰³ pointed out that a screw dislocation is a topological singularity in the phase of the density wave representing the perfect crystal, characterized by the fact that on going around it the phase of the order parameter changes by $2\pi n$. In the case of a crystal with a screw dislocation with its core along the z axis, one has

$$\rho(\mathbf{r}) = \rho_l (1 + \eta(\mathbf{r}) + \sum_{\mathbf{G} \neq 0} \rho_{\mathbf{G}}(x, y) \exp[i\mathbf{G} \cdot \hat{e}_z b / 2\pi] \exp[i\mathbf{G} \cdot \mathbf{r}]) \quad (1.6.21)$$

where $\hat{e}_z b$ is the Burgers vectors of dislocation and $\rho_G(x, y)$ is a smooth function of x and y , going to zero at the origin (the order parameter has to vanish there for a topological defect) and having the crystalline solid value for $(x^2 + y^2) \rightarrow \infty$. With the use of an energy functional similar to eqn.(1.6.10) and functional minimization with respect to $\rho(\mathbf{r})$, a differential equation for the vortex structure ($\rho_G(x, y)$) will be found.

Chapter 2

FREEZING OF A CLASSICAL PLASMA AND OF ALKALI METALS

INTRODUCTION

In this chapter we are going to discuss the application of the density functional theory to the freezing of the classical one-component plasma (OCP) and of the alkali metals. Before entering the description of our calculations, we discuss in section 1 the reasons behind choosing the OCP as a reference system for liquid alkali metals. In fact, the structure factor of the OCP, at the appropriate value of the coupling strength Γ (calculated from the nominal ionic valence, temperature and density of the metal) is closely similar in the region of the main peak and beyond to the measured structure factor of liquid alkali metals, near their freezing point and over a range of temperature above it. This was first noticed by Minoo et al. In the small angle scattering region this similarity is lost: electronic screening, which reduces the ionic plasma excitation to the longitudinal acoustic mode, simultaneously changes the k^2 behaviour of the OCP structure factor to the Ornstein-Zernike behaviour of the structure factor of the metal ($S(k) \rightarrow 0$) proportional to the compressibility). The evaluation of the long-wavelength limit of the liquid structure factor, as considered by Chaturvedi et al, is discussed in the same section, together with the calculation of the full structure factor of alkali metals near freezing as it was calculated by Pastore and Tosi. In addition, the alternative use of the OCP as a reference system in liquid-metal physics, concerning the calculation of the Helmholtz free energy using the variational principle based on the Gibbs-Bogolyubov inequality, is discussed.

Section 2 illustrates the main quantities (i.e. the Helmholtz free energy and the grand-canonical potential), which as functionals of the one-particle density provide the starting point for the density functional formalism discussed in section 3, following Mermin.

In section 4, we describe the density functional theory of freezing, that amounts to considering the hot solid as an inhomogeneous system having a periodic one-particle density $\rho_s(\mathbf{r})$. The set of equations needed to study freezing of the fluid into a prescribed crystal lattice structure are given. The evaluation of the entropy and the volume changes across the phase transition is presented and a discussion of the thermodynamic inconsistency, which arises in the theory because of the approximations involved, is reported following the previous work by D'Aguanno et al. In this section we also explicitly show the relationship between the microscopic order parameters $\rho_{\mathbf{G}}$ (the Fourier components of the periodic density at the reciprocal lattice vectors \mathbf{G}) and the Debye-Waller factors of the crystal at melting. If the density profile $\rho_s(\mathbf{r})$ of the solid phase in real space is represented by a superposition of Gaussian centered at the various lattice sites, the Gaussian

widths are immediately related to the Lindemann's ratio.

Freezing of the OCP on a rigid background into the bcc and the fcc structure is evaluated in section 5, taking account of the recent progress in the determination of the thermodynamic functions of this model fluid by computer simulation. The known difficulties of the theory relating to the order parameter at the (200) star of reciprocal vectors (RLV) is also discussed.

The relationship between Wigner crystallization in the classical ionic plasma and the liquid-solid transition of alkali metals is examined in section 6 and 7. Freezing of the OCP on a deformable background is discussed in section 7. We show that, on allowing for long-wavelength deformability of the background, the appearance of a volume change on freezing into the bcc structure is accompanied by reduced stability of the fluid phase and by an increase in the entropy of melting. Next, freezing of alkali metals into the bcc structure is evaluated, taking their ionic pair structure as that of an ionic plasma reference fluid screened by conduction electrons and asking that the correct ionic coupling strength at liquid-solid coexistence should be approximately reproduced.

2.1 Classical One-Component Plasma as a Reference System

The simplest model of a Coulombic system is the so-called one-component classical plasma (OCP), a system of identical point charges, interacting purely through the coulomb potential and immersed in a rigid uniform background of opposite charge to ensure charge neutrality. Although this model is an over-simplification, it serves as a prototype for more “realistic” systems and can be considered as a limiting case of real matter¹⁰⁵. The basic parameter which characterizes the model system is the coupling strength parameter $\Gamma = \beta e^2/a$, where $\beta = (k_B T)^{-1}$ and $a = (4\pi n/3)^{-1/3}$ in terms of the particle density n . The OCP has been considered by many authors as a reference fluid for perturbative calculations of thermodynamic and structural properties of liquid metals and we are going to discuss some of these aspects in this section.

The choice of the OCP as a reference system is particularly successful for liquid alkali metals. It was first noticed by Minoo et al¹⁰⁶ that the structure factor of the OCP, at the appropriate value of the coupling strength Γ is closely similar in the region of the main peak and beyond to the measured structure factor of the liquid alkali metals. In the small angle scattering region this similarity is lost, since electronic screening is crucial in the liquid metal. Chaturvedi et al^{107,6} have proposed a way to include the electronic screening through a random phase approximation on the indirect ion-ion interaction, that arises via the response of the sea of conduction electrons to the ionic cores.

The evaluation of the long-wavelength limit of the liquid structure factor corresponds to a calculation of the isothermal compressibility by the “method of long waves”, i.e. one determines through it the value of dynamic compressibility which is consistent with the speed of long acoustic waves¹⁰⁸. Chaturvedi et al⁶ considered the liquid alkali metals as constituted of a fluid of classical ions and degenerate electron gas. In such a system near freezing the bare ion-ion coupling is very strong ($\Gamma \simeq 200$), while the electron-electron coupling is by comparison only moderately strong ($r_s = a/a_o$, where a_o is the Bohr radius, with $r_s \sim 3 - 6$). The basic assumption made was that the ionic liquid and electron gas are weakly coupled to each other through a bare electron-ion pseudopotential $v(k)$, which can be treated by second-order perturbation theory. Then structure factor $S(k)$ of the liquid metal can be written as^{108,6}

$$S(k) = S_o(k)[1 - \bar{c}_s(k)S_o(k)]^{-1} \quad , \quad (2.1.1)$$

or equivalently the direct correlation function $\bar{c}(k)$ is given by

$$\bar{c}(k) = \bar{c}_o(k) + \bar{c}_s(k) \quad . \quad (2.1.2)$$

Here $S_o(k)$ and $\bar{c}_o(k)$ are the structure factor and the direct correlation function of the bare ionic system on a rigid electron background, i.e. those of the OCP if one neglects the non-Coulombic terms in the direct ion-ion interaction, while

$$\bar{c}_s(k) = \frac{nk^2v^2(k)}{4\pi e^2k_B T} [1 - 1/\epsilon(k)] \quad , \quad (2.1.3)$$

is given by the usual expression for the contribution of electronic screening to the effective ion-ion potential in terms of $v(k)$ and of the dielectric function $\epsilon(k)$ of the homogeneous electron gas.

In order to examine how eqn.(2.1.1) accounts for the isothermal compressibility K_T of liquid alkali metals through the Ornstein-Zernike relation,

$$\lim_{k \rightarrow 0} S(k) = nk_B T K_T \quad , \quad (2.1.4)$$

one starts from the well-known forms at long wavelength for the structure factor of the OCP ¹⁰⁹,

$$\lim_{k \rightarrow 0} S_o(k) = \frac{k_B T k^2}{4\pi n e^2} [1 + k^2/k_i^2]^{-1} \quad , \quad (2.1.5)$$

and for the electronic function ¹¹⁰,

$$\lim_{k \rightarrow 0} \epsilon(k) = 1 + k_e^2/k^2 \quad . \quad (2.1.6)$$

On the other hand, adopting for the electron-ion pseudopotential the simple Ashcroft for $v(k) = -(4\pi e^2/k^2) \cos(kr_c)$ ¹¹¹, one has

$$\lim_{k \rightarrow 0} v(k) = -4\pi e^2/k^2 + 2\pi e^2 r_c^2 \quad , \quad (2.1.7)$$

the quantity r_c being the Ashcroft core radius. The quantity k_e in eqn.(2.1.6) is the inverse screening length of the electron gas, related to its compressibility ¹¹⁰, while in eqn.(2.1.5) k_i is identified as "inverse screening length" of the OCP, which is calculated from the excess internal energy u per particle of the OCP, in units of $k_B T$, as ¹⁰⁵

$$k_D^2/k_i^2 = 1 + \frac{1}{3}u + \frac{1}{9} \frac{du}{d\Gamma} \quad . \quad (2.1.8)$$

Here, k_D is the Debye-Hückel inverse screening length,

$$k_D = (4\pi n e^2/k_B T)^{1/2} \quad . \quad (2.1.9)$$

The use of the eqns.(2.1.5)-(2.1.7) in eqn.(2.1.1) leads to

$$S(0) = \left(\frac{k_D^2}{k_e^2} + \frac{k_D^2}{k_i^2} + k_D^2 r_c^2 \right)^{-1} \quad (2.1.10)$$

Table (2.1) reports the numerical results that were obtained, using the values of r_c deduced from an overall fit ¹¹² of the phonon dispersion curve in crystalline alkali metals with the corresponding values of k_e from Singwi et al ¹¹³, compared with experimental data ^{114,115}. The good agreement indicates that their model is giving a consistent account of sound waves in the liquid and in the solid. The only exception may be Lithium, where $S(0)$ appears to be low when compared with theoretical calculations ¹¹⁶ of the compressibility.

	$T(K)$	Γ	$r_c(\text{\AA})$	r_s	$S(0)_{calc}^a$	$S(0)_{expt}^b$
<i>Li</i>	453	211	0.741	3.299	0.0158(0.0201)	
<i>Na</i>	371	208	0.894	4.049	0.0215	0.0240(0.0233)
	437	163	0.894	4.085	0.0289	0.0322(0.0308)
<i>K</i>	337	186	1.180	5.030	0.0231(0.0212)	0.0247(0.0225)
	408	153	1.180	5.072	0.0295(0.0270)	0.0312(0.0283)
<i>Rb</i>	312	188	1.270	5.388	0.0236(0.0207)	(0.0220)
<i>Cs</i>	301	181	1.390	5.786	0.0235(0.0202)	(0.0237)

Table 2.1: Structure factor at long wavelength for liquid alkali metals. The superscript :(a) Values in parentheses include an effective mass correction in the calculation of k_e^2 , as discussed by Price et al [112]. (b) Values in parentheses are deduced from the sound velocities reported by Webber and Stephens [115], with a correction for the difference between the adiabatic and isothermal compressibilities. The other values are from Greenfield et al [114]. From ref.[6]

The full structure factor of alkali metals near freezing was calculated by Pastore and Tosi ¹¹⁷, starting from the classical plasma of bare ions as reference liquid (OCP). The indirect ion-ion interaction arising from electronic screening is treated by an optimized random phase approximation (ORPA), imposing physical requirements as in the original ORPA scheme developed by Weeks et al ¹¹⁸ for liquids with strongly repulsive core potentials. An independent justification of the accuracy of the theory was first given by coupling its results with computer simulation data on liquid *Rb*.

Figure 2.1 shows the result of $S(k)$ for alkali metals compared with X-ray diffraction data ^{114,119}. Two choices were adopted for the indirect ion-ion interaction, both based on the Ashcroft form for $v(k)$. The first choice is the potential adjusted by Price et al ¹¹² to phonon dispersion curves (model I),

and in the second choice (model II) they have used the results of Vashishta and Singwi ¹²⁰ for the dielectric function in eqn.(2.1.3) and have at the same time readjusted the core radius r_c to fit experimental values of $S(0)$ ^{13,121}, related to the isothermal compressibility of the liquid metal through the Ornstein-Zernike relation. The results of this calculation shows an overall good representation for sodium, potassium and cesium in the small angle scattering region as well as in the height of the main peak, except for lithium, when one uses a very simple form for the electron-ion potential adjusted to the liquid compressibility, fig 2.2. It is clear from table (2.2) that the theoretical values are sensitive to the details of the electron-ion coupling (entering the results through core radius r_c), although the comparison with the corresponding peak heights for the OCP in the same table shows that the effect of this coupling is rather small outside the small-angle scattering region (and excluding for the moment the case of Li from consideration). From the above discussion it is clear that the OCP structure factor at the appropriate value of the coupling Γ reproduce very well the measured structure factor of real alkali metals near freezing, except in the small-angle scattering region. It should be stressed for latter reference that indeed the correction due to electronic screening have essentially died out when one reaches the region of wave number corresponding to the main peak.

	r_s	Γ	σ/a	$r_c(\text{\AA})$	$S(0)$	S^{peak}	S_o^{peak}
<i>Li</i>	3.28	212	1.463	0.74	0.016	3.11	3.21
				0.59	0.031*	2.38	
<i>Na</i>	4.05	211	1.462	0.95	0.017	3.21	3.20
				0.86	0.0256#	2.98	
<i>K</i>	5.02	187	1.450	1.26	0.020	3.11	3.00
				1.21	0.0241#	3.11	
<i>Rb</i>	5.42	185	1.449	1.33	0.021	3.10	2.99
				1.35	0.0245*	3.18	
<i>Cs</i>	5.77	181	1.447	1.44	0.021	3.14	2.95
				1.43	0.0256#	3.14	

Table 2.2: Input data and results for $S(0)$ and S^{peak} for liquid alkalis. For each metal, the two rows refer to model I and II. Measured values of $S(0)$ are in parentheses #: from ref. [119]; *: from ref. [121] and have been fitted to determine the values reported for r_c in model II. S^{peak} are the calculated values for the height of the main peak, the corresponding theoretical values for the OCP being given in the last column. In the case of Na the values of S_o^{peak} and S^{peak} are sensitive to the input data [24,123] on the free energy of the OCP. From ref. [117].

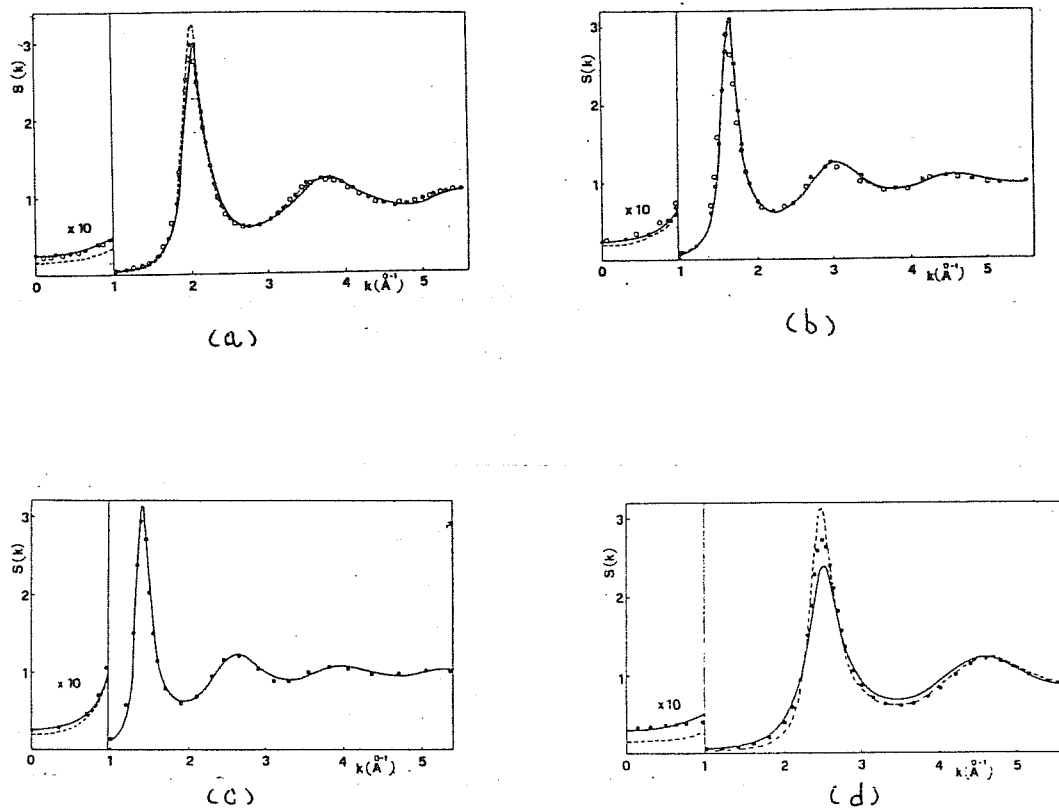


Figure 2.1: Structure factor of alkali metals, from model I (broken curve) and model II (full curve). a: Liquid Na at 100°C the experimental data are from X-ray diffraction of Huijben and Van der Lugt [119] (dots) and of Greenfield et al. [114] (circles). b: Liquid K at 5°C the experimental data form ref. [119] (dots) and from ref.[114] (circles). c: Liquid Cs at 30°C the experimental data from ref. [119] (dots). d: Liquid Li at 190°C the experimental data are taken from Waseda [121] (dots). From ref. [117]

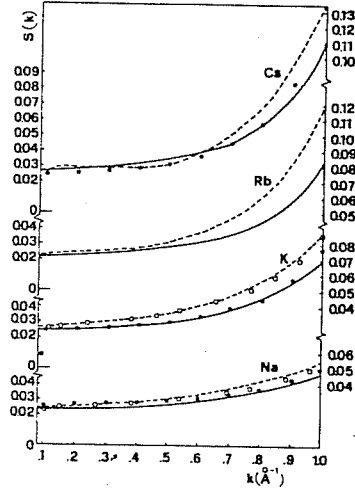


Figure 2.2: Structure factor of liquid Na, K, Rb and Cs in the small angle scattering region ($0.1\text{\AA}^{-1} \leq k \leq 1\text{\AA}^{-1}$). The experimental data are from Waseda [121] (broken curve), Huijben and Van der Lugt [119] (dots) and Greenfield et al.[114] (circles). The theoretical results (full curve) are from model II, at temperatures equal to those of Waseda's data (105°C for Na, 70°C for K, 40°C for Rb and 30°C for Cs). The other experimental data for Na and K are at slightly lower temperatures (100°C for Na and 65°C for K). From ref. [117]

A rather different use of the OCP as a reference system in liquid-metal physics concerns the calculation of the Helmholtz free energy using the variational principle based on Gibbs-Bogolyubov inequality. This ensures an upper bound to the Helmholtz free energy F of a liquid giving by

$$F \leq F_o + \langle \delta H \rangle_o \quad , \quad (2.1.11)$$

where F_o is the Helmholtz free energy of a reference liquid at the same density n and temperature T , while $\langle \delta H \rangle_o$ is the difference between the Hamiltonians of real and reference liquids evaluated with the distribution function of the reference. Ross et al ¹²³ observed that the OCP reference system gives rise for alkali metals to a better (i.e., lower) variational upper bound to the free energy than does the hard sphere model, and found good agreement with simulations for a model of liquid Li. In the case of liquid Na and Al, Mon et al ¹²⁴ used also the variational principle based on Gibbs-Bogolyubov inequality in conjunction with the hard sphere and the OCP reference systems. In their work, for liquid Na, the OCP gives the lower variational bound to the free energy, which was further supported by fitting the measured structure ¹¹⁴ factor with the OCP structure factor. Liquid Al, on the other hand, described by the hard sphere reference system when exchange-correlations to the pair potentials were properly included.

Thermodynamic calculation for liquid metals using the OCP as a reference system were performed by Young ¹²⁵ within the framework of the Gibbs-Bogolyubov method. The OCP Helmholtz free energy per ion is:

$$F_o = \frac{3}{2}k_B T + V_o - T S_o \quad , \quad (2.1.12)$$

where V_o and S_o are the potential energy and the entropy respectively. The OCP reference system is characterized by the effective coupling strength $\Gamma^* = (Z^*e)^2/ak_B T$, where $a = (4\pi n/3)^{-1/3}$ and Z^* is an effective ionic valence which is determined variationally (having assumed density, temperature and ionic mass as those of the real system). The free energy of the liquid was written as:

$$F = F_o + \frac{1}{2} \int d\mathbf{r} (u(\mathbf{r}) - u_o(\mathbf{r})) g_o(\mathbf{r}/a, \Gamma^*) + U(n) \quad , \quad (2.1.13)$$

or alternatively

$$F = F_{id} - T \Delta S_o + \frac{1}{2} \int d\mathbf{r} (u(\mathbf{r})) g_o(\mathbf{r}/a, \Gamma^*) + U(n) \quad , \quad (2.1.14)$$

where the subscript *id* corresponds to the ideal classical gas with $Z^* = 0$, $\Delta S_o = S - o - S_{id}$, $u_o(\mathbf{r})$ and $g_o(\mathbf{r}/a, \Gamma^*)$ are the pairwise interaction and the radial distribution function of the OCP system, and $u(\mathbf{r})$ is the ion-ion interaction. Finally, $U(n)$ is a purely density dependent term arising from the sea of conduction electrons. The optimal Z^* is found from

$$\left(\frac{\partial F}{\partial \Gamma^*} \right)_{n,T} \equiv (Z^*/2\Gamma)(\partial F/\partial Z^*)_{n,T} = 0 \quad , \quad (2.1.15)$$

or, more explicitly

$$-T \partial \Delta S_o / \partial \Gamma^* + \frac{1}{2} n \int d\mathbf{r} (u(\mathbf{r})) \partial g_o(\mathbf{r}/a, \Gamma^*) / \partial \Gamma^* = 0 \quad . \quad (2.1.16)$$

The entropy is given by

$$S = S_{id} + \{ \Delta S_o + T(\partial \Delta S_o / \partial T)_{n,Z^*} \} - \frac{1}{2} n \int d\mathbf{r} (u(\mathbf{r})) [\partial g_o(\mathbf{r}/a, \Gamma^*) / \partial T]_{n,Z^*} \quad . \quad (2.1.17)$$

Of the two terms in curly brackets, the first combine with S_{id} to give S_o , while the second cancels against the integral on invoking eqn.(2.1.16) after noting that $T(\partial/\partial T)_{n,Z^*} = -\Gamma(\partial/\partial \Gamma)_{n,T}$. The final result is

$$S = S_o$$

that is the entropy of the liquid metals is given in the variational approach by the entropy of the OCP at the value of the coupling strength which minimizes the free energy.

Montella et al ¹²⁶ have combined the variational treatment for the structure-dependent part of the free energy with the electron-theory treatment given earlier by Price ¹²⁷ on liquid Na for the structure-independent part $U(n)$ part of the internal energy, in order to have a complete evaluation of thermodynamic properties. Eqn.(2.1.14) is the free energy equation, with $U(n)$ given by

$$U(n) = E_g + \frac{1}{2} \lim_{r \rightarrow 0} [u(r) - e^2/r] - \frac{1}{2} \int dr u(r) + \alpha n \int dr [v(r) + e^2/r] \quad (2.1.18)$$

where E_g is the ground-state energy of the homogeneous electron gas, $v(r)$ is the bare electron-ion potential and α is a parameter introduced by Price to fit the experimental pressure P for given n and T . This approach allows the evaluation of higher thermodynamic derivatives such as thermal coefficient γ_V of the pressure, the isothermal compressibility K_T , and the ratio of the specific heats. A tabulation of results for the thermodynamic derivatives of the free energy is given in table (2.3) together with experimental values whenever available, the agreement with the data being very reasonable.

	<i>Li</i>	<i>Na</i>	<i>K</i>	<i>Rb</i>	<i>Cs</i>
$\Delta S/k_B$	-2.9(-3.61)	-3.4(-3.45)	-3.7(-3.45)	-3.8(-3.63)	-3.7(-3.56)
C_V/k_B	2.9(3.4)	3.3(3.4)	3.3(3.4)	3.4(3.3)	3.4(3.2)
$\gamma_V(\text{bar}/K)$	24	13(13)	6.6(7.60)	5.2(6.86)	4.4(5.74)
$K_T(10^{-12} \frac{\text{cm}^2}{\text{dyn}})$	9.5(9.43)	20(18.6)	40(38.2)	51(49.3)	65(68.8)
C_p/C_V	1.1(1.07)	1.1(1.12)	1.1(1.11)	1.1(1.15)	1.1(1.20)

Table 2.3: *Thermodynamic properties of liquid alkali near freezing at atmospheric pressure. Measured values in parentheses. From ref.[127].*

It is evident from the above discussion that the use of the OCP as a reference system for perturbative calculations of the thermodynamic properties of liquid metals predicts to a good extent the various thermodynamic derivatives of the free energy. The main drawback is the prediction of the value of the plasma parameter appropriate to the liquid metal, which is significantly

lower (i.e. Z^* is appreciably less than unity) when it is determined variationally from the Gibbs-Bogolyubov inequality for the free energy, leading to some deterioration in the predicted structure factor. This discrepancy has been discussed by Iwamatsu et al ¹²⁸.

The OCP model has been also used as a reference system to reproduce the structure factor in the case of the liquid transition metals by Khanna and Cyrot-Lackman ¹²⁹, with main attention to the first peak of the structure factor. Itami and Shimoji ¹³⁰, on the other hand have applied the OCP model to study the thermodynamic properties of the liquid transition metals. In both calculations it is found that the value of the valence Z^* in the coupling parameter $\Gamma = (Z^*e)^2/ak_B T$ is somewhat larger than unity, which is taken to indicate some effect of s-d hybridisation. Table (2.4) presents some of the thermodynamic quantities of liquid transition metals, based on the use of the OCP as a reference system and compared with experimental data.

	<i>Sc</i>	<i>Ti</i>	<i>V</i>	<i>Cr</i>	<i>Mn</i>	<i>Fe</i>	<i>Co</i>	<i>Ni</i>
<i>T(K)</i>	1833	1973	2173	2173	1533	1833	1823	1773
Γ	100	110	110	120	120	110	110	110
Z^*	1.42	1.47	1.49	1.52	1.30	1.33	1.32	1.30
S_{OCP}	11.87	11.55	11.61	11.34	10.87	11.39	11.49	11.56
S_{exp}	12.05	12.01	12.08	11.58	12.05	12.11	12.08	11.69
C_V^{OCP}	3.91	3.85	3.87	3.88	3.75	3.94	4.01	4.13
C_V^{exp}	4.39	3.53	4.15	3.90	4.56	4.38	4.00	4.46
χ_T^{OCP}	2.31	1.56	1.23	1.01	1.52	1.26	1.23	1.26
χ_T^{OCP}						1.04	0.97	0.98

Table 2.4: *Thermodynamic properties of liquid metals. Entropy S (in units of Nk_B), the valence Z^* calculated from the plasma parameter Γ , heat capacity C_V at constant volume (in units of Nk_B), and isothermal compressibility $\chi_T(10^{-11}m^2N^{-1})$, all compared with available experimental data. From ref.[131]*

The aim of our work in the later parts of this chapter will be to examine

the usefulness of the OCP model as a reference for the liquid-solid transition in the alkali metals, within the density wave theory of freezing. We start in the next section by recalling some general point on the thermodynamic potentials in inhomogeneous systems.

2.2 Thermodynamic Potentials

Useful theories of non-uniform systems have been developed in the last twenty years. These theories are of a variational character and the crucial entity is a functional of the single-particle density that has as a lower bound the exact grand potential of the system. The application to classical fluids was first described by Ebner et al ¹³¹, but similar methods had been used previously for quantum-mechanical systems in the ground state by Hohenberg and Kohn ⁴⁷ and extended to equilibrium states at finite temperature by Mermin ⁴⁷. In this section we are going to illustrate the key quantities $\mathcal{F}[\rho]$ and $\Omega_V[\rho]$ (the Helmholtz free energy and the grand-canonical potential), which are functionals of the one-particle density $\rho(\mathbf{r})$. In the following section we are going to give the density functional formalism and then proceed to describe its use in the theory of freezing.

Let us consider a classical system of N identical particles in a volume V . The Hamiltonian of the system is composed of (i) a term due to the free motion of the particles, (ii) a term corresponding to the interactions of particles with each other and (iii) a term describing the action of an arbitrary external potential depending only on the coordinates of the particles:

$$\mathcal{H}_N = K_N(\{\mathbf{p}_i\}) + V_N(\{\mathbf{r}_i\}) + \Phi_N(\{\mathbf{r}_i\}) \quad , \quad (2.2.1)$$

where

$$K_N(\{\mathbf{p}_i\}) = \sum_{i=1}^N \mathbf{p}_i^2 / 2m \quad ,$$

$$\Phi_N(\{\mathbf{r}_i\}) = \int_V d\mathbf{r} \rho(\mathbf{r}) \phi_{ext}(\mathbf{r}) \quad ,$$

m is the mass of the particles. The potential energy V_N includes any containing walls present in the system and no pairwise additivity is assumed for it. The microscopic density $\rho(\mathbf{r})$ is given by

$$\rho(\mathbf{r}) = \sum_{i=1}^N \delta(\mathbf{r} - \mathbf{r}_i) \quad . \quad (2.2.2)$$

The system, with a prescribed potential μ , is in thermal equilibrium in a bath at temperature T .

We are going to use the grand canonical ensemble to describe the system, because the equilibrium conditions, i.e. the equality of pressure P , temperature T and chemical potential μ are in it easily accessible. Let $f(\mathbf{r}^N, \mathbf{p}^N; N)$ be the probability that a system chosen at random contains

precisely N particles, with coordinates \mathbf{r}^N and momenta \mathbf{p}^N . At equilibrium, $f = f_{eq}$ is

$$f_{eq} = Z_G^{-1} \exp[-\beta(\mathcal{H}_N - \mu N)] \quad , \quad (2.2.3)$$

where the grand canonical partition function is given by

$$Z_G(V, T, \mu) = Tr_{cl}\{\exp[-\beta(\mathcal{H}_N - \mu N)]\} \quad . \quad (2.2.4)$$

Tr_{cl} denotes the usual classical trace operation, that is

$$Tr_{cl} = \sum_{N=0}^{\infty} \frac{1}{N!} \prod_{i=1}^N \int d\mathbf{r}_i \int \frac{d\mathbf{p}_i}{h^3} \dots \quad . \quad (2.2.5)$$

The macroscopic value of a generic operator \hat{A} is defined by taking the configurational average

$$\langle \hat{A} \rangle = Tr_{cl}\{f_{eq} \cdot \hat{A}\} \quad , \quad (2.2.6)$$

and for the equilibrium density $\rho_{eq}(\mathbf{r})$ we have

$$\rho_{eq}(\mathbf{r}) = \langle \rho(\mathbf{r}) \rangle \quad , \quad (2.2.7)$$

starting from the relation between the grand potential Ω and the grand partition function Z_G , one can see the connection between the thermodynamic properties and the grand canonical ensemble, i.e.

$$\beta^{-1} \ln Z_G = -\Omega = PV \quad . \quad (2.2.8)$$

The other thermodynamic functions are the “intrinsic” Helmholtz free energy \mathcal{F} and the Helmholtz free energy F , which are defined as

$$\mathcal{F} = \Omega - \int d\mathbf{r} \rho_{eq}(\mathbf{r}) \phi_{ext}(\mathbf{r}) + \mu \int d\mathbf{r} \rho_{eq}(\mathbf{r}) \quad (2.2.9)$$

and

$$F = \mathcal{F} + \int d\mathbf{r} \rho_{eq}(\mathbf{r}) \phi_{ext}(\mathbf{r}) \quad . \quad (2.2.10)$$

2.3 The Density Functional Formalism

Following Mermin ⁴⁷, we introduce the functional of the probability density f

$$\Omega[f] = Tr_{cl}\{f(\mathcal{H}_N - \mu N + \beta^{-1} \ln f)\} \quad , \quad (2.3.1)$$

which coincides with the grand canonical potential if $f = f_{eq}$,

$$\Omega[f_{eq}] \equiv \Omega(V, T, \mu) \quad . \quad (2.3.2)$$

From the Gibbs-Bogolyubov inequality ¹³² for two arbitrary distribution functions f and g

$$Tr_{cl}(f \ln f) \geq Tr_{cl}(g \ln g) \quad , \quad (2.3.3)$$

one immediately obtains the relation

$$\Omega[f] > \Omega[f_{eq}] \quad (2.3.4)$$

where we have used the relation (2.2.3), (2.3.1) and (2.3.2). Using the same arguments of Hohenberg-Kohn-Mermin ⁴⁷, one can show that for a given interaction potential $V_N(\{\mathbf{r}_i\})$ and chemical potential μ , $\phi_{ext}(\mathbf{r})$ is a functional of $\rho_o(\mathbf{r})$: i.e. $\phi_{ext}(\mathbf{r})$ is uniquely determined by $\rho_o(\mathbf{r})$ if this density is known in all \mathbf{r} points of the system. In fact, one can see from eqn.(2.2.3) that f_{eq} is a function of $\phi_{ext}(\mathbf{r})$ and therefore f_{eq} is a functional of $\rho_o(\mathbf{r})$.

The two key quantities of density functional theory are the functionals

$$\mathcal{F}[\rho] = Tr_{cl}\{f_{eq}(K_N(\{\mathbf{p}_i\}) + V_N(\{\mathbf{r}_i\}) + \beta^{-1} \ln f_{eq})\} \quad (2.3.5)$$

$$\Omega_V[\rho] = \int d\mathbf{r} \rho(\mathbf{r}) \phi_{ext}(\mathbf{r}) + \mathcal{F}[\rho] - \mu \int d\mathbf{r} \rho(\mathbf{r}) \quad . \quad (2.3.6)$$

Let us suppose at this point that $\phi_{ext}(\mathbf{r})$ changes to $\phi'_{ext}(\mathbf{r})$, with consequent change in the Hamiltonian, equilibrium probability density and grand potential given, respectively, by $\mathcal{H}_N \rightarrow \mathcal{H}'_N, f_{eq} \rightarrow f'_{eq}$ and $\Omega \rightarrow \Omega'$. then since $f_{eq} \neq f'_{eq}$,

$$\begin{aligned} \Omega' &= Tr_{cl}\{f'_{eq}(\mathcal{H}'_N - \mu N + \beta^{-1} \ln f'_{eq})\} \\ &< Tr_{cl}\{\rho_o(\mathcal{H}' - \mu N) + \beta^{-1} \ln \rho_o\} \end{aligned} \quad (2.3.7)$$

and hence

$$\Omega' < \Omega + \int d\mathbf{r} (\phi'_{ext}(\mathbf{r}) - \phi_{ext}(\mathbf{r})) \rho(\mathbf{r}) \quad , \quad (2.3.8)$$

with $\rho_o(\mathbf{r})$ being the single-particle density for the distribution function f_{eq} . The inequality in eqn.(2.3.7) remains valid when primed and unprimed quantities are interchanged, and if $\rho_o(\mathbf{r})$ remains unaltered we find

$$\Omega < \Omega' + \int d\mathbf{r} (\phi_{ext}(\mathbf{r}) - \phi'_{ext}(\mathbf{r})) \rho(\mathbf{r}) \quad (2.3.9)$$

adding eqn.(2.3.8) and eqn.(2.3.9) leads to the contradiction $\Omega' + \Omega < \Omega + \Omega'$. Hence the assumption that $\rho_o(\mathbf{r})$ remains the same must therefore be false, since no other approximation has been made. The conclusion drawn is that

for a system with prescribed interparticle potential there is one and only one external potential that gives rise to a particular single-particle density. From this it follows, since $\phi_{ext}(\mathbf{r})$ also determines f_{eq} is a unique functional of $\rho_o(\mathbf{r})$. Then we can conclude the $\Omega_V[\rho(\mathbf{r})]$ reaches its minimum value when $\rho(\mathbf{r}) = \rho_o(\mathbf{r})$, this results being expressed through the relation

$$\left. \frac{\delta \Omega_V[\rho(\mathbf{r})]}{\delta \rho(\mathbf{r})} \right|_{\rho(\mathbf{r})=\rho_o(\mathbf{r})} = 0 \quad . \quad (2.3.10)$$

Keeping in mind the general definition of a functional derivative,

$$\delta G = \int_{y_1}^{y_2} dy A(y, [\Psi(y)]) \delta \Psi(y) \quad (2.3.11)$$

namely

$$\frac{\delta G}{\delta \Psi(y)} = A(y, [\Psi(y)]) \quad , \quad (2.3.12)$$

we can calculate the functional derivative of eqn.(2.3.9) using for $\Omega_V[\rho(\mathbf{r})]$ the expression (2.3.6). In this way we obtain the fundamental equation of the theory

$$\phi_{ext}(\mathbf{r}) + \mu_{in}[\rho_o; \mathbf{r}] = \mu \quad (2.3.13)$$

with

$$\mu_{in} = \frac{\delta \mathcal{F}[\rho(\mathbf{r})]}{\delta \rho(\mathbf{r})} \quad . \quad (2.3.14)$$

In fact, eqn.(2.3.13) is an explicit equation for the equilibrium density if we apply it to the system of N interacting particles introduced in section (2.2). The effect of interactions may be put in evidence by decomposing $\mathcal{F}[\rho]$ into an ideal part $\mathcal{F}_{id}[\rho]$ and a part $\Psi[\rho(\mathbf{r})]$ corresponding to the interactions,

$$\mathcal{F}[\rho] = \mathcal{F}_{id}[\rho] - \Psi[\rho(\mathbf{r})] \quad . \quad (2.3.15)$$

The ideal part can be easily determined from non-interacting system ($V_N = 0$) as

$$\mathcal{F}_{id}[\rho] = \beta^{-1} \int d\mathbf{r} [\ln(\rho_o(\mathbf{r})\Lambda) - 1] \rho_o(\mathbf{r}) \quad (2.3.16)$$

and

$$\rho_o(\mathbf{r}) = z \exp[-\beta \phi_{ext}(\mathbf{r})] \quad (2.3.17)$$

where $\Lambda = (h^2/2\pi m k_B T)^{3/2}$ and the fugacity $z = \Lambda^{-1} \exp(\beta \mu)$. Equation (2.3.14) can be rewritten as

$$\beta\mu_{in} = \ln[\Lambda\rho(\mathbf{r})] - c[\rho; \mathbf{r}] \quad (2.3.18)$$

where

$$c[\rho; \mathbf{r}] = \frac{\delta\Psi[\rho]}{\delta\rho(\mathbf{r})} \quad , \quad (2.3.19)$$

is the contribution due to interactions. Equation (2.3.13) can be solved easily and for the equilibrium density we obtain

$$\rho_o(\mathbf{r}) = z \exp[-\beta\phi_{ext}(\mathbf{r}) + c[\rho_o; \mathbf{r}]] \quad . \quad (2.3.20)$$

From this equation, the effect of the interaction can be dealt through the one-body effective potential $c[\rho_o; \mathbf{r}]$. The successive functional derivatives of eqn.(2.3.19) generate a hierarchy of correlation functions,

$$\begin{aligned} c[\rho; \mathbf{r}_1, \mathbf{r}_2] &= \frac{\delta c[\rho; \mathbf{r}]}{\delta\rho(\mathbf{r})} = \frac{\delta^2\Psi[\rho]}{\delta\rho(\mathbf{r}_1)\delta\rho(\mathbf{r}_2)} \\ c^{(3)}[\rho; \mathbf{r}_1, \mathbf{r}_2, \mathbf{r}_3] &= \frac{\delta^2 c[\rho; \mathbf{r}_1]}{\delta\rho(\mathbf{r}_3)\delta\rho(\mathbf{r}_2)} \quad \dots etc. \end{aligned} \quad (2.3. 21)$$

If we define now a local potential $u(\mathbf{r})$ as

$$u(\mathbf{r}) = \mu - \phi_{ext}(\mathbf{r}) \quad , \quad (2.3.22)$$

we can rewrite eqn.(2.3.6) as

$$\Omega_V[\rho] = - \int d\mathbf{r} \rho(\mathbf{r})u(\mathbf{r}) + \mathcal{F}[\rho] \quad . \quad (2.3.23)$$

The functional derivative with respect to $u(\mathbf{r})$ is

$$\frac{\delta\Omega_V[\rho]}{\delta u(\mathbf{r})} = -\rho_o(\mathbf{r}) \quad , \quad (2.3.24)$$

and by successive iterations another series of hierarchic functions can be derived. Explicitly

$$\begin{aligned} G(\mathbf{r}_1, \mathbf{r}_2) &\equiv \beta^{-1} \frac{\delta\rho_o(\mathbf{r}_1)}{\delta u(\mathbf{r}_2)} \\ &= \rho^{(2)}(\mathbf{r}_1, \mathbf{r}_2) + \rho_o\mathbf{r}_1\delta(\mathbf{r}_1 - \mathbf{r}_2) - \rho_o(\mathbf{r}_1)\rho_o(\mathbf{r}_2) \end{aligned} \quad (2.3. 25)$$

where $\rho^{(2)}(\mathbf{r}_1, \mathbf{r}_2)$ is the usual pair distribution function¹³³. Using eqn.(2.3.20) one write the first of equations (2.3.21) in the form

$$\beta \frac{\delta u(\mathbf{r}_1)}{\delta\rho_o(\mathbf{r}_2)} = \frac{\delta(\mathbf{r}_1 - \mathbf{r}_2)}{\rho_o(\mathbf{r}_1)} - c[\rho_o; \mathbf{r}_1, \mathbf{r}_2] \equiv K(\mathbf{r}_1, \mathbf{r}_2) \quad , \quad (2.3.26)$$

where $K(\mathbf{r}_1, \mathbf{r}_2)$ is the inverse of $G(\mathbf{r}_1, \mathbf{r}_2)$

$$\int d\mathbf{r}_1 G(\mathbf{r}_1, \mathbf{r}) K(\mathbf{r}_1, \mathbf{r}') = \delta(\mathbf{r} - \mathbf{r}') \quad . \quad (2.3.27)$$

With these definitions we can see that eqn.(2.3.27) is nothing but the Ornstein-Zernike equation, providing that $c[\rho_o; \mathbf{r}_1, \mathbf{r}_2]$ is the direct correlation function as generalized to the case of a non-uniform system.

Equations (2.3.6) and (2.3.10) allow a variational calculation of the single-particle density and the grand potential of the inhomogeneous system. As a last step one may expand the difference in the grand canonical potential between the inhomogeneous and homogeneous fluid, $\Delta\Omega \equiv \Omega[\rho] - \Omega_l$, in terms of the corresponding difference in density, $\Delta\rho(\mathbf{r}) \equiv \rho(\mathbf{r}) - \rho_l$, leading to practical approximate formulae for sufficiently small differences. In fact, the effective potential $c[\rho; \mathbf{r}]$, as defined in eqn.(2.3.19), can be functionally expanded around its value c_l corresponding to the uniform fluid,

$$\begin{aligned} c(\rho(\mathbf{r}); \mathbf{r}) &= c_l + \int d\mathbf{r}_2 c(|\mathbf{r}_1 - \mathbf{r}_2|) \Delta\rho(\mathbf{r}_2) + \\ &+ \frac{1}{2} \int \int d\mathbf{r}_2 d\mathbf{r}_3 c^{(3)}(\mathbf{r}_2 - \mathbf{r}_1, \mathbf{r}_3 - \mathbf{r}_1) \Delta\rho(\mathbf{r}_2) \Delta\rho(\mathbf{r}_3) + \dots \end{aligned} \quad (2.3. 28)$$

where $c(|\mathbf{r}_1 - \mathbf{r}_2|)$ and $c^{(3)}(\mathbf{r}_2 - \mathbf{r}_1, \mathbf{r}_3 - \mathbf{r}_1)$ are the quantities defined in eqn.(2.3.21) for the homogeneous fluid at density ρ_l . In the same manner one can expand the contribution of the interactions to the free energy Ψ ,

$$\begin{aligned} \Psi &= \Psi_l + \int d\mathbf{r}_1 c_l \Delta\rho(\mathbf{r}_1) + \\ &+ \frac{1}{2} \int \int d\mathbf{r}_1 d\mathbf{r}_2 c(|\mathbf{r}_1 - \mathbf{r}_2|) \Delta\rho(\mathbf{r}_1) \Delta\rho(\mathbf{r}_2) + \dots \end{aligned} \quad (2.3. 29)$$

The difference $\Delta\Omega$ which we are looking for can be determined by writing eqn(2.3.23) as

$$\begin{aligned} \Omega &= \mathcal{F} - \mathcal{F}_{id} + \mathcal{F}_{id} - \int d\mathbf{r} \rho(\mathbf{r}) u(\mathbf{r}) \\ &= -\Psi + \beta^{-1} \int d\mathbf{r} \rho(\mathbf{r}) [c(\mathbf{r}) - 1] \end{aligned} \quad (2.3. 30)$$

and by substituting in it the functional expansions of eqn.(2.3.28) and (2.3.29) we get

$$\begin{aligned} \beta\Delta\Omega &= - \int d\mathbf{r}_1 \Delta\rho(\mathbf{r}_1) + \frac{1}{2} \int \int d\mathbf{r}_1 d\mathbf{r}_2 c(|\mathbf{r}_1 - \mathbf{r}_2|) \Delta\rho(\mathbf{r}_2) [\rho(\mathbf{r}_1) + \rho_l] + \\ &+ \frac{1}{6} \int \int \int d\mathbf{r}_1 d\mathbf{r}_2 d\mathbf{r}_3 c^{(3)}(\mathbf{r}_2 - \mathbf{r}_1, \mathbf{r}_3 - \mathbf{r}_1) [2\rho(\mathbf{r}_1) + \rho_l] \Delta\rho(\mathbf{r}_2) \Delta\rho(\mathbf{r}_3) \end{aligned} \quad (2.3. 31)$$

2.4 Density Functional Theory of Freezing

The modern density functional theory of freezing⁴⁹ amounts to considering the solid as a inhomogeneous system having a periodic one-particle density $\rho_s(\mathbf{r})$. Then, one starts from the liquid phase described by a uniform density ρ_l and inquires for the existence of coexisting crystalline solutions of prescribed lattice symmetry at the equilibrium between the two phases. In this section we simplify the problem by inquiring for freezing of the fluid into a prescribed crystal lattice, leaving aside the question of the relative thermodynamic stability of the different crystalline lattices.

As we have already mentioned in chapter 1 (section 1.4). the solid phase density can be expanded in its Fourier components,

$$\rho_s(\mathbf{r}) = \rho_l(1 + \eta) + \rho_l \sum_{\mathbf{G} \neq 0} \rho_{\mathbf{G}} \exp[i\mathbf{G} \cdot \mathbf{r}] \quad , \quad (2.4.1)$$

where $\eta = (\rho_s - \rho_l)/\rho_l$ is an "order parameter" giving the fractional density change and the Fourier components $\rho_{\mathbf{G}}$ are the "microscopic parameters" of the theory ($\rho_{\mathbf{G}} = 0$) in the liquid phase, $\rho_{\mathbf{G}} \neq 0$ in the solid phase). The translational and rotational crystalline symmetry of $\rho_s(\mathbf{r})$ are guaranteed by eqn.(2.4.1) if (i) \mathbf{G} is a reciprocal lattice vector of the given crystalline lattice and (ii) if all the $\rho_{\mathbf{G}}$ corresponding to a given 'star' of reciprocal lattice vectors are identical. In the limit of a vanishing external potential $\phi_{ext}(\mathbf{r})$, we get for the non-uniform equilibrium density

$$\rho_s(\mathbf{r}) = \Lambda^{-1} e^{\beta\mu_s} e^{c(\mathbf{r})} \quad , \quad (2.4.2)$$

and using the expansion of $c(\mathbf{r})$ in eqn.(2.3.28) truncated at three-body terms, eqn.(2.4.2) becomes

$$\begin{aligned} \rho_s(\mathbf{r}_1) &= \rho_l \exp[\beta\Delta\mu] \exp\left[\int d\mathbf{r}_2 c(|\mathbf{r}_1 - \mathbf{r}_2|)\Delta\rho(\mathbf{r}_2) + \right. \\ &\quad \left. + \frac{1}{2} \int \int d\mathbf{r}_2 d\mathbf{r}_3 c^{(3)}(\mathbf{r}_2 - \mathbf{r}_1, \mathbf{r}_3 - \mathbf{r}_1)\Delta\rho(\mathbf{r}_2)\Delta\rho(\mathbf{r}_3) + \dots\right] \end{aligned} \quad (2.4.3)$$

Here, $\rho_l = \Lambda^{-1} \exp[\beta\mu_l + c_l]$ and $\Delta\mu$ is the difference in the chemical potentials between the two phases (vanishing at coexistence).

Inserting eqn.(2.4.1) in eqn.(2.4.3) we obtain

$$\begin{aligned} \ln \left[\frac{\rho_s(\mathbf{r})}{\rho_l} \right] &= \beta\Delta\mu + c_o\eta + \frac{1}{2} \tilde{c}^{(3)}(0,0)\eta^2 + \frac{1}{2} \sum_{\mathbf{G} \neq 0} \tilde{c}^{(3)}(\mathbf{G}, -\mathbf{G})\rho_{\mathbf{G}}^2 \\ &\quad + \sum_{\mathbf{G} \neq 0} (\tilde{c}(\mathbf{G}) + \tilde{c}^{(3)}(\mathbf{G},0)\eta) \rho_{\mathbf{G}} \exp[i\mathbf{G} \cdot \mathbf{r}] \\ &\quad + \frac{1}{2} \sum_{\mathbf{G}, \mathbf{G}' \neq 0} \tilde{c}^{(3)}(\mathbf{G}, \mathbf{G}') \rho_{\mathbf{G}} \rho_{\mathbf{G}'} \exp[i(\mathbf{G} + \mathbf{G}') \cdot \mathbf{r}] \quad . \end{aligned} \quad (2.4.4)$$

where $\bar{c}(\mathbf{G})$ and $\bar{c}^{(3)}(\mathbf{G}, \mathbf{G}')$ are the Fourier transforms of the Ornstein-Zernike direct correlation function $c(r)$ and of the triplet direct correlation function $c^{(3)}(\mathbf{r}_2 - \mathbf{r}_1, \mathbf{r}_3 - \mathbf{r}_1)$, evaluated at the reciprocal lattice vectors \mathbf{G} :

$$\bar{c}(k) \equiv \rho \int d\mathbf{r} c(r) e^{i\mathbf{k}\cdot\mathbf{r}} \quad (2.4.5)$$

$$\bar{c}^{(3)}(\mathbf{k}, \mathbf{k}') \equiv \rho^2 \int d\mathbf{r}_{12} d\mathbf{r}_{13} c^{(3)}(\mathbf{r}_2 - \mathbf{r}_1, \mathbf{r}_3 - \mathbf{r}_1) e^{[i\mathbf{k}\cdot\mathbf{r}_{12} + \mathbf{k}'\cdot\mathbf{r}_{13}]} . \quad (2.4.6)$$

Taking the exponential of both sides of eqn.(2.4.4) and integrating over \mathbf{r} leads, for the components at $\mathbf{G} = 0$ and at $\mathbf{G} \neq 0$, to the set of equations

$$1 + \eta = \frac{e^{x_0 + \beta\Delta\mu}}{V} \int d\mathbf{r} \exp \left[\sum_{\mathbf{G} \neq 0} x_{\mathbf{G}} e^{i\mathbf{G}\cdot\mathbf{r}} + \sum_{\mathbf{G}, \mathbf{G}' \neq 0} x_{\mathbf{G}, \mathbf{G}'} e^{i(\mathbf{G} + \mathbf{G}')\cdot\mathbf{r}} \right] \quad (2.4.7)$$

$$\rho_{\mathbf{G}} = \frac{e^{x_0 + \beta\Delta\mu}}{V} \int d\mathbf{r} \exp \left[\sum_{\mathbf{G} \neq 0} x_{\mathbf{G}} e^{i\mathbf{G}'\cdot\mathbf{r}} + \sum_{\mathbf{G}', \mathbf{G}'' \neq 0} x_{\mathbf{G}', \mathbf{G}''} e^{i(\mathbf{G}' + \mathbf{G}'')\cdot\mathbf{r}} \right] e^{i\mathbf{G}\cdot\mathbf{r}} \quad (2.4.8)$$

where we have introduced the following:

$$\begin{aligned} x_0 &= c_0 \eta + \frac{1}{2} \bar{c}^{(3)}(0, 0) \eta^2 + \frac{1}{2} \sum_{\mathbf{G}} \bar{c}^{(3)}(\mathbf{G}, -\mathbf{G}) \rho_{\mathbf{G}}^2 \\ x_{\mathbf{G}} &= [\bar{c}(\mathbf{G}) + \bar{c}^{(3)}(\mathbf{G}, 0) \eta] \rho_{\mathbf{G}} \\ x_{\mathbf{G}, \mathbf{G}'} &= \frac{1}{2} \bar{c}^{(3)}(\mathbf{G}, \mathbf{G}') \rho_{\mathbf{G}} \rho_{\mathbf{G}'} \end{aligned} .$$

The set of equations (2.4.7) and (2.4.8) can be solved for a given set of values of $\{\bar{c}(\mathbf{G})\}$ and $\{\bar{c}(\mathbf{G}, \mathbf{G}')\}$. There always is a solution with $\eta = 0$ and $\rho_{\mathbf{G}} = 0$, representing the liquid phase, whereas a solution with $\eta \neq 0$ and $\rho_{\mathbf{G}} \neq 0$ (and periodic $\rho_s(\mathbf{r})$) can occur for an appropriate choice of $\{\bar{c}(\mathbf{G})\}$ and $\{\bar{c}(\mathbf{G}, \mathbf{G}')\}$.

The two phases will be in equilibrium if the difference between the thermodynamic potential Ω_s of the solid and that of the liquid Ω_l is zero. The thermodynamic potential variation in the liquid-solid transformation $\Delta\Omega$ is obtained by substituting in eqn.(2.3.31) the Fourier expansion (2.4.1) with the use of eqn.'s (2.4.5) and (2.4.6):

$$\beta \frac{\Delta\Omega}{N_l} = (c_0 - 1) \eta + \frac{1}{2} (c_0 + \bar{c}^{(3)}(0, 0)) \eta^2 + \frac{1}{3} \bar{c}^{(3)}(0, 0) \eta^3 +$$

$$\begin{aligned}
& + \frac{1}{2} \sum_{\mathbf{G} \neq 0} [\tilde{c}(\mathbf{G}) + (2\eta + 1)\tilde{c}^{(3)}(\mathbf{G}, 0)] \rho_{\mathbf{G}}^2 \\
& + \frac{1}{3} \sum_{\mathbf{G}, \mathbf{G}' \neq 0} \tilde{c}^{(3)}(\mathbf{G}, \mathbf{G}') \rho_{\mathbf{G}} \rho_{\mathbf{G}'} \rho_{\mathbf{G}+\mathbf{G}'} \quad . \quad (2.4.9)
\end{aligned}$$

Equations (2.4.7), (2.4.8) and (2.4.9) are the basic equations that need to be solved in applying the theory.

The quantity $c(\mathbf{G})$ and $\tilde{c}^{(3)}(\mathbf{G}_1, \mathbf{G}_2)$, that appear in the equations for freezing are connected to physical concepts in response theory, by which more insight into the physical interpretation of the freezing process can be gained. It is known that the static response function $\chi(k)$ of a classical fluid to a weak external perturbation coupled with density fluctuations, is related to the static structure factor $S(k)$ through the equation

$$\chi(k) = -\frac{\rho}{k_B T} S(k) \quad . \quad (2.4.10)$$

From the Ornstein-Zernike relation one can also connect the response function to the Fourier transform of the direct correlation function $\tilde{c}(k)$, using the relation

$$S(k) = [1 - \tilde{c}(k)]^{-1} \quad . \quad (2.4.11)$$

It is also known in the $k \rightarrow 0$ limit the relation between the structure factor $S(k)$ and the isothermal compressibility K_T , which denotes the degree of "softness" of the system in response to a uniform compression, i.e.

$$\lim_{k \rightarrow 0} S(k) = \rho K_B T K_T \quad . \quad (2.4.12)$$

In fact eqn.(2.4.10) is a generalization of eqn.(2.4.12) to a deformation with arbitrary wave vector. Thus, $\tilde{c}(\mathbf{G})$ in eqns.(2.4.7) - (2.4.9) measure the "deformability" of the liquid to a weak modulation and can be obtained directly from the structure factor of the liquid near freezing as measured by diffraction or as evaluated from some theoretical model of the interactions between the particles of the liquid. On the other hand, $\tilde{c}^{(3)}(\mathbf{G}_1, \mathbf{G}_2)$ makes allowance for non-linear response to modulation, at the lowest level of non-linearity, with specific relation to (i) the density dependence of the compressibility (when $\mathbf{G}_1 = \mathbf{G}_2 = 0$), (ii) the density dependence of the structure factor (when $\mathbf{G}_2 = 0$ with $\mathbf{G}_1 \neq 0$), and (iii) genuine microscopic coupling between order parameters (when \mathbf{G}_1 and \mathbf{G}_2 are both different from zero).

Let us return now to the equations of freezing (2.4.7), (2.4.8) and (2.4.9). Equation (2.4.9) is composed of the sum of terms depending on η and terms depending on $\rho_{\mathbf{G}}$. The condition $\Delta\Omega = 0$, which corresponds to the equilibrium of the two phases, can be satisfied if the change in the free energy

due to the change in the average density is compensated by the change in the free energy due to the modulation in density. More particularly, free energy is normally gained in the first (for $\eta > 0$) while it is expended in the second case. Hence the transition will occur by spontaneous modulation of the system at wave numbers such as to reduce the free energy expense, which are those corresponding to the peaks in the structure factor.

2.4.1 Entropy and Volume Changes Across the Phase Transition

We turn next to discuss the different routes that can be followed for calculating the entropy and volume changes across the phase transition, within the framework of the density functional theory. As already discussed, the expansion of the appropriate thermodynamic potential of the ordered phase around that of the homogeneous liquid requires (i) a functional expansion in which direct correlation functions of any order appear, and (ii) a Fourier representation of the one-body density $\rho(\mathbf{r})$. In practical applications^{50,54,80}, one has to truncate the expansion in both (i) and (ii) (see chapter 1, section 1.5.1 and 1.5.4). D'Aguanno et al¹³⁴ have pointed out that thermodynamic inconsistency should be expected to arise from the above approximations.

Upon freezing with finite volume change, one can calculate the entropy change per particle (Δs) within the usual approach^{49,54,135} of relating Δs to the difference in the grandcanonical potential between the two phases. In fact, D'Aguanno et al¹³⁴ presented the correct expression for the entropy change Δs across the phase transition, in which the effect of the finite volume change at freezing is included, and also proposed a new method for calculating Δs which, in particular, avoids an unphysical dependence of the entropy change on the mass of the particles yielded by approximate calculations carried out within previous approaches. Following Haymet and Oxtoby⁵⁰ and D'Aguanno et al¹³⁴, and including only second order terms in the difference $\rho(\mathbf{r}) - \rho_l$ (eqn.2.4.1), the equilibrium condition for the microscopic order parameters (eqn.2.4.8) can be written in a more convenient way as

$$\rho_{\mathbf{G}} = (1 + \eta) \frac{\int d\mathbf{r} e^{i\mathbf{G}\cdot\mathbf{r}} \exp[c_0\eta + \sum_{\mathbf{G}' \neq 0} \bar{c}(\mathbf{G}') \rho_{\mathbf{G}'} e^{i\mathbf{G}'\cdot\mathbf{r}}]}{\int d\mathbf{r} \exp[c_0\eta + \sum_{\mathbf{G}' \neq 0} \bar{c}(\mathbf{G}') \rho_{\mathbf{G}'} e^{i\mathbf{G}'\cdot\mathbf{r}}]} \quad (2.4.13)$$

One also obtains expressions for the difference in chemical potential, $\Delta\mu = \mu_s - \mu_l$,

$$\Delta\mu = -k_B T \ln \left\{ \frac{1}{(1 + \eta)V} \int d\mathbf{r} \exp[c_0\eta + \sum_{\mathbf{G}' \neq 0} \bar{c}(\mathbf{G}') \rho_{\mathbf{G}'} e^{i\mathbf{G}'\cdot\mathbf{r}}] \right\} \quad (2.4.14)$$

and an equation for the difference in pressure $\Delta P = P_s - P_l$,

$$\Delta P = \rho_l k_B T \left[-\eta + c_o \eta + \frac{1}{2} c_o \eta^2 + \frac{1}{2} \sum_{\mathbf{G} \neq 0} \bar{c}(\mathbf{G}) |\rho_{\mathbf{G}}|^2 \right] \quad (2.4.15)$$

In these equations. ρ_l is the density of the fluid phase, $\rho_{\mathbf{G}}$ are the microscopic order parameters associated with the reciprocal lattice vectors \mathbf{G} , and $\eta = (\rho_s - \rho_l)/\rho_l = \Delta v/v_s$ gives the percentual volume difference between the two phases. The subscripts s and l are to denote macroscopic properties of the solid and fluid phase respectively. The $\bar{c}(\mathbf{G})$ are the Fourier components of the Ornstein-Zernike correlation function $c(r)$ of the fluid at the RLV stars of the solid (eqn.2.4.5), and c_o is the regular part of the Fourier transform of $c(r)$ at long wavelengths, which in the OCP on a deformable background will embody thermodynamic properties to be assigned to the background. In particular, this quantity will be related to the isothermal compressibility K_T of the full system of ions plus background, according to the Ornstein-Zernike relation.

$$c_o = 1 - \frac{1}{S(0)} = 1 - \frac{1}{\rho_l k_B T K_T} \quad (2.4.16)$$

The set of order parameters $\rho_{\mathbf{G}}$ and η at coexistence, must satisfy the equilibrium equations (2.4.13) under the condition that the pressure and chemical potential difference should vanish, $\Delta P = \Delta \mu = 0$. This fixes the freezing line (ρ_f, T_f) , once the liquid structure is known as a function of ρ and T , and gives the fractional volume change η and the Fourier components $\rho_{\mathbf{G}}$ of the density ρ in the coexistent solid.

The change on freezing of a thermodynamic property such as the entropy per particle s can be calculated from the slopes of ΔP or of $\Delta \mu$ near the freezing point. These can be obtained, in turn, by solving eqn.(2.4.13) under the only condition $\Delta \mu = 0$ (or $\Delta P = 0$). In terms of ΔP the entropy per particle can be written as

$$\begin{aligned} \Delta s &= s_s - s_l = -\frac{1}{1 + \eta} \left[k_B T \frac{\partial \Delta P}{\partial T} \Big|_{\mu} + \eta s_l \right]_{\rho_f, T_f} \\ &= -\frac{1}{1 + \eta} \left[k_B T \frac{\partial \Delta P}{\partial \rho} \Big|_T \frac{\partial \rho}{\partial T} \Big|_{\mu} + k_B T \frac{\partial \Delta P}{\partial T} \Big|_{\rho} + \eta s_l \right]_{\rho_f, T_f} \end{aligned} \quad (2.4.17)$$

were the expression in the second row is obtained from the fact that ΔP (eqn.2.4.15) is a function of temperature T and of the density ρ of the liquid. The contribution $-\eta s_l/(1 + \eta)$ to the entropy change originates from the fact that, in the grandcanonical ensemble, the number of particles in the volume V for the crystalline phase, N_s , is different from that for the liquid phase, N_l ,

with $(N_s - N_l)/N_l = \eta$. Such a term, which has been neglected in previous formulas^{49,54,135} for Δs , has the unpleasant feature that it contains the mass of the particles. This appears in the ideal part of s_l . However, there is another term in Δs which is proportional to ρ_l . By utilizing thermodynamic identities, in fact, eqn.(2.4.17) can be modified to read

$$\Delta s = \left[(1 - \alpha)\rho\Delta v s_l + \alpha \left. \frac{\partial S_l}{\partial V} \right|_T \Delta v - \frac{k_B T}{1 + \eta} \left. \frac{\partial P}{\partial T} \right|_{\rho} \right]_{\rho_f, T_f} \quad (2.4.18)$$

with $\Delta v = v_s - v_l$, the volume per particle, and

$$\alpha = \left[-\frac{k_B T}{\eta} \left. \frac{\partial \Delta P}{\partial \rho} \right|_T \rho \left. \frac{\partial \rho}{\partial P} \right|_T \right]_{\rho_f, T_f} \quad (2.4.19)$$

The entropy per particle is now decomposed, in eqn.(2.4.18), into three terms. The first term contains all the dependence on the mass m of the particles. Since Δs cannot depend on m , an exact calculation must yield $\alpha = 1$. [in the case where the first term vanishes due to $\alpha = 1$, one recover the partitioning of the entropy change into a volume term plus a remainder as proposed by Tallon¹³⁶, where the term $(\partial S_l/\partial V)_T \Delta v$ can be formally identified as the change in entropy due to the isothermal compression of the liquid to the density of the solid at constant $(\partial S_l/\partial V)_T \Delta v$]. It has been concluded by D'Aguanno et al that eqn.(2.4.17) and (2.4.18) do not provide a convenient way of evaluating the entropy change. In the case of freezing of hard spheres by Haymet⁵⁴, the $\Delta P(\rho)$ around ρ_f were given and the value of α is easily evaluated to be 2.3.

Another route to evaluate Δs was proposed by D'Aguanno et al¹³⁴ by exploiting the dependence of $\Delta\mu$ on ρ and T , where one gets:

$$\begin{aligned} \Delta s &= - \left[\left. \frac{\partial \Delta \mu}{\partial T} \right|_P \right]_{\rho_f, T_f} \\ &= - \left[\left. \frac{\partial \Delta \mu}{\partial \rho} \right|_T + \left. \frac{\partial \rho}{\partial T} \right|_P + \left. \frac{\partial \Delta \mu}{\partial T} \right|_{\rho} \right]_{\rho_f, T_f} \end{aligned} \quad (2.4.20)$$

This formula does not contain any dependence on the mass of the particles. Moreover, from the slope of $\Delta\mu$ around the freezing point it is to obtain an alternative thermodynamic equation for the fractional volume change

$$\begin{aligned} \rho_f \Delta v = -\frac{\eta}{1 + \eta} &= \rho_f \left[\left. \frac{\partial \Delta \mu}{\partial P} \right|_T \right]_{\rho_f, T_f} \\ &= \rho_f \left[\left. \frac{\partial \Delta \mu}{\partial \rho} \right|_T + \left. \frac{\partial \rho}{\partial P} \right|_T \right]_{\rho_f, T_f} \end{aligned} \quad (2.4.21)$$

hence the comparison between η from eqn.(2.4.21) and η from the coexistence conditions (eqn.2.4.13 and 2.4.15) with ΔP and $\Delta\mu$ set to zero) provides a simple check on the internal consistency of an approximate calculation. The entropy change and the fractional volume change were calculated from eqn's.(2.4.20) and (2.4.21), respectively, by D'Aguanno et al ¹³⁴ in the case of the freezing of hard spheres. They found $\Delta s = -1.9k_B$ and $\eta = 0.06$. These values should be compared with the computer simulation results, $\Delta s = -1.2k_B$ and $\eta = 0.10$.

The above mentioned alternative routes for calculating the entropy change and the volume change across the phase transition are going to be used in the following sections (2.6 and 2.7).

2.4.2 Gaussian Width and Lindemann's Ratio

Finally, we discuss the relationship between the microscopic order parameters $\rho_{\mathbf{G}}$ and the Debye-Waller factors of the crystal at melting. As we have already discussed in chapter 1 (section 1.5.4), the density profile $\rho_s(\mathbf{r})$, of the solid phase in real space can be approximated as a superposition of Gaussian centered at the various sites and with a width that is to be evaluated variationally. That is

$$\rho_s(\mathbf{r}) = \rho \frac{1}{N_1} \sum_j \left(\frac{\alpha}{\pi}\right)^{3/2} \exp(-\alpha(\mathbf{r} - \mathbf{R}_j)^2) \quad , \quad (2.4.22)$$

where ρ is the average density of the solid, N_1 the number of particles per unit cell while j labels the lattice sites (located at $\{\mathbf{R}_j\}$), and the periodicity is taken care of by the sum over the sites.

The connection between the Gaussian representation in eqn.(2.4.22) and the density wave expansion eqn.(2.4.1) can easily be obtained from the following Poisson sum formula ¹³⁷

$$\begin{aligned} \rho_s(\mathbf{r})/\rho &= \frac{1}{N_1} \sum_j \left(\frac{\alpha}{\pi}\right)^{3/2} \exp(-\alpha(\mathbf{r} - \mathbf{R}_j)^2) \\ &= \sum_{\mathbf{G}} \exp(-|\mathbf{G}|^2/4\alpha) \exp[i\mathbf{G}\cdot\mathbf{r}] \quad . \end{aligned} \quad (2.4. 23)$$

Comparing eqn.(2.4.23) and eqn.(2.4.1) we can see that in the Gaussian representation, the microscopic order parameters $\rho_{\mathbf{G}}$ are

$$\rho_{\mathbf{G}} = (1 + \eta) \exp(-|\mathbf{G}|^2/4\alpha) \quad (2.4.24)$$

where we can relates these microscopic order parameters with the Lindemann ratio $L = \sqrt{\langle (\Delta u)^2 \rangle} / d^2$, since

$$\langle (\Delta u)^2 \rangle = \langle (\mathbf{r} - \mathbf{R}_j)^2 \rangle = \frac{3}{2\alpha} \quad (2.4.25)$$

then

$$\rho_{\mathbf{G}} = (1 + \eta) \exp\left[-\frac{1}{6}L^2G^2d^2\right] \quad , \quad (2.4.26)$$

where d is the first neighbour distance in the specific crystal structure under consideration.

In fact, the series (2.4.22) is term by term positive and rapidly converging as we have seen in chapter 1 (section 1.5.4 and fig.1.9). In the following sections we are going to see how the microscopic order parameters $\rho_{\mathbf{G}}$ conform rather closely to a Gaussian behaviour and yield a Lindemann ratio in reasonable agreement with the empirical value for melting for the different cases that we are going to consider. This will be done by full evaluation of the order parameters $\rho_{\mathbf{G}}$ from the equilibrium conditions of the theory and by representing them in the form

$$\rho_{\mathbf{G}} = (1 + \eta) \exp\left[-\frac{1}{6}L_G^2G^2d^2\right] \quad (2.4.27)$$

where L_G is a “star dependent Lindemann ratio”. Clearly, the accuracy of a Gaussian representation of the density profile can be tested by examining the dependence of L_G on \mathbf{G} .

2.5 Freezing of One-Component Plasma on a Rigid Background (OCP-RB)

Crystallization of the one-component plasma on a rigid background (OCP-RB) has been studied by computer simulation^{75,23} and within the density functional theory^{79,80,83,84}, as discussed in chapter 1 (section 1.6).

In this section we are going to reevaluate the theory of freezing of the OCP-RB, in view of the recent progress in the determination of its thermodynamic functions by computer simulation⁷⁶ and as a preliminary step to our evaluation of the freezing of alkali metals¹⁴¹. We shall discuss the difficulties of the density wave theory of freezing for the OCP, related to the order parameter at the (200) star of RLV and also consider freezing of the OCP into the bcc and the fcc structure. In addition, the entropy change across the phase transition will be evaluated.

The earlier Monte Carlo data^{24,25} for the internal energy per particle in the fluid OCP have been fitted, in terms of the coupling strength Γ , to the form

$$U/Nk_B T = a\Gamma + b\Gamma^{1/4} + c + d\Gamma^{-1/4} \quad (2.5.1)$$

where a, b, c and d are constants and the exponent $1/4$ was first proposed by De Witt⁷⁵. The available Monte Carlo runs at that time did not permit to obtain the exponent to a good degree of accuracy. Recently De Witt et al⁷⁶ have generated long runs for a larger number of particles and proposed for the internal energy per particle the expression

$$U/Nk_B T = -0.8992\Gamma + 0.596\Gamma^{0.3253} - 0.268 \quad (2.5.2)$$

These authors have also calculated freezing into the bcc structure (which occurs at $\Gamma = 178 \pm 1$ and into the fcc structure (at $\Gamma = 192$). The expression for U enters the evaluation of the structure factor $S(qa; \Gamma)$, that we carry in the generalized mean spherical approximation (GMSA)¹⁰⁹ and use as input for the evaluation of freezing into both structures.

At this stage we would like to summarily present the main equations that we use in the case of freezing of the OCP-RG. In fact the set of equations derived by previous authors⁸⁰, and in this case, however, the coexistence condition is given by the vanishing of the Helmholtz free energy difference, that is

$$\Delta F/N = \Delta\mu - \Delta P/\rho_l = 0 \quad (2.5.3)$$

whereas eqn.(2.4.14) (with $\eta = 0$) allows an estimate for the interfacial dipole layer between the two phases.

Recalling our discussion in chapter 1 (section 1.6), the Fourier representation of the charge density in the solid in terms of the order parameters $\rho_{\mathbf{G}}$ as

$$\rho(\mathbf{r}) - \rho_l = \rho_l \sum_{\mathbf{G} \neq 0} \rho_{\mathbf{G}} \exp[i\mathbf{G} \cdot \mathbf{r}] \quad , \quad (2.5.4)$$

the microscopic conditions for equilibrium and phase coexistence in the OCP (eqn's. (1.6.1) and 1.6.2) of chapter 1) in the Fourier representation and up to second order terms, are

$$\begin{aligned} \beta(F_s - F_l)/N &= -\ln \psi_o + \frac{1}{2} \sum_{\mathbf{G}_n \neq 0} \tilde{c}(\mathbf{G}_n) |\rho_{\mathbf{G}_n}|^2 + \dots \\ &= 0 \end{aligned} \quad (2.5.5)$$

and

$$\rho_{\mathbf{G}_n} = \psi_o^{-1} \int d\mathbf{r} e^{i\mathbf{G} \cdot \mathbf{r}} \exp\left[\sum_{\mathbf{G}_m \neq 0} \tilde{c}(\mathbf{G}_m) \rho_{\mathbf{G}_m} e^{i\mathbf{G}_m \cdot \mathbf{r}} + \dots \right] \quad (2.5.6)$$

where $\tilde{c}(\mathbf{G})_m$ are the Fourier transform of the two-body direct correlation function. The quantity ψ_o is related to the chemical potential and can be

determined in two ways: (i) by using eqn.(1.6.3) (chapter 1) in eliminating $\beta(\mu_s - \mu_l)$, which yields

$$\psi_o = \int d\mathbf{r} \exp\left[\sum_{\mathbf{G}_m \neq 0} \tilde{c}(\mathbf{G}_m) \rho_{\mathbf{G}_m} e^{i\mathbf{G}_m \cdot \mathbf{r}} + \dots \right] \quad (2.5.7)$$

where one recovers the equations used by Bagchi et al ⁷⁸ and Haymet ⁷⁹; or (ii) by using computer simulation data for $\beta(\mu_s - \mu_l)$ and the expression

$$\psi_o = \exp\left[-\beta(\mu_s - \mu_l) - \frac{1}{2} \sum_{\mathbf{G}_n \neq 0} \tilde{c}^{(3)}(\mathbf{G}_n, 0) |\rho_{\mathbf{G}_n}|^2 \right] \quad (2.5.8)$$

where we have included the next higher-order correction $\tilde{c}^{(3)}(\mathbf{G}_n, 0)$, which can be calculated from

$$\begin{aligned} \tilde{c}^{(3)}(\mathbf{G}_n, 0) &= -\tilde{c}(\mathbf{G}_n) + \rho \left(\frac{\partial \tilde{c}(\mathbf{G}_n)}{\partial \rho} \right)_T \\ &= -\tilde{c}(\mathbf{G}_n) + \frac{1}{3} \Gamma \left(\frac{\partial \tilde{c}(\mathbf{G}_n)}{\partial \Gamma} \right) \end{aligned} \quad (2.5.9)$$

In either of the routes that we have mentioned, we can also evaluate the difference in the chemical potential across the transition, (through the sum rule (1.6.3) of chapter 1), i.e.

$$\beta(\mu_s - \mu_l) = -\frac{1}{2} \sum_{\mathbf{G}_n \neq 0} \tilde{c}^{(3)}(\mathbf{G}_n, 0) |\rho_{\mathbf{G}_n}|^2 - \ln\left(\int d\mathbf{r} \exp\left[\sum_{\mathbf{G}_m \neq 0} \tilde{c}(\mathbf{G}_m) \rho_{\mathbf{G}_m} e^{i\mathbf{G}_m \cdot \mathbf{r}} \right] \right) \quad (2.5.10)$$

as a test of the results of the evaluation of the order parameters against the simulation data.

the search for coexistence point is carried out by solving the set of equations (2.5.6) for the order parameters $\rho_{\mathbf{G}_n}$ at a given value of the coupling strength and by varying the coupling strength Γ until eqn.(2.5.5) is satisfied. Satisfactory convergence in the determination of Γ_c is achieved by including nineteen stars of reciprocal lattice vectors. Convergence can be accelerated by including in successive steps the stars of RLV which lie between alternate nodes of the direct correlation function $\tilde{c}_l(k)$. The equations were solved by a refined version of the Newton-Raphson method.

We are going to discuss separately the results that we have obtained by excluding the equilibrium equation for the order parameter $\rho_{\mathbf{G}_2}$ in the "linearized" theory (\mathbf{G}_2 denotes the (200) star) and the calculations that we have carried out by including this order parameter also.

2.5.1 Results with Exclusion of Equilibrium Equation for ρ_{G_2}

The values of $\bar{c}(G)_2$ in figure (1.8) (chapter 1) is strongly negative, namely the liquid structure factor $S(k)$ has a deep minimum in this region of wave number (i.e. near the (200) star). Following first the procedure suggested by Rovere and Tosi ⁸⁰, the order parameter ρ_{G_2} was excluded from our calculation. As already noted, the values of the direct correlation function in the fluid phase were calculated using the generalized mean spherical (GMSA) approximation combined with the recent simulation result for internal energy of the fluid OCP by De Witt et al ⁷⁶. However, we found only very small changes from the earlier calculation of $\bar{c}(k)$ by Rovere and Tosi ⁸⁰, and again the results are in very close agreement with the simulation data at the representative value of $\Gamma = 160$ (see figure 2.3).

The values for the coupling parameters Γ_c at the solid-liquid transition point, for freezing into the bcc structure, is $\Gamma_c = 156.75$, which is approximately the same as in the previous calculation of Rovere and Tosi ⁸⁰. This theoretical value for Γ_c is not too far from the value $\Gamma_c = 178$ obtained by De Witt ⁷⁶ from simulation data for the free energies of the two phases. Table (2.5) summarise our results when the order parameter ρ_{G_2} is set to zero and simultaneously excluding the equilibrium equation for this order parameter from the set (2.5.6).

The value of $\beta(\mu_s - \mu_l)|_{\Gamma=\Gamma_c}$ from the sum rule (2.5.10) is -0.70 , which is to be compared with the value -0.26 from the available data on the equation of state of the two phases.

The entropy of freezing $\Delta s = (s_s - s_l)|_{\Gamma=\Gamma_c}$ can be calculated from its definition at coexistence,

$$\Delta s = -(\partial F_s / \partial T)_v + (\partial F_l / \partial T)_v \quad . \quad (2.5.11)$$

The specific functional dependence of the free energy of the plasma on T and ρ allows one to rewrite eqn.(2.6.11) as

$$\Delta s = k_B T \frac{d}{d\Gamma} [\beta(F_s - F_l)/N]_{\Gamma=\Gamma_c} \quad . \quad (2.5.12)$$

with $(F_s - F_l)/N$ given by equation (2.5.5) as a function of Γ . The result is $\Delta s/k_B \simeq -1.0$ in our calculation, to be compared with the value $\Delta s/k_B \simeq -0.78$ from the data of De Witt et al ⁷⁶.

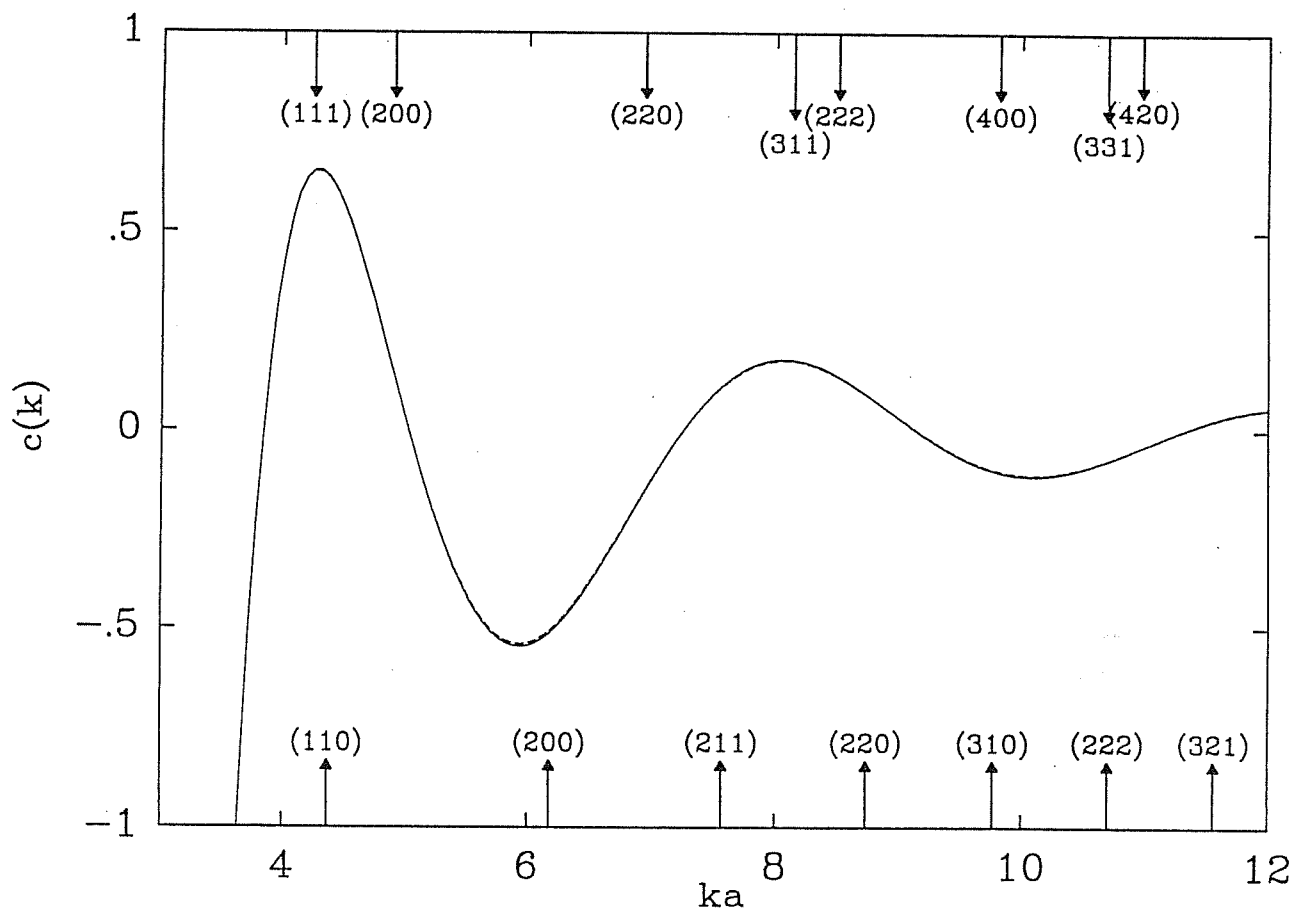


Figure 2.3: The Ornstein-Zernike direct correlation function $\bar{c}(k)$ of the OCP at $\Gamma = 160$ as a function of reduced wave number ka . Full curve: present GMSA results, using the internal energy of the OCP from De Witt et al [76]; dashed curve: GMSA results from earlier internal energy data by Slattery et al [24]. The arrows give the locations of the stars of RLV for the bcc lattice (bottom) and for the fcc lattice (top).

$Star\mathbf{G}$	$\bar{c}(\mathbf{G})$	$\rho_{\mathbf{G}}$	L
110	0.6330	0.7493	0.171
200	- 0.5046		∞
211	0.1117	0.4722	0.159
220	0.0911	0.3868	0.155
310	- 0.0975	0.2995	0.156
222	- 0.0731	0.2600	0.151
321	0.0287	0.2140	0.149
400	0.0591	0.1590	0.153
411	0.0179	0.1374	0.150
330	0.0179	0.1525	0.145
420	- 0.0289	0.1191	0.147
332	- 0.0394	0.1050	0.144
422	- 0.0171	0.0870	0.144
510	0.0119	0.0648	0.146
431	0.0119	0.0756	0.142
521	0.0206	0.0497	0.142
440	0.0037	0.0486	0.138
530	- 0.0123	0.0383	0.139
433	- 0.0123	0.0379	0.140

Table 2.5: *The bcc freezing parameter of the OCP-RB (in the case with $\rho_{\mathbf{G}_2} = 0$). In the first column the various stars that were used, the second column the values of the $\bar{c}(\mathbf{G})$ at the different stars, the third and fourth column are the various values of the order parameters $\rho_{\mathbf{G}}$ and the Lindemann ratio respectively. For the coupling strength $\Gamma = 156.75$.*

2.5.2 Calculations with Inclusion of $\rho_{\mathbf{G}_2}$

No solution of the full set of equilibrium equations (2.5.5) for the order parameters was found in the range of values of Γ where the phase transition is expected when the equilibrium equation for $\rho_{\mathbf{G}_2}$ is also included and the input structure data are calculated by the GMSA.

The difficulty with the order parameter $\rho_{\mathbf{G}_2}$ can be looked at from two alternative points of view: (i) since the liquid structure factor shows that the fluid is very rigid against a modulation by a density wave with wave vector \mathbf{G}_2 , then the order parameter $\rho_{\mathbf{G}_2}$ can only be small and likely arises from a cooperative process which is lost on decoupling the various order parameters through the truncated cluster expansion; (ii) the order parameter $\rho_{\mathbf{G}_2}$ may be driven by the other order parameters (in particular with those associated with the (110) star⁸⁰), that the three body function $\bar{c}^{(3)}(\mathbf{G}_1, \mathbf{G}_2)$ may have an important role, in some sense equivalent to raising the value of $\bar{c}(\mathbf{G}_2)$ at the star (200) to an effectively higher value.

We have examined both view points. First we start by increasing the order parameter $\rho_{\mathbf{G}_2}$ progressively in the equilibrium equations, as if this order parameter were a free parameter, and we find that the predicted value of Γ_c increases, approaching $\Gamma = 178$ for $\rho_{\mathbf{G}_2} = 0.038$. Table (2.6) shows the values of the other order parameters at $\Gamma_c = 178$, which are slightly higher than in table (2.5) (i.e. when $\rho_{\mathbf{G}_2} = 0$). The corresponding values of the thermodynamic parameter of the phase transition are $\beta(\mu_s - \mu_l)|_{\Gamma=178} \simeq -0.72$ and $\Delta s/k_B = -0.94$.

Alternatively, we have considered $\bar{c}(\mathbf{G}_2)$ as a free parameter and tried to solve the set of equilibrium equations for the order parameters $\rho_{\mathbf{G}}$ including also the equation for $\rho_{\mathbf{G}_2}$, fixing $\Gamma_c = 178$ to the computer simulation results. The effective value of $\bar{c}(\mathbf{G}_2)$ is -0.134 , which is roughly 24% of the simulation data. In table (2.7) we tabulate our results for the order parameters $\rho_{\mathbf{G}}$, where we can see that the value of $\rho_{\mathbf{G}_2}$ is quite reasonable with respect to the rest of the order parameters. The values of $\beta(\mu_s - \mu_l)|_{\Gamma_c=178}$ is -0.5 whereas the change in entropy is $\Delta s/k_B = -0.94$.

The values of the order parameters $\rho_{\mathbf{G}}$ for the different cases that we have considered (section 2.5.1 and 2.5.2) are tabulated in tables (2.5-2.7). These order parameters of the phase transition, excepting the (200) one, conform rather closely to a Gaussian behaviour and yield Lindemann ratios (tabulated in last column) in reasonable agreement with empirical values for melting of bcc crystal. In the case when we were looking for an effective $\bar{c}(\mathbf{G})$ at the (200) star (table 2.7), the Lindemann ratio for this star falls in the general pattern set by the others, which strengthens the viewpoint of the presence of microscopic coupling between the order parameters. All the parameters of freezing into the bcc lattice for the OCP-RB and for the OCP on a deformable background (that we are going to discuss in the following

section 2.6) are collected in table (2.15).

$Star\mathbf{G}$	$\bar{c}(\mathbf{G})$	$\rho_{\mathbf{G}}$	L
110	0.6567	0.7694	0.163
200	- 0.5554	0.0038	0.531
211	0.1353	0.5016	0.153
220	0.0839	0.4172	0.149
310	- 0.1169	0.3261	0.151
222	- 0.0706	0.2895	0.145
321	0.0423	0.2401	0.144
400	0.0630	0.1776	0.148
411	0.0094	0.1565	0.144
330	0.0094	0.1765	0.140
420	- 0.0389	0.1380	0.141
332	- 0.0416	0.1255	0.138
422	- 0.0111	0.1044	0.138
510	0.0199	0.0758	0.142
431	0.0199	0.0921	0.136
521	0.0182	0.0602	0.138
440	- 0.0026	0.0613	0.133
530	- 0.0182	0.0480	0.134
433	- 0.0182	0.0494	0.134

Table 2.6: *The bcc freezing parameter of the OCP-RB in the case with $\rho_{\mathbf{G}_2}$ were fixed at 0.0038 to reproduce the computer simulation [76] with coupling parameter $\Gamma = 178$.*

$Star\mathbf{G}$	$\bar{c}(\mathbf{G})$	$\rho_{\mathbf{G}}$	L
110	0.6567	0.723	0.181
200	- 0.1340	0.532	0.179
211	0.1353	0.440	0.166
220	0.0839	0.360	0.161
310	- 0.1169	0.264	0.164
222	- 0.0706	0.237	0.156
321	0.0423	0.193	0.154
400	0.0630	0.130	0.161
411	0.0094	0.115	0.156
330	0.0094	0.140	0.149
420	- 0.0389	0.101	0.152
332	- 0.0416	0.094	0.148
422	- 0.0111	0.076	0.147
510	0.0199	0.050	0.153
431	0.0199	0.067	0.145
521	0.0182	0.040	0.147
440	- 0.0026	0.044	0.141
530	- 0.0182	0.032	0.143
433	- 0.0182	0.034	0.142

Table 2.7: *The bcc freezing parameter of the OCP-RB in the case where we ask what is the effective $\bar{c}(\mathbf{G})$ at the (200) star, so that one reproduce the computer simulation [76] with coupling parameter $\Gamma = 178$.*

2.5.3 Freezing of OCP-RB Into the F.c.c. Structure

We turn to discuss the relative stability of the fcc structure for the OCP-RB. The main input for our calculation in this section is again the direct correlation function $\bar{c}(k)$ of the OCP as a function of the plasma parameter Γ . Reference to the locations of the stars of RLV for the bcc and fcc structures relative to the peaks and valleys of $\bar{c}(k)$ in fig.(2.3) indicates that they may be competitive, insofar as in both the first RLV star is close to the maximum in the main peak of $\bar{c}(k)$ and a number of order parameters lie in the region of the subsequent deep minimum of this function. The relative stability of the two structures should thus be primarily determined by a balance between the higher number of order parameters lying in this region for the fcc structure and the strongly negative value attained by $\bar{c}(\mathbf{G}_2)$ for freezing into bcc structure.

In fact, in the microscopic calculations that we have carried out for freezing into the fcc lattice, we have solved the set of equations (2.5.6) for the order parameters $\rho_{\mathbf{G}}$, monitoring at the same time the free energy difference

in eqn.(2.5.5). The method of solution is the same as the one we followed in the case of freezing of OCP-RB into the bcc structure. We found no self-consistent solution of eqns.(2.5.6) and (2.5.5) when we included all the successive stars up to (551) star, but excluding the third star (220), which has a stronger negative value of $\bar{c}(k)$, we obtain satisfactory convergence in the results. We find in this case $\Gamma \simeq 300$ for the phase transition, and our results are tabulated in table (2.8). The order parameters $\rho_{\mathbf{G}}$, excepting the (220) one, conform rather closely to a Gaussian behaviour and yield a Lindemann ratio in reasonable agreement with the empirical value for melting of f.c.c. crystals (with a Lindemann ratio $\simeq 0.12 \div 0.065$ ^{4,5}. Our results are broadly consistent with available evidence from computer simulation from De Witt ⁷⁶ ($\Gamma_c = 190$) in suggesting that freezing into f.c.c. structure is unfavoured and confirm an earlier report by Barrat and Hansen ²⁷ ($\Gamma_c \geq 210$ and excluding the (220) star).

<i>Star</i> \mathbf{G}	$\bar{c}(\mathbf{G})$	$\rho_{\mathbf{G}}$	L
111	0.7475	0.888	0.089
200	- 0.0160	0.856	0.089
220	- 0.1244		∞
311	0.2380	0.688	0.083
222	0.1222	0.669	0.082
400	- 0.1973	0.588	0.082
331	- 0.0421	0.541	0.081
420	0.0205	0.530	0.081
422	0.0939	0.470	0.080
511	0.0045	0.430	0.080
333	0.0045	0.434	0.079
440	- 0.0724	0.373	0.078
531	- 0.0290	0.344	0.079
600	- 0.0094	0.333	0.078
442	- 0.0094	0.337	0.078
533	0.0410	0.289	0.078
622	0.0324	0.269	0.077
444	- 0.0126	0.247	0.077
711	- 0.0336	0.222	0.077
551	- 0.0336	0.223	0.077

Table 2.8: *The freezing parameter of the OCP-RB into fcc structure for the coupling parameter $\Gamma \simeq 300$.*

2.6 Freezing of OCP on a Deformable Background (OCP-DB)

In this section we present our calculations for freezing of an OCP on a deformable background (OCP-DB) into the bcc lattice, on allowing for long-wavelength deformability of the background.

The first issue here is the value to be chosen for the quantity c_o (the regular part of the Fourier transform of $c(r)$ at long-wavelength) expressing the deformability, or equivalently for the long-wavelength structure factor $S(0) = [1 - c_o]^{-1}$. In fact we have chosen the values of $S(0)$ in the range $0.021 \div 0.026$ as appropriate for liquid alkali metal near freezing from data in the literature (table (2.9)). We have carried out the calculations for three different values of $S(0)$ ($S(0) = 0.02, 0.023$ and 0.0256) and our results are tabulated in tables (2.10-2.12). The common input to these calculations is, in addition to $S(0)$, the direct correlation function $\bar{c}(k)$ of the OCP as a function of plasma parameter Γ evaluated by the GMSA ¹⁰⁸ using as an input the new expression for the internal energy of the OCP as a function of Γ given by De Witt et al ⁷⁶.

<i>Element</i>	$S(0)$ ¹¹⁵	$S(0)$ ⁴	$S(0)$ ¹¹⁷
<i>Li</i>	0.0266	0.031	0.0310
<i>Na</i>	0.0230	0.024	0.0256
<i>K</i>	0.0224	0.023	0.0241
<i>Rb</i>	0.0213	0.022	0.0245
<i>Cs</i>	0.0240	0.028	0.0256

Table 2.9: *The Long length structure factors $S(0)$ for the liquid alkali metals near freezing as available in the literature.*

Freezing of the OCP-DB is accompanied by a volume change, and we assume exact cancellation of the divergent Coulombic terms at long wavelengths through perfect screening of the ions by the charges in the background. We have solved the set of equations (2.4.13) for the microscopic order parameters ρ_G as functions of Γ . The conditions for phase coexistence are

$$\Delta\mu = 0 \tag{2.6.1}$$

by which eqn.(2.4.14) will be the equation for estimating the volume change η , and

$$\Delta P = 0 \quad (2.6.2)$$

that is eqn.(2.4.15). The method of solution follows the same manner as in the case of the OCP-RB. we again could not find self-consistent solutions of eqn.(2.4.13) and (2.4.15) when the order parameter $\rho_{\mathbf{G}}$ at the (200) star is included among the others to be determined from the appropriate eqn.(2.4.13), but excluding the latter we obtained satisfactory convergence in the results by including the stars of RLV up to the (433) star, in groups which lie between alternate nodes of $\tilde{c}(k)$ as we have done in the OCP-RB.

Three different values of $S(0)$ were used in our calculations ($S(0) = 0.02, 0.023, 0.0256$). These quantity were kept fixed during our search for the coexistence point, so that the latter is specified by the appropriate coupling strength Γ_c for the underlying ionic plasma which describes the microscopic ionic pair structure of the liquid metal. Our results for the various choices of $S(0)$ are not significantly different, in both the values of the order parameters $\rho_{\mathbf{G}}$ and the coupling strength Γ_c [$\Gamma_c = 147.75, 146.44$, and 145.30 respectively], except for the value of the relative volume change η_m [i.e. $\eta_m = 0.054, 0.063$, and 0.072 respectively]. Naturally, the values of η_m increases with increasing $S(0)$. Our results for the case in which $\rho_{\mathbf{G}_2} = 0$ are tabulated in tables(2.10-2.12) and can be directly comparable with those for the OCP-RB in tables (2.5-2.7). We have also estimated the change in the entropy per particles across the phase transition in two different way, i.e. from eqn.(2.4.17) with $\eta_{sl} = 0.19k_B$ as appropriate to liquid *Na*, and from the slope of $\Delta\mu$ at coexistence using eqn.(2.4.20). The volume change has been also calculated in two different routes: the first one is by solving eqn.(2.4.14) with $\Delta\mu = 0$ at coexistence of the two phases , and the second route by using eqn.(2.4.21) which we can rewrite as follows

$$\frac{\eta}{1 + \eta} = \rho_i^2 K_T \left(\frac{\partial \Delta\mu}{\partial \rho_i} \right)_T \quad (2.6.3)$$

where the partial derivative of the density with respect to the pressure is given through its relation with the isothermal compressibility. Finally, the Lindemann ratio can be obtained using eqn.(2.4.27) and all our results are tabulated in table (2.15) and compare with the available experimental data of alkali metals.

Our results for freezing of the OCP-DB can be compared with those for the OCP-RB (in the case were $\rho_{\mathbf{G}_2}$). The main qualitative changes which accompany the appearance of a finite volume change across the phase transition are (a) a decrease in the value of Γ_c , i.e. reduced stability of the fluid phase as first pointed out by Pollock and Hansen ²³; (b) an increase in the entropy of melting; (c) a narrowing of the single particle distribution

around each lattice site in the hot solid. We also notice that there is a reasonable amount of internal thermodynamic consistency in the calculation of Δs and in the calculation of η from the conditions (2.6.1) and (2.6.2), whereas the route leading to a value of η via eqn.(2.6.3) yields a very different result.

As we have already discussed in section (2.5), the most likely source of uncertainty in our results is, of course, the handling of ordering at the (200) star. Two alternative extreme viewpoints could be taken with regard to this failure of the theory. These are (i) the (200) order parameter is genuinely small in the hot bcc crystal, or (ii) microscopic couplings between the ionic order parameters and also between these and electronic order parameters assist ordering in the (200) star. Clearly, our approach does not allow us to discriminate between these possibility, which may in fact be simultaneously correct. We have already examined their separate consequences in section (2.5.1) and (2.5.2) where we asked which value of $\rho_{\mathbf{G}_2}$, or alternatively of $\tilde{c}(G_2)$, would reproduce the value of Γ_c for the OCP-RB of the computer simulation of De Witt et al ⁷⁶.

At this point we have examined the freezing of the OCP-DB with the choice $S(0) = 0.023$ in various ways. First we included the order parameter $\rho_{\mathbf{G}_2} = 0.0038$ in our calculation (being fixed from outside from the OCP-RB). we solved the set of equations (2.4.13) for the microscopic order parameter $\rho_{\mathbf{G}}$, eqn.(2.4.14) for estimating the volume change η (using the condition (2.6.1) for coexistence), and at the same time satisfying the condition (2.6.2). Our results are tabulated in table (2.13), where we can see that freezing occurs at $\Gamma_c = 161.75$ (a bit higher than in the previous case with $\rho_{\mathbf{G}_2} = 0$), whereas the estimated values for the volume change η and the change in the entropy across phase transition are almost the same compared with the values in table (2.9). We have also checked the freezing of the OCP-DB with $S(0) = 0.023$ using the effective direct correlation function $\tilde{c}(G_2) = -0.134$ that we found in the OCP-RB, and we can see that $\Gamma_c = 166.85$ in this case; the volume change has not been affected much whereas the change in the entropy is improved. Our results for this test are also tabulated in table (2.15).

<i>Star</i> \mathbf{G}	$\bar{c}(G)$	$\bar{\rho}_{\mathbf{G}}$	L
110	0.6214	0.770	0.162
200	- 0.4821		∞
211	0.1011	0.498	0.153
220	0.0935	0.412	0.150
310	- 0.0887	0.324	0.151
222	- 0.0736	0.280	0.146
321	0.0227	0.232	0.145
400	0.0567	0.178	0.148
411	0.0211	0.155	0.145
330	0.0211	0.168	0.141
420	- 0.0243	0.134	0.142
332	- 0.0378	0.116	0.141
422	- 0.0193	0.098	0.140
510	0.0083	0.076	0.141
431	0.0083	0.084	0.139
521	0.0211	0.058	0.138
440	0.0062	0.055	0.135
530	- 0.0095	0.045	0.136
433	- 0.0095	0.043	0.137

Table 2.10: *The bcc freezing parameter of the OCP-DB for $S(0) = 0.02$ and $\Gamma_c = 147.75$. $\bar{c}(G)$ are the direct correlation function as a function of Γ at the different stars, $\bar{\rho}_{\mathbf{G}} = \rho_{\mathbf{G}}/(1 + \eta)$, which can be compared with $\rho_{\mathbf{G}}$ of the OCP-RB and $\rho_{\mathbf{G}}$ are the order parameters evaluated from eqn.(2.4.13). L is the Lindemann ratio calculated by eqn.(2.4.27).*

<i>Star</i> \mathbf{G}	$\bar{c}(G)$	$\bar{\rho}_{\mathbf{G}}$	L
110	0.6197	0.773	0.161
200	- 0.4788		∞
211	0.0996	0.502	0.152
220	0.0939	0.415	0.149
310	- 0.0874	0.330	0.150
222	- 0.0735	0.284	0.145
321	0.0218	0.236	0.144
400	0.0563	0.182	0.146
411	0.0216	0.157	0.144
330	0.0216	0.170	0.141
420	- 0.0236	0.136	0.142
332	- 0.0375	0.118	0.140
422	- 0.0195	0.099	0.139
510	0.0087	0.078	0.141
431	0.0087	0.086	0.138
521	0.0211	0.059	0.138
440	0.0065	0.056	0.135
530	- 0.0091	0.045	0.135
433	- 0.0091	0.044	0.136

Table 2.11: *The bcc freezing parameter of the OCP-DB for $S(0) = 0.023$ and $\Gamma_c = 146.44$. $\bar{c}(G)$ are the direct correlation function as a function of Γ at the different stars, $\bar{\rho}_{\mathbf{G}} = \rho_{\mathbf{G}}/(1 + \eta)$, which can be compared with $\rho_{\mathbf{G}}$ of the OCP-RB and $\rho_{\mathbf{G}}$ are the order parameters evaluated from eqn.(2.4.13). L is the Lindemann ratio calculated by eqn.(2.4.27).*

$Star\mathbf{G}$	$\bar{c}(G)$	$\bar{\rho}_{\mathbf{G}}$	L
110	0.6182	0.775	0.161
200	- 0.4759		∞
211	0.0982	0.506	0.152
220	0.0942	0.420	0.148
310	- 0.0863	0.333	0.149
222	- 0.0735	0.286	0.145
321	0.0211	0.239	0.144
400	0.0559	0.185	0.146
411	0.0220	0.159	0.144
330	0.0220	0.173	0.141
420	- 0.0230	0.138	0.142
332	- 0.0373	0.119	0.140
422	- 0.0198	0.101	0.139
510	0.0073	0.079	0.141
431	0.0073	0.088	0.138
521	0.0211	0.061	0.138
440	0.0068	0.057	0.135
530	- 0.0087	0.047	0.135
433	- 0.0087	0.045	0.136

Table 2.12: The bcc freezing parameter of the OCP-DB for $S(0) = 0.0256$ and $\Gamma_c = 145.30$. $\bar{c}(G)$ are the direct correlation function as a function of Γ at the different stars, $\bar{\rho}_{\mathbf{G}} = \rho_{\mathbf{G}}/(1 + \eta)$, which can be compared with $\rho_{\mathbf{G}}$ of the OCP-RB and $\rho_{\mathbf{G}}$ are the order parameters evaluated from eqn.(2.4.13). L is the Lindemann ratio calculated by eqn.(2.4.27).

<i>Star</i> \mathbf{G}	$\bar{c}(G)$	$\bar{\rho}_{\mathbf{G}}$	L	$\bar{c}(G)$	$\bar{\rho}_{\mathbf{G}}$	L
110	0.6387	0.790	0.154	0.6446	0.747	0.172
200	- 0.5168	0.0035	0.531	- 0.1340	0.565	0.170
211	0.1175	0.530	0.146	0.1232	0.469	0.160
220	0.0895	0.444	0.143	0.0879	0.387	0.155
310	- 0.1023	0.356	0.145	- 0.1070	0.292	0.158
222	- 0.0727	0.312	0.140	- 0.0722	0.259	0.151
321	0.0320	0.262	0.139	0.0353	0.213	0.150
400	0.0602	0.203	0.142	0.0612	0.150	0.155
411	0.0159	0.178	0.139	0.0139	0.132	0.151
330	0.0159	0.193	0.136	0.0139	0.155	0.145
420	- 0.0314	0.156	0.137	- 0.0338	0.116	0.148
332	- 0.0401	0.138	0.135	- 0.0407	0.106	0.144
422	- 0.0158	0.117	0.135	- 0.0144	0.087	0.144
510	0.0138	0.091	0.137	0.0158	0.060	0.148
431	0.0138	0.103	0.133	0.0158	0.076	0.142
521	0.0201	0.071	0.134	0.0196	0.047	0.144
440	0.0022	0.069	0.130	0.0007	0.050	0.138
530	- 0.0138	0.056	0.131	- 0.0152	0.038	0.140
433	- 0.0138	0.055	0.131	- 0.0152	0.039	0.139

Table 2.13: *The bcc freezing parameter of the OCP-DB for $S(0) = 0.023$ ($\Gamma_c = 161.75$ in the 2nd – 4th when $\rho_{\mathbf{G}_2}$ was fixed (very small); and $\Gamma_c = 166.85$ in the 5th – 7th when $\bar{c}(G_2)$ was fixed to be -0.1340). $\bar{\rho}_{\mathbf{G}} = \rho_{\mathbf{G}}/(1 + \eta)$.*

2.7 Freezing of Alkali Metals

The combination of the forementioned results for ionic pair structure of the liquid alkalis and of empirical facts relating to their liquid-solid transition (section 2.1 and 2.5) suggests that a primitive view of phase transition of the liquid alkalis could be obtained by regarding the liquid phase near freezing as a classical ionic plasma embedded on a background which is endowed with deformability at long-wavelengths, to allow for perfect screening of the ions by the conduction electrons and for a finite compressibility of the system. Indeed, within the framework of the density wave theory of freezing⁴⁹ the phase transition is associated with the spontaneous appearance of order parameters which are driven, at the simplest level of approximation, by the liquid compressibility and by the structure factor at wave numbers corresponding to the various stars of reciprocal lattice vectors of the crystal. The first star of RLV, i.e. the (110) star for the bcc lattice, is in approximate correspondence with the main peak in the liquid structure factor and thus lies in a region of wave numbers such that electronic screening is already essentially immaterial in determining the ionic pair structure of the liquid metal.

The above picture of the liquid-solid transition in alkali metals, though appealing because of its simplicity, needs careful examination. As we have already discussed the freezing of the OCP on a rigid background (section 2.6), the important role of higher-order corrections in the fluid phase is quite evident in assisting the phase transition. In essence, the fluid structure of the OCP, while appropriately soft to modulation in the (110) star of RLV of the bcc lattice, is rigid against modulation in the (200) star, which must therefore be assisted by couplings to other order parameters. Extrapolating these considerations to freezing of alkali metals, one expects that special attention should be given to the volume change and to the (110) and (200) stars for microscopic order parameters. An earlier evaluation of the phase transition in *Na*⁴⁹ has included only the (110) and (211) microscopic order parameters, in correspondence with the first two peaks of the liquid structure factor.

The relative behaviour of the liquid metal and the OCP model at the (200) star is particularly worth of attention in view of the analysis given by Dobson¹³⁹ of X-ray and neutron diffraction intensity data for liquid *Na* and *Al*, following an earlier proposal by Egelstaff et al¹⁴⁰. Dobson analysis gave evidence for some amount of medium range ordering for the conduction electrons in these liquid metals, which is revealed by excess X-ray scattering intensity peaking in correspondence with the appropriate (111) and (200) stars (fir 2.4). Such ordering is, of course, completely missing in the OCP model and may assist the phase transition in the liquid metals.

Our calculation of freezing of the OCP-DB into the bcc lattice, in the case where we assumed $\rho_{G_2} = 0$ (section 2.6), can be related to the freezing of the

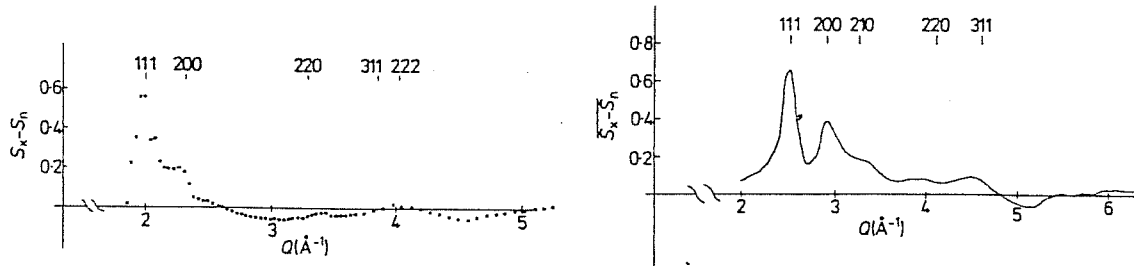


Figure 2.4: *Subtracted structure factor results : (a) for sodium where indexed positions of diffraction are from face centered cubic lattice of $a_o = 5.38\text{\AA}$, and (b) for aluminium where indexed positions of diffraction are from a structure of the original BiF_3 type, assuming that the lattice is made up from electrons occupying the Flourine sites. From ref. [139]*

alkali metals. In fact, the effect of deformability has been introduced through the long-wavelength structure factor $S(0)$ [i.e. through the finite value of c_o]. We have chosen different values of $S(0)$ which falls in the range of the liquid alkali metals near freezing as it is known from available data in the literature. We have noticed an increase in the entropy of melting which is in qualitative agreement with the data on the entropy of melting of alkalin metals relative to that of the OCP-RB (table 2.15), while we have noticed a decrease in the value of Γ_c which is in disagreement with the evidence that we have quoted in section (2.1) for melting of alkali metals both at atmospheric pressure ($\Gamma_c = 180 \div 210$) against $\Gamma_c = 178$ for the OCP-RB and under pressure (Γ_c decreasing with decreasing volume change across the phase transition). Thus, the most likely source of uncertainty in our results is the handling of ordering at (200) star. We have already stated two alternative extreme viewpoints that could be taken with regard to this failure of the theory, that is (i) either the order parameter at the (200) star is very small in the hot solid, or (ii) the microscopic couplings between the ionic order parameters and the electronic parameters assist ordering in the (200) star.

Since our approach does not allow us to check these possibilities, we have examined their consequence separately by asking which value of ρ_{G_2} , or alternatively of $\tilde{c}(G_2)$, would be compatible with a value of Γ_c for the OCP-DB lying in the range appropriate for alkali metal at standard pressure. Our calculations are tabulated in table (2.14), which can be compared with our tabulated results in table (2.15) of the OCP-DB and with the empirical data for alkali metals. The viewpoint (ii) gives overall better agreement with the

data and it is remarkable that in this case the Lindemann ratio at the (200) star near melting falls in the general pattern set by the others. However, in view also of the fact that the diffraction patterns from the liquid alkalis show that the separation between first and second neighbours in the bcc solid has been obliterated on melting, we feel that the viewpoint (i) can not be completely rejected.

In summary, we have interpreted the ionic pair structure in the liquid metals as that of a classical ionic plasma with long-wavelength screening by the conduction electrons. We have seen that within this simple model and within the qualitative uncertainties that affect the theory of the phase transition, a reasonable account of its thermodynamic parameters and of the state of order obtaining in the bcc solid at melting can be obtained.

We have focussed attention in our discussion on the behaviour of the Fourier transform of the periodic crystalline density at the (200) star of reciprocal lattice vectors. The difficulties of the theory in this connection are qualitatively similar to those already well known for Wigner crystallization of the the classical plasma on a rigid background. Our results suggest that the phase transition in the alkali metals may also assisted by medium range ordering of the conduction electrons in the liquid, which is indicated by differences of X-ray and neutron scattering intensities from liquid *Na* as analysed by Dobson ¹³⁹. However, the possibility also suggests itself that anharmonicity in hot bcc crystals may appear as a premelting phenomenon through a rigid decrease of scattering at the (200) Bragg diffraction spots.

$Star\mathbf{G}$	$\bar{c}(G)$	$\bar{\rho}_{\mathbf{G}}$	L	$\bar{c}(G)$	$\bar{\rho}_{\mathbf{G}}$	L
110	0.6804	0.822	0.141	0.6804	0.690	0.194
200	- 0.6108	0.009	0.488	- 0.3503	0.475	0.194
211	0.1600	0.584	0.135	0.1600	0.401	0.175
220	0.0740	0.502	0.132	0.0740	0.365	0.162
310	- 0.1369	0.412	0.120	- 0.1369	0.223	0.174
222	- 0.0660	0.373	0.117	- 0.0660	0.212	0.162
321	0.0566	0.320	0.118	0.0566	0.172	0.159
400	0.0651	0.249	0.132	0.0651	0.099	0.171
411	- 0.0010	0.224	0.129	- 0.0010	0.090	0.164
330	- 0.0010	0.247	0.125	- 0.0010	0.128	0.152
420	- 0.0488	0.202	0.127	- 0.0488	0.083	0.158
332	- 0.0419	0.187	0.124	- 0.0419	0.083	0.151
422	- 0.0035	0.160	0.124	- 0.0035	0.067	0.151
510	0.0279	0.121	0.128	0.0279	0.037	0.162
431	0.0279	0.144	0.123	0.0279	0.060	0.148
521	0.0139	0.100	0.124	0.0139	0.030	0.154
440	- 0.0098	0.102	0.120	- 0.0098	0.041	0.142
530	- 0.0236	0.083	0.122	- 0.0236	0.026	0.147
433	- 0.0236	0.087	0.120	- 0.0236	0.030	0.144

Table 2.14: *The bcc freezing parameter of the alkali metals for $S(0) = 0.023$ ($\Gamma_c = 202.5$ in the 2nd – 4th when $\rho_{\mathbf{G}_2}$ was fixed (very small); and $\Gamma_c = 202.5$ in the 5th – 7th when $\bar{c}(G_2)$ was fixed to be -0.3503). $\bar{\rho}_{\mathbf{G}} = \rho_{\mathbf{G}}/(1 + \eta)$.*

	Γ_c	ρ_G	$\bar{c}(G_2)$	$\Delta s/k_B$	η	$L_{(110)}$	$L_{(200)}$	$L_{(211)}$	$L_{(220)}$	$< L >$
<i>OCP - RB</i>	157.00	0.0	- 0.5046	- 1.00	0.0	0.171	∞	0.159	0.155	0.146 ± 0.003
<i>OCP - RB</i>	178.00	0.0038	- 0.5554	- 0.94	0.0	0.163	0.531	0.153	0.149	0.140 ± 0.003
<i>OCP - RB</i>	178.00	0.5320	- 0.1340	- 0.94	0.0	0.181	0.179	0.166	0.161	0.150 ± 0.004
<i>OCP - DB</i>										
$S(0) = 0.0200$	147.75	0.0	- 0.4821	-1.33 ^(a) , -1.16 ^(b)	0.054 ^(c) , 0.008 ^(d)	0.162	∞	0.153	0.150	0.142 ± 0.002
$S(0) = 0.0230$	146.44	0.0	- 0.4788	-1.39 ^(a) , -1.20 ^(b)	0.063 ^(c) , 0.009 ^(d)	0.161	∞	0.153	0.149	0.140 ± 0.002
$S(0) = 0.0256$	145.30	0.0	- 0.4759	-1.39 ^(a) , -1.20 ^(b)	0.072 ^(c) , 0.010 ^(d)	0.161	∞	0.152	0.150	0.148 ± 0.002
<i>OCP - DB</i>										
$S(0) = 0.0230$	161.75	0.0035 ^(e)	- 0.5168	-1.38 ^(a) , -1.15 ^(b)	0.070 ^(c) , 0.010 ^(d)	0.154	0.531	0.146	0.143	0.136 ± 0.002
$S(0) = 0.0230$	166.85	0.5650 ^(e)	- 0.1340	-1.26 ^(a) , -1.05 ^(b)	0.060 ^(c) , 0.008 ^(d)	0.172	0.170	0.160	0.155	0.146 ± 0.002
<i>Alkali Metals</i>										
$S(0) = 0.0230$	202.50	0.0090 ^(e)	- 0.6108	-1.31 ^(a) , -1.10 ^(b)	0.087 ^(c) , 0.008 ^(d)	0.141	0.487	0.135	0.132	0.124 ± 0.002
$S(0) = 0.0230$	202.50	0.4750 ^(e)	- 0.3503	-1.04 ^(a) , -0.86 ^(b)	0.050 ^(c) , 0.007 ^(d)	0.194	0.194	0.175	0.162	0.156 ± 0.006
<i>Expt</i>	180 \div 210		- 0.600	-0.80 \div -0.85				L		$\simeq 0.12^{(f)}, 0.15^{(g)}$

Table 2.15: The bcc freezing parameter of the *OCP-RB* and of *OCP-DB* for different values of $S(0)$. The data in the last row marked 'Expt' refer to alkali metals at atmospheric pressure. Γ_c is the coupling parameter at phase transition; ρ_{G_2} the order parameter at (200) star; $\bar{c}(G_2)$ the direct correlation function at (200) star; $\Delta s/k_B$ and η are the entropy change and the volume change across transition; $L_{(110)}$, $L_{(200)}$, $L_{(211)}$, $L_{(220)}$ are the Lindemann ratio at the first four stars and $< L >$ is the average value of the Lindemann ratio for the remaining stars up to (433). (a) From eqn.(2.4.17) with $\eta_{sl} = 0.19k_B$ as appropriate to liquid Na; (b) From eqn.(2.4.20); (c) From eqn.(2.4.14), the values following from eqn.(2.7.2) essentially the same; (d) From eqn.(2.4.21); (e) these are $\rho_{\bar{G}} = \rho_G/(1 + \eta)$; (f) calculation in the Debye Approximation by Faber [4]; (g) calculated in the Harmonic approximation by Chaturvedi et al [6].

Chapter 3

FREEZING OF A BOND PARTICLE MODEL FOR LIQUID GERMANIUM

INTRODUCTION

Considerable effort has been given for some years to developing models of interatomic forces aimed at accounting for bond directionality in liquid and amorphous state calculations. In this chapter we are concerned with the freezing of a bond model for liquid germanium.

In section 1 we give a short introduction to the structure of covalently bonded systems, by recalling some of the basic experimental facts relating mainly to the medium-range order that exist in the disordered states of these materials. Various theoretical approaches are also briefly discussed: after a mention of the basic approach using quantal simulation techniques, and in particular the Car-Parrinello method, we refer to models involving three-body potentials to account for the directionality of covalent bonds, and introduce the bond particle model. The early uses of this model in treating the lattice dynamics are reviewed in section 2, which further presents the melting criteria that follow from the model and its use in the evaluation of liquid structure.

Starting from this calculated liquid pair structure, the process of equilibrium freezing is discussed qualitatively in section 3, and evaluated in section 4 within the framework of the density wave theory. Finally, in section 5 we briefly report on an evaluation of freezing for a liquid having the structure of amorphous germanium.

3.1 Introduction to the Structure of Covalently Bonded Systems

Increasing theoretical attention has been given in recent years to the structure of covalently bonded systems in disordered states. An amorphous or vitreous state can be prepared in many of these materials and it is useful to consider its structure in parallel with that of the liquid near equilibrium freezing. In this section we will consider the group-IV and III-V semiconductors, dichalcogenides of group-IV element and some halides of divalent metals. We shall consider in more detail liquid germanium near freezing and amorphous germanium in the following sections.

The electropositive atom in a compound such as $GeSe_2$ or $ZnCl_2$ is tetrahedrally coordinated by atoms of the other species. Fourfold coordination is successfully distinguished from others in the crystal structure classification diagram (fig. 3.1) built by Anderioni¹⁴² for sp bonded (non-transition) AB_2 compounds on the basis of ab initio electronic parameters of the atomic constituents. These are s and p orbital (nodal) radii, which measure the size of core orthogonalisation holes for valence electrons in each angular momentum state. Such atomic parameters reflect basic information on the valence electron states of the constituent elements and hence on the bonding properties.

The classification scheme for sp bonded AB_2 compounds is based on the orbital nodal radii $\mathcal{N}_l^E (l = 0, 1)$ for each element E . Elemental coordinates

$$y_E = \frac{1}{2}(\mathcal{N}_0^E + 3\mathcal{N}_1^E)$$

and

$$x_E = \frac{1}{4}(3\mathcal{N}_0^E - \mathcal{N}_1^E)$$

are constructed from these, and hence compound coordinated $Y = y_A - y_B$ and $X = x_A + x_B$. The elemental coordinate y_E measures the average size of the inner core seen by the valence electrons. Increasingly negative values of Y broadly correspond to increasing ionicity of the bond, while X is an inverse measure of bond directionality¹⁴³. Figure 3.1 shows how the various AB_2 compounds distribute themselves in the (X, Y) plane. The coordination number increase with increasingly negative Y and/or increasing X , and the separation between structures with different coordination numbers is well represented. Tetrahedral-type coordination are found near the left-hand top of the plane, i.e. at low ionicity and strong bond directionality. Among these lie the glass-forming systems.

Tetrahedral units can form a network by connecting in two basic alternative way, i.e. by corner sharing or by edge sharing. There consequently

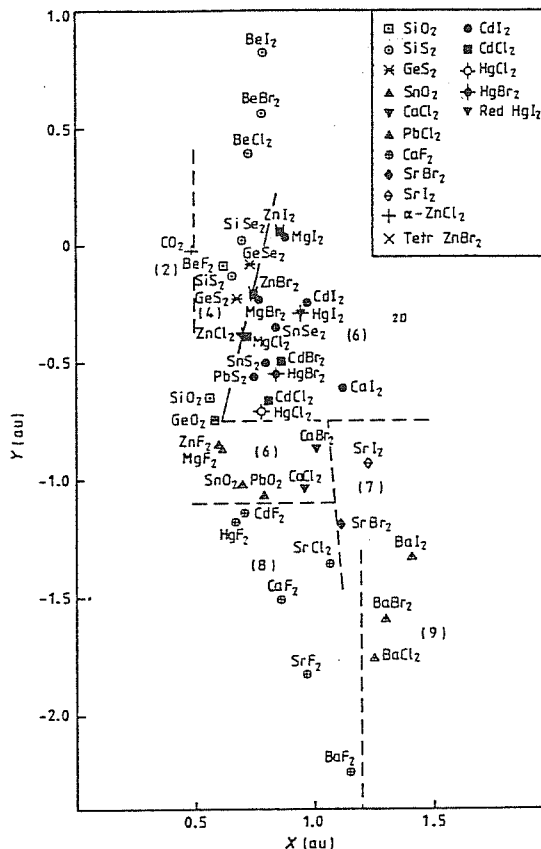


Figure 3.1: Classification of crystal structures for *sp* bonded, double-octet AB_2 compounds. The plot discriminates between three dimensional and layer structures and between different coordinations (in parentheses). Misplacements occur for Hg halides. From ref. [142]

is variety already in the crystal structures that may be realized. For instance, pure edge sharing in $SiSe_2$, mixed edge and corner sharing in $GeSe_2$ and pure corner sharing in SiO_2 yield crystal structures composed of 1D, 2D and 3D regular networks, respectively. Various allotropic crystalline forms may also exist for a given compound, a well-known case being SiO_2 . Figure 3.2 shows all the possible forms of bonding around a tetrahedral unit.

The structure of glassy and liquid states of these compounds can clearly be viewed as disordered networks of somewhat deformable tetrahedra. An important structural question concerns the relative weight of corner and edge sharing in the disordered states. This also has dynamic implications, as studied e.g. by Sugai¹⁴⁴ in the case of *Ge* and *Si* chalcogenide glasses: the structure of the vitreous state is reflected in Raman scattering peaks and their splitting (fig. 3.3). The structure of vitreous silica $\alpha-SiO_2$ was studied through inelastic neutron scattering by Price et al¹⁴⁵: the various peaks in the effective density states $G(E)$ (which is related to the average scattering function $\langle S(k, E) \rangle$) were ascribed to the rocking, bending, and stretching motions of the $Si-O-Si$ bond (fig. 3.4).

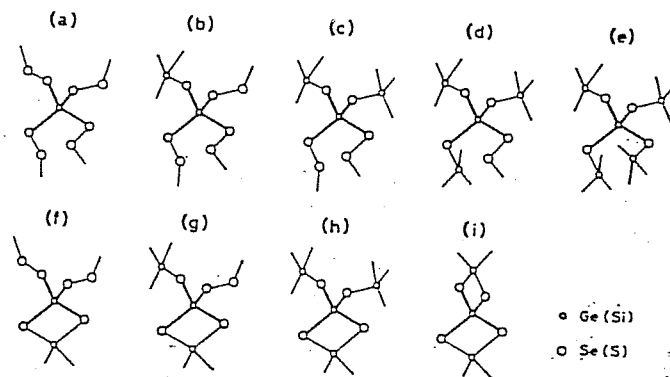


Figure 3.2: All possible forms of bonding around a tetrahedral unit (for Ge and Si chalcogenide glasses, a random network of methane like $MX_{4/2}$ molecules): from (a)-(e) consist of X-X bonds and corner sharing bonds; from (f)-(h) consist of X-X, corner sharing and edge sharing; and (i) is for only edge sharing bonds.

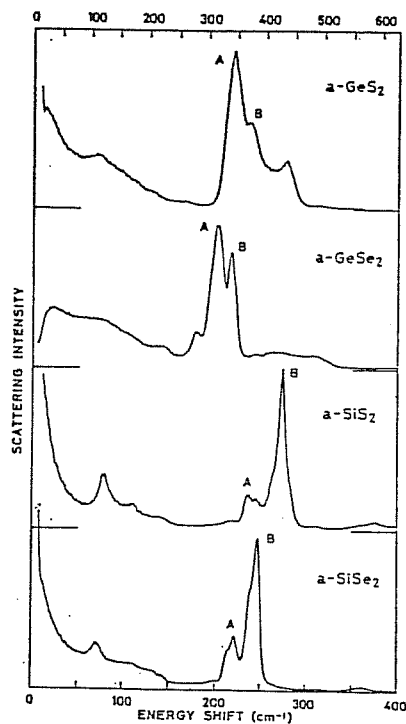


Figure 3.3: The Raman spectra in GeS_2 , GeSe_2 , SiS_2 and SiSe_2 glasses. The lower scale is for selenides and the upper is for sulfide. The upper scale is contracted by $(M_S/M_{Se})^{1/2}$. From ref. [144]

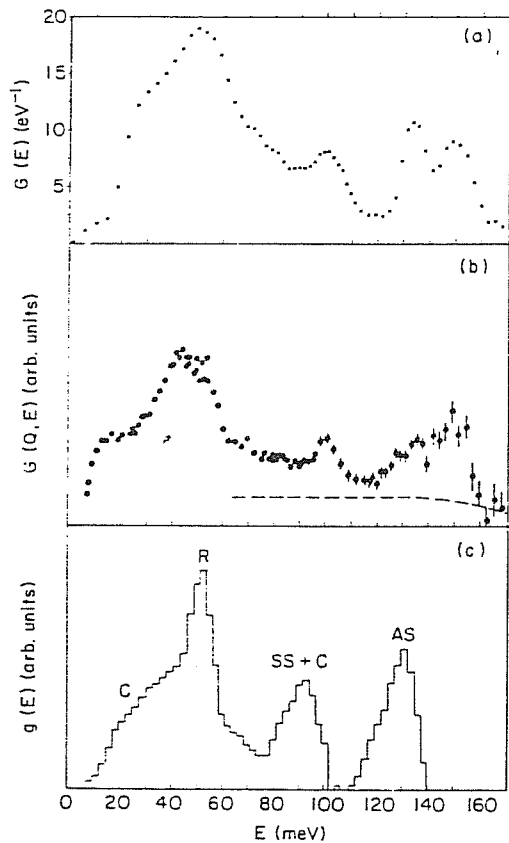


Figure 3.4: (a) Effective density of states; (b) neutron spectrum with $Q-E^{1/2}$; (c) density of state calculated from the 334-atom Bell and Dean model, with boundary atoms damped. The features labeled As, SS, R and C in (c) correspond respectively to different modes in terms of the direction of motion of an O atom relative to its two Si neighbours being “asymmetric stretch”, “symmetric stretch”, and “rocking”, and to modes dominated by “cation” (Si) motion. From Price et al [145].

3.1.1 Some Basic Experimental Facts Concerning Structure

In the analysis of glassy structure by diffraction methods, the standard procedure involves the measurement of spherically averaged intensity data over a range in $k (= 4\pi \sin \theta / \lambda)$ from 0.2 \AA^{-1} to 20 \AA^{-1} . These data are then elaborated to extract the familiar pair distribution, or radial density, function. There has been enormous amount of data collected over the years on glassy (non-crystalline or amorphous) solids and our intent in this section is to outline some general features of glassy structure.

The diffraction patterns of glasses reflect the medium-range order arising from the connectivity of basic tetrahedral units through a first sharp diffraction peak (FSDP) in the vicinity of $k_p \simeq 1.0 - 1.5 \text{ \AA}^{-1}$. Moss and Price¹⁴⁶ have noticed that the general relation $k_p d \simeq 2.5$ holds between the FSDP position k_p and the first-neighbour distance d in a variety of halide, oxide and chalcogenide glasses, irrespectively of the network dimensionality in their crystalline state. Figure 3.5 illustrates the FSDP for several glasses, by plotting the neutron structure factor $S(k)$ versus kd , whereas in table (3.1) the position of the FSDP is given for a number of glasses along with $k_p r_s$, where r_s is the mean interatomic spacing derived from the macroscopic number density ρ ($\rho^{-1} = \pi/6r_s^3$). For oxides (excepting B_2O_3), halides, chalcogenides, As and P , $k_p d$ lies at about 2.5, with a spread between 2.3 and 3.1. $k_p r_s$ also clusters between 3.7 and 4.8. For Se and Ge instead one has $k_p d \sim 4.5$, falling near the values given by the "pre-peak" in neutron scattering from metallic glasses at $k_p d \sim 4.9$. Moss and Price suggest that the observed diffraction patterns could arise from essentially random packing of structural units, through a combination of the form factor for individual units and interference function for their centres.

The main observed features of the diffraction pattern, including the FSDP, are preserved in the liquid state in $ZnCl_2$ ¹⁴⁷ and in $GeSe_2$ ¹⁴⁸. In fact, the height of the FSDP in molten $GeSe_2$ is essentially the same as in the low-temperature glass, whereas the other features of diffraction pattern show the expected thermal attenuation and broadening. On the other hand, although the diffraction patterns of amorphous Silicon¹⁴⁹ and germanium¹⁵⁰ show a FSDP lying at $k_p \simeq 4.5$, the diffraction patterns of these elemental semiconductors in the liquid state near freezing¹⁵¹ show clear differences from those of their amorphous state. Indeed, melting at standard pressure brings elemental and polar III-V semiconductors from tetrahedrally coordinated open structures into metallic liquids having higher density than the solid and first-neighbour coordination number close to seven^{152,13}. Their liquid structure is nevertheless quite distinct from that of other liquid metals[?]. Specifically, their first-neighbour coordination number of order seven is still relatively low and a second shell of neighbours is seen to lie at a short distance

<i>System</i>	$k_p(\text{\AA}^{-1})$	$d(\text{\AA})$	$k_p d$	$r_s(\text{\AA})$	$k_p r_s$
<i>Oxides and halide glasses</i>					
B_2O_3	1.57	1.36	2.14	2.90	4.55
SiO_2	1.55	1.61	2.50	3.07	4.75
GeO_2	1.55	1.74	2.70	3.12	4.83
BeF_2	1.63	1.54	2.51	2.92	4.76
$ZnCl_2$	1.09	2.29	2.49	3.76	4.10
<i>Chalcogenide Glasses</i>					
$P_{40}Se_{60}$	1.16	2.29	2.66	3.78	4.38
$Si_{32}Se_{68}$	1.02	2.30	2.35	3.92	3.99
$Si_{24}Te_{76}$	1.04	2.60	2.69	4.09	4.25
GeS_2	1.04	2.22	2.31	3.76	3.91
$GeSe_2$	1.01	2.37	2.39	3.86	3.90
As_2Se_3	1.27	2.44	3.10	3.77	4.79
As_2S_3	1.26	2.28	2.87	3.66	4.61
<i>Elemental Semiconducting Glasses</i>					
Se	1.88	2.37	4.56	3.89	7.32
$P(\text{red})$	1.04	2.29	2.38	3.54	3.69
As	1.03	2.49	2.56	3.69	3.80
Ge	1.89	2.46	4.43	3.64	6.88
<i>Metallic Glasses (Pre Peak)</i>					
$Co_{80}P_{20}$	2.30	2.34	5.38	2.77	6.37
$Ni_{35}Zr_{65}$	1.62	2.66	4.30	3.31	5.36
$Ni_{40}P_{60}$	1.90	2.60	4.94	3.03	5.76
<i>Metallic Glasses (Main Peak)</i>					
$Co_{80}P_{20}$	3.16	2.34	7.39	2.77	8.75
$Ni_{35}Zr_{65}$	2.62	2.66	6.97	3.31	8.67
$Ni_{40}P_{60}$	2.91	2.60	7.57	3.03	8.82
Fe	3.09	2.55	7.88		

Table 3.1: Positions k_p of the first peak in the diffraction pattern compared with the nearest neighbour distance d and mean interatomic spacing r_s ($\rho^{-1} = \pi/6r_s^3$). From ref.[146].

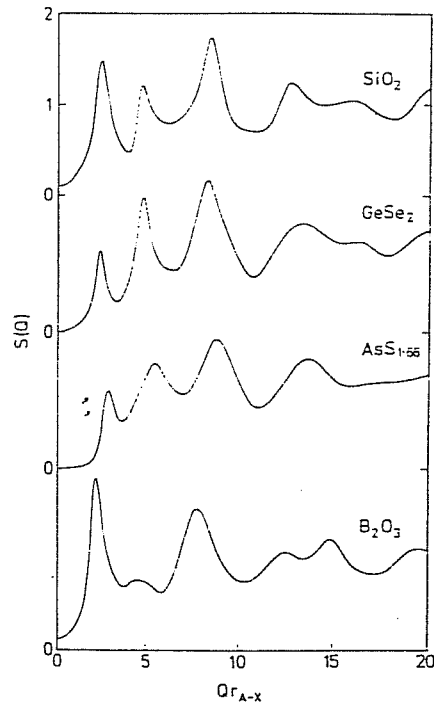


Figure 3.5: Neutron structure factors $S(Q)$ for vitreous SiO_2 , GeSe_2 , As_2S_3 and B_2O_3 . From ref. [146]

beyond the first shell, in a region of interatomic separations where the pair distribution function $g(r)$ in other liquid metals has its minimum (fig. 3.6)¹⁵³. Similarly, the liquid structure factor $S(k)$ shows a distinctive shoulder on the large- k side of its main peak, merging into a single symmetric broad peak with increasing temperature of the liquid phase (fig. 3.7)¹⁵³. The FSDP observed in the amorphous state at $k_p \simeq 1.9 \text{ \AA}^{-1}$ is no longer evident in the melt. Similar structural features have been observed in the total diffraction pattern from molten GaAs ¹⁵⁴.

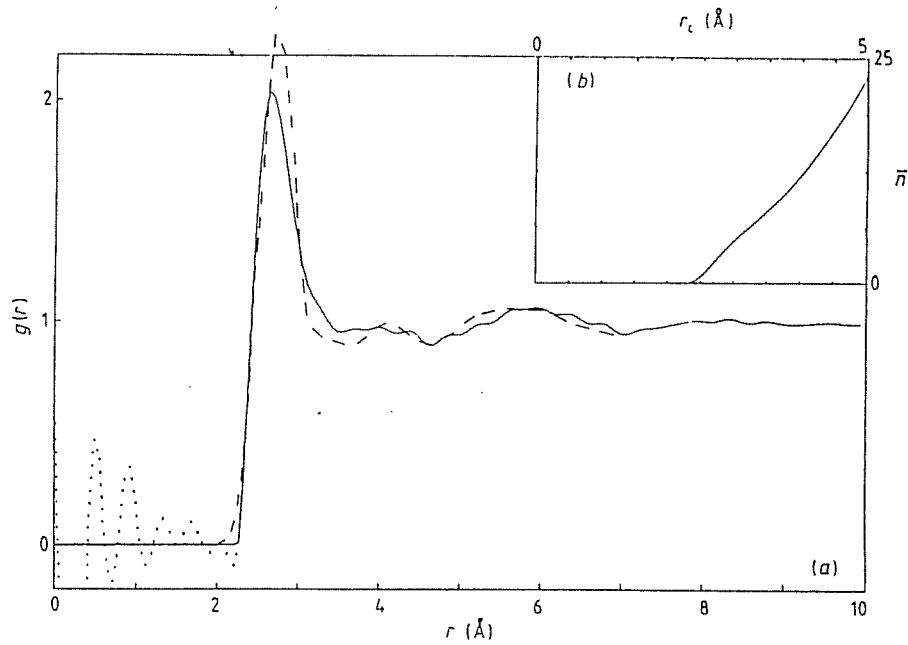


Figure 3.6: (a) The full curve give $g(r)$ for liquid Ge at 1000°C from the neutron diffraction study by Salmon [1]. The dotted curve shows the extent of the unphysical features at $r < 2.25\text{\AA}$ which results from Fourier transforming the experimentally determined $S(k)$. The broken curve gives the X-ray diffraction data by Waseda [13] for liquid Ge at 980°C . From ref.[153]

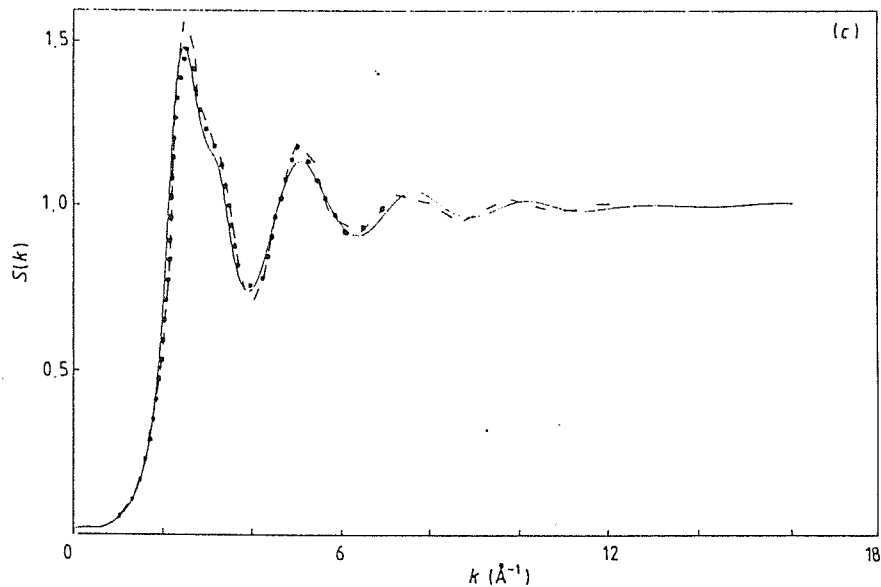


Figure 3.7: The $S(k)$ for liquid Ge obtained from neutron diffraction data (full curve, at 1000°C , by Salmon [1]) and from X-ray diffraction data (broken curve, at 980°C , by Waseda [13]); dotted curve represent also X-ray diffraction data at 1047°C . After Salmon [153].

3.1.2 Theoretical Approaches

A number of theoretical approaches have been developed in the recent literature to deal with the disordered states of the above systems. A specific role of the valence electrons is clearly expected in group-IV elements or III-V compounds and can be exhaustively examined by quantal simulation techniques. The Car-Parrinello method, combining density functional theory for the valence electron density with molecular dynamics for the ionic cores, has been tested on silicon¹⁵⁵ and has usefully supplemented experiment in the case of liquid carbon¹⁵⁶. The metallic melt of elemental semiconductors has also been investigated by conventional pseudoatom approach of the electron theory of metals¹⁵⁷.

Within the theoretical framework provided by the concept of effective atom-atom interactions, the directionality of covalent bonds can be successfully modelled by invoking suitable three-body contributions to the interatomic potential energy function for computer simulation, in addition to pair-potentials¹⁵⁸. Without inclusion of such three-body forces, the diamond crystal structure in elemental semiconductors is found to be unstable against close-packed structures. Table (3.2) compares the structure factor features from calculation of Stillinger and Weber¹⁵⁸ with experimental results for liquid *Si*. The model potential-energy function proposed by Stillinger and Weber has been adopted by a number of other authors, among which we mention Kluge et al¹⁵⁹ and Luedtke and Landman¹⁶⁰ for amorphous silicon (fig. 3.8) and Vashishta et al¹⁶¹ for the molten and glassy states of *GeSe₂* (fig 3.9). These models attribute to three-body forces the role of selecting preferred values for bond angles and of describing stiffness against bond bending. It is remarkable that such interatomic force models are able to account for the observed structural features of the disordered solid and liquid states for both dichalcogenides and elemental semiconductors, in spite of the fact that the melting process is qualitatively different in these two types of material and that the models do not explicitly display the structural role of the valence electrons. The evaluation of partial structure factors and of distributions of bond angles in these simulations provides additional insight into the state of short- and medium-range order in the disordered materials, subject to the limits of realism and accuracy of the model. In addition, the approach of Vashishta et al¹⁶¹ to vitreous and liquid *GeSe₂* offers a natural explanation for the afore-mentioned observed insensitivity of the FSDP to temperature, by suggesting frustration of medium-range order in the glass by its higher density.

From the viewpoint of conventional liquid structure theory based on the use of integral equations relating structure to interatomic forces, it is pertinent to ask whether strongly directional interatomic forces could still be mimicked through suitable pair potentials. Ballone et al¹⁶² have drawn

Feature	Moleculardynamics	Experiment
FirstPeak	2.53	2.80
Shoulder	3.25	3.25
SecondPeak	5.35	5.75
ThirdPeak	8.16	8.50
FourthPeak	10.60	11.20

Table 3.2: Comparison of structure factor positions in k space. (Units for k are \AA^{-1}) from ref [158].

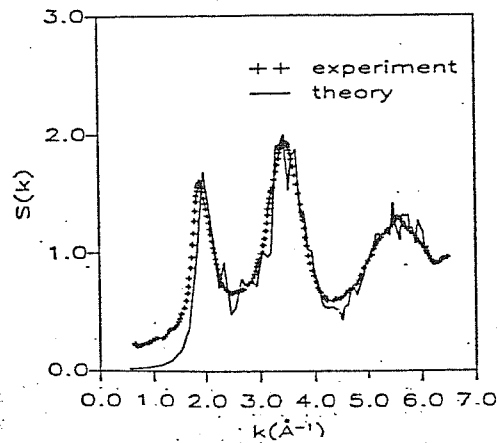


Figure 3.8: A comparison of the neutron scattering structure factor $S(k)$ for amorphous silicon and the Kluge et al calculation [159] using Stillinger and Weber potential for the system at 427 K.

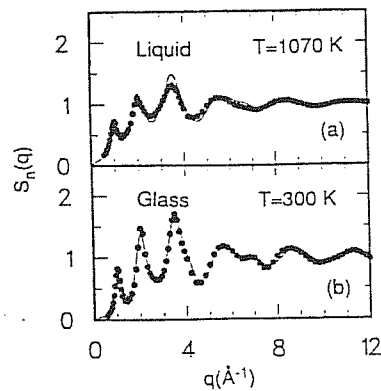


Figure 3.9: Neutron static structure factors in glassy and molten GeSe_2 . Continuous curve is MD and solid circles are from neutron experiment. From ref. [161]

attention to non-additive charged hard sphere models in relation to molten $ZnCl_2$. The crucial observation ¹⁴⁷ is that $Zn - Zn$ first neighbour distance in the melt lies at about 3.8\AA , whereas Coulomb repulsions between cations would place their separation at about 5\AA as is indeed observed in molten alkaline earth chloride ^{88,163}. Both central distance-dependent screening of Coulomb interactions and angular-dependent forces, which may be mimicked through nonadditivity of ionic radii, are needed for a qualitative account of the structural data ¹⁶².

At a more general theoretical level an interesting proposal, pertaining to three-body interaction models, has been made by Iyetomi and Vashishta ¹⁶⁴. By an extension of density functional theory for inhomogeneous systems, in which they regard the free energy as a functional of both the single-particle density and the two-body distribution function, they discuss how three-body interactions could be incorporated into an effective pair potential for the evaluation of the two-body distribution function $g(r)$ of the homogeneous disordered material. The simplest expression for the effective pair potential, as obtained within a hypernetted chain (HNC) approximation scheme, involves a dependence on $g(r)$, since it is obtained by averaging the three-body interaction between a given pair of particles and a third particle by means of the two-body distribution function relating each member of the pair to the third particle.

An alternative route for the theory involves the development of models which describe at a primitive level the interatomic bonds and keep track of their correlations. A model of this type has been proposed in an entirely different context by Smith and Nezbeda ¹⁶⁵. It relies on near-peripheral attraction sites on hard spheres or dumbbells in order to mimic association and polymerization in hydrogen-bonded fluids. Kolafa and Nezbeda ¹⁶⁶ have used such a model in Monte Carlo studies of water and methanol, while Wertheim ¹⁶⁷ has made significant progress in solving it by integral equation techniques of the Percus-Yevick type. Extensions of this model, invoking direct correlations between the peripheral interaction sites, may possibly be useful to deal with glass-forming liquids. The configuration of the interaction sites on the periphery of each atomic sphere would be determined by the preferred bond angles and strong directionality in the effective atom-atom interactions would clearly result.

In relation to the molten state of semiconductors, on the other hand, Ferrante and Tosi ¹⁶⁸ have proposed and examined pseudoclassical models for germanium, which are inspired to the bond-charge model proposed a long time ago by Phillips ¹⁶⁹ for their crystalline state. We are going to report the main features and results of the bond-particle models in the following section.

3.2 Bond - Particle Model for Elemental Semiconductors

In this section we are going to discuss the bond-particle model and its application to the structure of elemental semiconductors in the liquid and supercooled liquid state. This model introduce along with the atomic component, an auxiliary component (the bond-particle) to account for the chemical bonding and to mimic the angular dependence of the atom-atom interactions.

The bond-charge model was first proposed by Phillips ¹⁷⁰ for crystalline elemental semiconductors. Martin ¹⁷² applied this model in the calculation of phonon-dispersion curves in silicon. A modified bond-charge model was proposed by Weber ¹⁷³, with application to phonons in Ge.

3.2.1 Bond-Charge Model for Lattice Dynamics

The bond-charge model as proposed by Phillips represents the electronic charge distribution in each covalent bond as a point-like charge of suitable amount, localised at mid distance between each pair of neighbouring atoms. the bond charges participate in the lattice dynamics and indeed an important application of the model has been its use in the calculation of phonon dispersion curves by Martin. He obtained fair agreement with experimental dispersion curves, except that the flattening of the transverse acoustic (TA) phonons could not be reproduced.

As early as 1959, Cochran ¹⁷⁴ pointed out that this flattening of the TA branches, which in a Born and von Kàrmàn model requires very long-range forces constants with a large number of parameters of doubtful significance ¹⁷⁵, is in fact due to mainly short-range ion-electron and electron-electron interactions. Cochran suggested a model known as the shell model (SM), in which he represented the valence electron charge density around the atom as a rigid shell coupled with the atom through an elastic force, and introduces non-central forces between the nearest-neighbour shells to account for the interaction between the atoms.

In what follows we will give in some detail the argument presented by Phillips ¹⁷⁰ and the calculation of Martin ¹⁷². The electronic dielectric constant ϵ_o , which describes the screening of ion-ion forces at distance large compared to a nearest-neighbour distance, in semiconductors has a finite value. This is due to the presence of the gap, given by the Penn relation ¹⁷⁶

$$\epsilon_o = (\hbar\omega_p/E_g)^2 C + 1$$

where ω_p is the frequency and C is a constant of order unity.

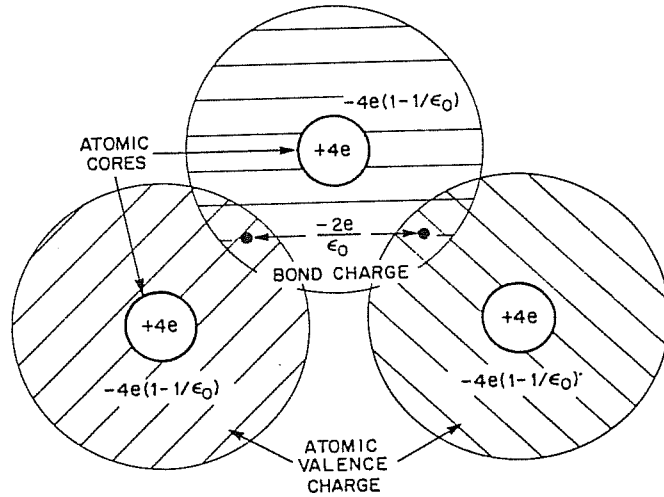


Figure 3.10: Separation of valence charge distribution in diamond-type semiconductors into atomic and bonding parts. From ref. [170]

In a diamond-type semiconductor, the valence charge is next subdivided into two parts. The first (of magnitude $Z^{(1)}$) is centered on the atoms and consists of screening clouds which are approximately spherically symmetric about each atom. The second part of the valence charge, which describes the valence bonds, is represented by point charges of magnitude $Z^{(2)}$ centered at bond sites half-way between nearest-neighbours. The bonding charge is given by

$$Z^{(2)} = -|e|/\epsilon_0$$

per atom, so the charge per bond is $Z_b = 2Z^{(2)}$. The nature of the electron charge distribution is sketched in fig. 3.10, where we can see that the charge per bond is $Z_b = -2e/\epsilon$ and the charge of the screening cloud is $Z^{(1)} = -4e(1 - 1/\epsilon_0)$ surrounding the atomic cores of $Z = +4e$. In the case of *Ge* with $\epsilon_0 = 16$, $Z_b = 0.125e$.

Following Phillips's bond-particle model, Martin has used a dielectric screening model to calculate the phonon spectrum of *Si*. He assumed that the bare-ion-core potentials are screened in a nearly free-electron-like manner, i.e. by the diagonal elements of the inverse dielectric function $\epsilon^{-1}(\mathbf{q} + \mathbf{G}, \mathbf{q}' + \mathbf{G}')$. This metal-like binding gives rise to short-range central forces between the ions, which die out rapidly beyond nearest neighbours. The effect of the off-diagonal elements of ϵ^{-1} is described by Coulombic interactions involving the bond charges. These forces represent the covalent character of the binding; they lead to effective noncentral forces between the ions, which produce the stability of the diamond structure against shear. The specific assumption was made that the bond charges stay midway between the ions, even when the ions are displaced.

In detailed calculations Martin¹⁷² considered the Coulombic interaction between the bond charge-ion and bond charge-bond charge as $(Z_+ Z_-)/\epsilon_0 r$

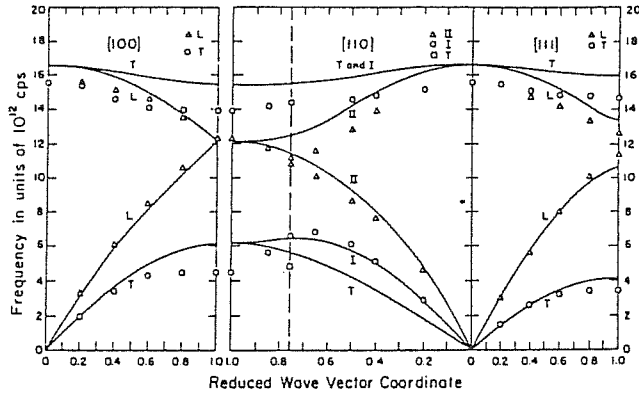


Figure 3.11: *Phonon dispersion curves for Si for the principle symmetry directions [100], [110], [111] after Martin [172]. Solid line shows the theoretical calculations, circles, triangles and squares are the experimental data. From ref. [172]*

and $(Z_+Z_-)/\epsilon_0 r$ with Phillips's values $Z_+ = 4$ and $Z_- = -2$. Then the dynamical matrix \tilde{D} was expressed as $\tilde{D} = \tilde{D}^{II} + \tilde{D}^{IB} + \tilde{D}^{BB}$ where \tilde{D}^{II} includes all the diagonal terms, which are of the form of central ion-ion interaction, and the terms \tilde{D}^{IB} and \tilde{D}^{BB} are, respectively, appropriate sums over ion-bond and bond-bond interactions, thus introducing effective noncentral forces between the ions. Within this model the phonon dispersion curves for Si were calculated for the principal symmetry directions [100], [110] and [111] and are represented in fig. 3.11. The results obtained in this model suggested a two-parameter "simple bond-charge" model which is applicable to all the diamond-structure crystals because it contains only purely Coulombic and nearest neighbour non-Coulombic forces. In this simplified model the bond charge Z'_b is one of the two parameters, to be compared with the value given by Phillips ($Z_b = -2e$), whereas the second parameter describes the non-Coulombic forces. Within this simple bond-charge model the dispersion curve along the [100] direction in diamond and Si are illustrated in fig. 3.12, and the resulting values for the parameter Z'_b are $Z'_b = -3.2e$ for diamond and $Z'_b = -2.6e$ for Ge. This simplified model reproduce qualitatively the main feature of the dispersion curves.

A modified bond-charge model was later proposed by Weber¹⁷³ for phonons in semiconductors of diamond structure. The flattening of the transverse acoustic phonon branches in these materials was reproduced and is due to interactions involving the bond charges, when these move adiabatically. Good agreement with experiment was obtained using this model for phonons in Ge.

Weber introduces four type of interactions: (a) central ion-ion forces; (b) Coulomb interactions of the ions and bond charges; (c) central ion-bond charge forces and (d) bond-bending forces. These forces are metal-like in (a)

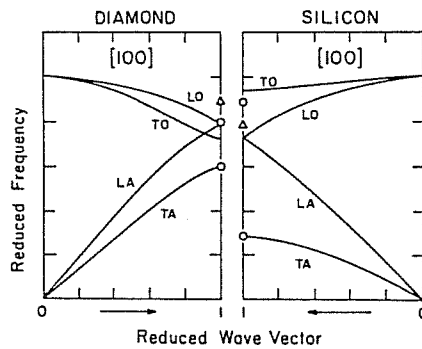


Figure 3.12: Comparison of diamond and Si [100] vibration frequencies, using the simple bond charge model suggested by Martin [172].

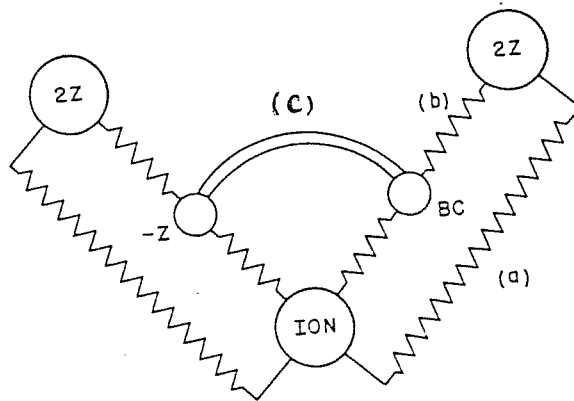


Figure 3.13: Schematic presentation of the adiabatic bond charge model proposed by Weber [173]. (a) represents ion-ion interaction. (b) represents ion-bond charge interaction responsible for stabilizing the bond-charge in its equilibrium position. (c) represents bond-bond (noncentral) interaction.

and covalent in (b)-(d). These four types of interactions are schematically sketched in fig 3.13 and the constraint that the bond charges are fixed on the midway position between the atoms is removed. Instead, they are allowed to move adiabatically following the movement of the ions. Short rang ion-bond charge forces are introduced to stabilize the bond charges in their sites. This model employs four-five disposable parameters and was applied in lattice dynamics calculation, *Si*, *Ge* and α -*Sn*, with good agreement with experimental data (fig. 3.14).

An extension of Weber's model had been developed by Goldberg et al ¹⁷⁷ and Winer and Wooten ¹⁷⁸ in order to study the vibrational properties of metastable phases of *Si* and *Ge*. The extension takes into account distorted bond lengths and angles.

Finally, electronic charge densities were calculated by Walter and Cohen ¹⁷⁹ for different diamond and Zinc-blend semiconductors, using wave

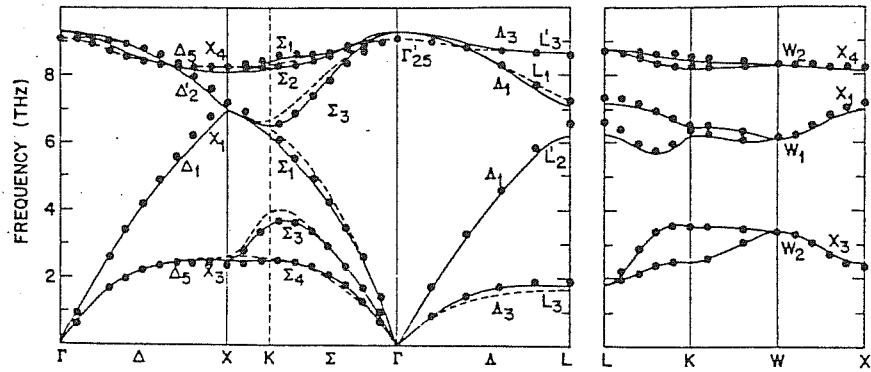


Figure 3.14: Phonon dispersion curves for Ge. Solid line shows the theoretical calculation by Weber [173]. Circles are experimental data and dashed lines are depict results of a bond charge model. From ref. [173].

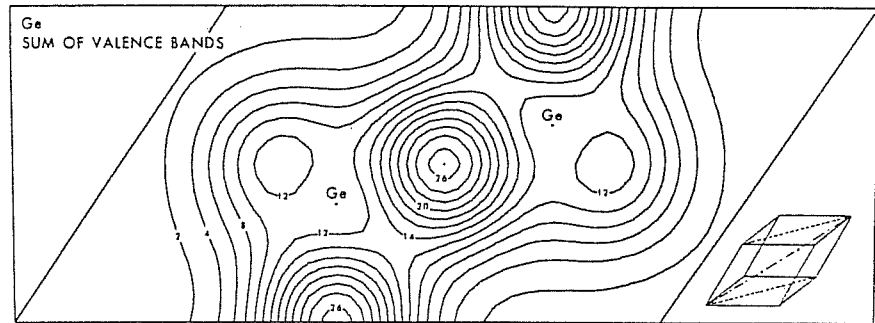


Figure 3.15: A topological map of the valence pseudocharge of Ge in the (110) plane. The position of this plane in the unit cell is shown in the inset. From ref. [179]

functions derived from pseudopotential band-structure calculations. The results of these calculation were used to analyse the bonding properties of the different crystals, and were also used to estimate the covalent-bonding charge Z_b . In the case of Ge the calculated value was $Z_b = -0.146$, which is not far from the value calculated within the Phillips model ($Z_b = -0.125$). Figure 3.15 illustrates the valence electron density contour map in the $[1\bar{1}0]$ plane, where the covalent bonding is seen to be an important factor in the total valence charge distribution. The symmetry of the bond charge (neglecting the effect of overlap with adjacent bonds), but the actual ellipsoidal distribution is nearly spherical, with a small elongation along the bond axis.

3.2.2 Melting of Elemental and III-V Semiconductors

At melting group IV elemental and group III- group V polar semiconductors suffer breakage in the covalent bond with a collapse in volume, a marked increase in near neighbour coordination, and a change in electrical transport character to metallic-type conductivity. Such radical changes in atomic and electronic structure on melting can be viewed in a primitive chemical picture of bonding as associated with a release of valence electrons from interatomic bonds into conduction states.

The above elementary picture of semiconductor melting is naturally related to the bond charge model of Phillips¹⁶⁹, that we have already discussed in the previous section. Such a primitive model for semiconductor melts was explored by Ferrante and Tosi¹⁶⁸ with specific application to the liquid structure of germanium as a test case. They regarded the *Ge* as a mixture of hard-sphere atoms and point-like bond particles, with mutual attractive interactions which can induce localization of bond particles between pairs of atoms under steric constraints limiting the coordination of an atom by bond particles to a maximum of 4 in tetrahedral configuration. Such constraints can be most simply imposed by fixing the distance of closest approach between bond particle from tetrahedral coordination geometry. The localizing interaction are alternatively chosen as Coulombic, as in the original model of Phillips, or represented by a narrow attractive well attached to the surface of each atom. In either case there is a simple coupling strength parameter in units of the thermal energy, which can be continuously varied through the liquid phase. It is given respectively, by $\Gamma = z^2 e^2 / ak_B T$, where z is the amount of bond charge and $a = (4\pi n_A)^{-1/3}$ in terms of the atomic number density n_A , or by $V^* = V/k_B T$, where V is the well depth. This model resembles the structure of real liquid germanium when the coupling strength parameters take the approximate values $V^* \simeq 7.5$ or $\Gamma \simeq 24$. Given the melting temperature and the density of germanium. these values can be compared with the estimated values (a) from knowledge of the valence-conduction energy gap E_g of *Ge* at room temperature ($V \simeq E_g \simeq 0.7\text{ev}$ yields $V^* \simeq 6$) and (b) from the estimates of bond charges ($z \simeq 2/\sqrt{\epsilon_o} \simeq 0.5$, or $z \simeq 0.65$ and $z \simeq 0.40$ from the fits of Martin¹⁷² and Weber¹⁷³ to phonons, yield Γ in the range 50 – 20).

The similarity in melting behaviour for elemental and III-V polar semiconductors immediately suggests the alternative melting criteria $T_m \propto n^{1/3}/\epsilon_o$ or $T_m \propto E_g$ for the melting temperature satisfied in these materials at standard pressure¹⁶⁸. Figure 3.16 shows the correlations of the melting temperature with the valence-conduction band gap and with the quantity $n^{1/3}\epsilon_o$, which reflect satisfaction of the relations stated above for the group IV elements and group III-group V compounds.

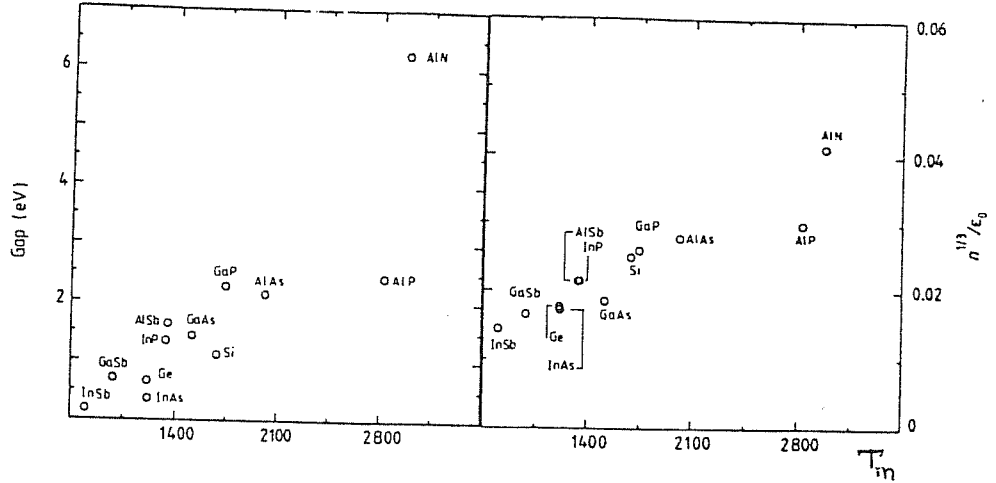


Figure 3.16: Correlation of the melting temperature T_m of elemental semiconductors and III-V compounds with the valence conduction band gap E_g (left) and with the quantity $n^{1/3}\epsilon_0$, (right), where n is the number of atoms per unit volume and ϵ_0 the static dielectric constant of the crystal. From ref. [168].

3.2.3 Bond Particle Models for Liquid Structure

In this section the extension and application of bond-particle models to the liquid structure of *Ge* by Ferrante and Tosi¹⁶⁸ are presented. Their starting point is well known of a two-component liquid as a mixture of hard spheres (of very different sizes in this case). As we have mentioned the bond particle component is subject to localization between pairs of atoms by attractions to the atomic components. Localization is constrained by an upper limit of four on the local coordination of atoms by bond particles through non-additivity of hard-sphere diameters, by fixing a distance of closest approach between bond particles from the size of a tetrahedron inscribed in the atomic sphere.

Their aim behind examining the model as formulated above was to follow the structural evolution of both the atomic (*A*) component and the bond particle (*B*) component as temperature is lowered from hot liquid states to strongly supercooled states. Directionality of effective atom-atom interactions and angular interatomic correlations, ultimately leading to fourfold interatomic coordination, are progressively built into the model as localization of bond particles sets in and grows. The model involves only atom-atom (*A* – *A*), atom-bond (*A* – *B*) and bond-bond (*B* – *B*) pair potentials and can be solved for liquid structure by standard integral equations techniques of liquid-state theory. They examined its solution in the hypernetted chain approximation (HNC) and in one of its currently available refinements (HMSA) due to Zerah and Hansen¹⁸¹.

Ferrante and Tosi evaluated the structure of a two-component fluid of hard spheres, with components *A* and *B* having number density n_A and $n_B = 2n_A$ at temperature T . The hard-sphere interactions are characterized by three distances of closest approach (σ_{AA} , σ_{AB} and σ_{BB} , say). The hard-

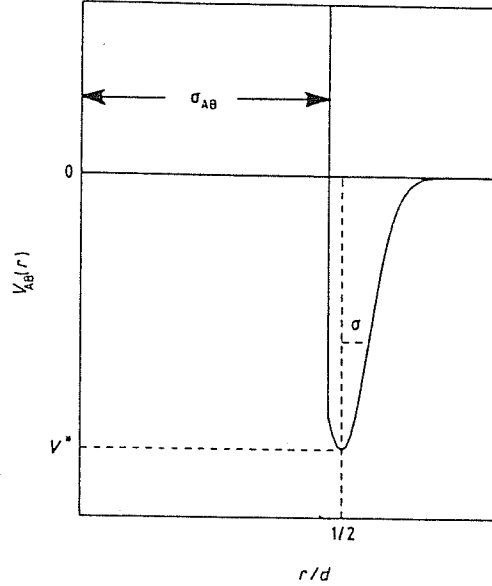


Figure 3.17: Atom-bond particle interaction potential versus distance in the LAM. From ref.[168]

sphere contact distances satisfy the approximate relations $\sigma_{AA} \simeq 2\sigma_{AB} \leq d$, where d is the first-neighbour distance in the liquid, and $\sigma_{BB} \geq (2/3)^{1/2}\sigma_{AA}$. These relations imply that, even though the B component is essentially point-like compared with the A component, no more than four B particles can be found in immediate contact with the A particle. The atom-bond interactions lead to strong relative ordering of the two components in the liquid can be chosen as a localized attraction (localized attractive model, or LAM) in the form of a narrow potential well centered at a distance $d/2$ from the center of each A particle and uniformly spread over its surface (see fig. 3.17). The well is taken to have a Gaussian shape of half-width σ and depth V , with $\sigma \simeq 1/2d - \sigma_{AB}$. The well depth V enters the model only in units of the thermal energy $k_B T$, yielding a coupling strength parameter $V^* = V/k_B T$ which is allowed to increase continuously from zero in order to follow the process of localization of the bond particles.

Alternatively, the hard-spheres are allowed to carry charges and localization is left to $A - B$ attractive Coulomb interactions. We shall focus below on the results obtained in the LAM starting from the atom-bond (AB) and atom-atom (AA) pair distribution functions at $V^* = 0$, fig 3.18 illustrates how localization of bond particles proceeds in the LAM with increasing V^* and the structural changes that it induces in the atomic component, down to strongly supercooled liquid states. Bond-particle localization starts to appear at $V^* \simeq 2$ and grows rapidly henceforward, with the exchange of bond particles between localized states and free states (as measured by the height g_{AB} of the main minimum in $g_{AB}(r)$) being rapidly suppressed and the atom-bond coordination number (N_{AB}) increasing towards the value 4. At $V^* \simeq 7$ (close to the value of $E_g/k_B T_m$ for Ge), localization is sufficiently strong to split the first atom-atom coordination shell into two shells. This is seen in fig 3.18^{182,183} from the behaviour of the atom-atom coordination number (N_{AA}) and of the position of the main minimum (R_{AA}) in $g_{AA}(r)$. At

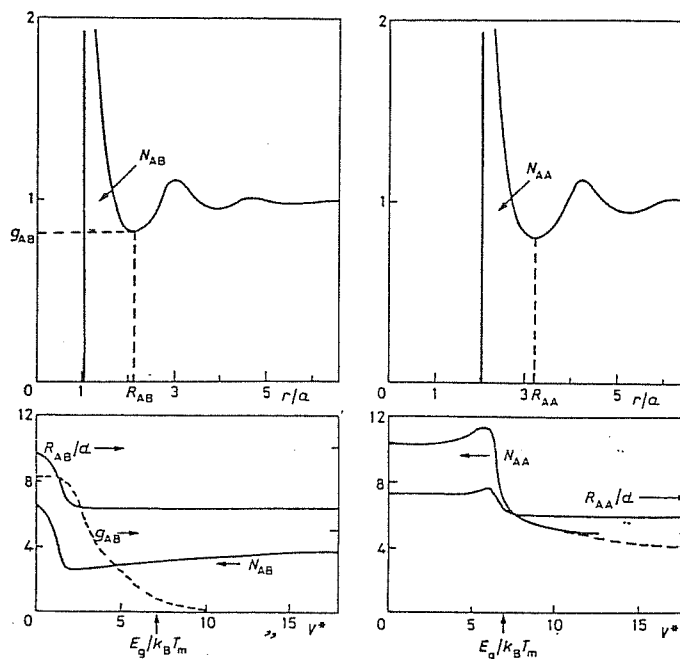


Figure 3.18: Schematic representation of bond particle localization and induced atomic structure changes with increasing coupling strength V^* . The top drawing show the atom-bond (left) and atom-atom (right) pair distribution functions at zero coupling strength. The evolution of special features of these functions, as defined in the top drawings, is shown at constant liquid density in the bottom drawings. The dashed portion in the curve for the atom-atom coordination number N_{AA} shows the effect of reducing the density from that of freezing germanium to that of compacted amorphous germanium. The value $V^* = E_g/k_B T_m$ is marked on the bottom axes. From Tosi, ref.[182].

approximately this value of the coupling strength, the atom-atom structure in the model starts to qualitatively resemble the observed liquid structure of germanium near freezing. In particular the value of N_{AA} in the model is approximately 7. It slowly decreases on supercooling, but a volume expansion of the order of the observed $\Delta v/v$ on freezing is necessary for N_{AA} to move towards the value 4. Thus, the unusual sign of the volume change on freezing is related to the need to accommodate the decrease in the atom-atom coordination number, which is frustrated at the relatively high liquid density.

Figure 3.19 (a) shows the evolution of liquid structure with increasing V^* at constant density. Upon incipient localization of B particles at $V^* \simeq 1 - 2$, the valley in $S_{AB}(k)$ is shifted towards the position of the main peak in $S_{BB}(k)$ and a weak prepeak in $S_{AB}(k)$ appears in correspondence with the main peak in $S_{AA}(k)$. Splitting of the $A - A$ first coordination shell into two shells at $V^* \simeq 7$ appears in $S_{AA}(k)$ as a new structure in the main peak, in the shape of a shoulder on its large- k side. A well known qualitative feature of the observed structure factor of liquid germanium is indeed the presence of such a shoulder near freezing, which reduces to an asymmetry in the peak shape at appreciably higher temperatures¹⁸⁴. The position of the shoulder

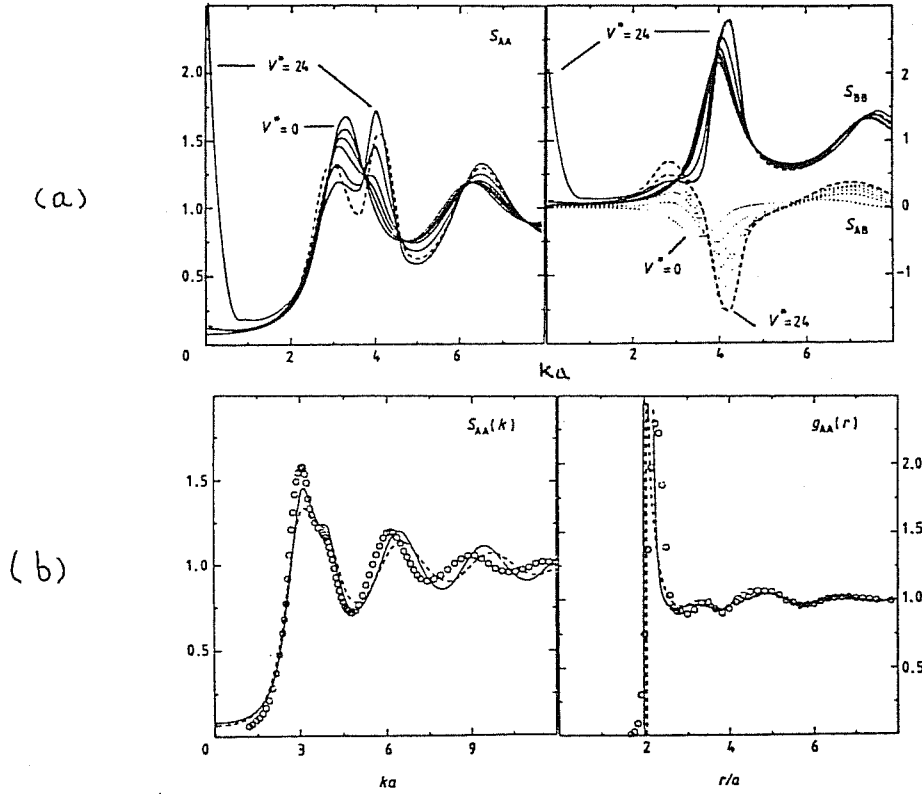


Figure 3.19: In (a) partial structure factors $S_{AA}(k)$ (left), $S_{AB}(k)$ (right, dotted curves) and $S_{BB}(k)$ (right, full curves) for the LAM in the HNC at series of values of V^* ($V^* = 0, 3, 5, 7.5, 14$ and 24 , the first and last values being marked in the figures). The broken lines gives the HMSA results for $V^* = 24$ and $b=1$. In (b) HNC partial structure factor $S_{AA}(k)$ (left) and pair distribution function $g_{AA}(r)$ (right) for the LAM at $V^* = 7.5$ (full curves) and for the BCM at $\Gamma = 24$ (broken lines). The circles reports X-ray diffraction data on liquid germanium at $T = 1253$ from Waseda and Suzuki [151]. From ref.[168]

in $S_{AA}(k)$ lies in correspondence with the main peak in $S_{BB}(k)$. On further increase in V^* the shoulder grows into a strong peak at essentially unshifted position, while the former main peak is reduced to a prepeak at progressively lower wave numbers.

While the above results are based on the HNC, Monte Carlo tests ¹⁶⁸ shows that this standard approximation in liquid-structure theory is surprisingly accurate even for the LAM up to $V^* \simeq 7$, above which accuracy in quantitative details is progressively being lost in the atom-atom correlations. The Monte Carlo runs requires large numbers of steps for equilibration and statistical accuracy and indeed indicate strong stickiness in the model when V^* is appreciably larger than 7.

In fig. 3.19 (b) we report the HNC results for $g_{AA}(r)$ and $S_{AA}(k)$ at $V^* = 7.5$, together with the liquid structure data on germanium near freezing from the X-ray diffraction experiments of Waseda and Suzuki ^{151,13}. For detailed discussion the reader should consult the original work of Ferrante and Tosi ¹⁶⁸.

3.3 Qualitative Discussion of Freezing of a Bond-Particle Model

In this section we are going to discuss equilibrium freezing of the bond particle model from a qualitative point of view ¹⁸³.

As shown in fig 3.20, the main peak in the atom-atom structure factor ($S_{AA}(k)$) in the model at $V^* = 7.5$ has the characteristic structure of a peak with a shoulder on its large- k side. These two features have been crudely separated in the figure by drawing a dotted line, to indicate that they could be viewed as a peak (the “shoulder”) with a prepeak superposed on it. We also notice in the same figure the main feature of the other partial structure factor of the model, namely the strong peak in the bond-bond structure factor, $S_{BB}(k)$, and the deep valley in the atom-bond structure factor, $S_{AB}(k)$, which are in superposition with the “shoulder” in this position. These features and their superposition with the “shoulder” show that in the liquid near freezing there is strong short-range order in the subsystem of bond particles and in their alternation with atoms in space.

The above observations suggest the following interpretation for the structural results shown in fig 3.20. A part of the patterns, consisting of the “shoulder” in $S_{AA}(k)$ (as separated by the dotted line), the valley in $S_{AB}(k)$ and the peak in $S_{BB}(k)$ plus all the structures at higher wave number, could in essence represent the form factor of relatively long-lived units consisting of an atom surrounded by bond particles and by first-neighbour atoms in approximate tetrahedral configuration. The remaining part of the structure, consisting just of the peak in $S_{AA}(k)$ (dashed line) after separation from the shoulder, would then represent the interference between the centers of such units. We shall for convenience refer below to this approximate partition of the partial structure factors as $S_{\alpha\beta}^{(1)}(k)$ and $S_{AA}^{(1)}(k)$ respectively.

The qualitative structural interpretation that we have suggested above is confirmed by the behaviour of the model on supercooling (i.e. on further increase of V^* at constant density ¹⁶⁸, as we have already discussed in the previous section. The shoulder in $S_{AA}(k)$ grows in intensity without shift in position, and indeed the whole of $S_{\alpha\beta}^{(1)}(k)$ just shows the usual sharpening and increase in peak intensity that are associated with a decrease in temperature. Instead, $S_{AA}^{(2)}(k)$ decreases in intensity and moves towards lower wave numbers, thus acquiring the nature of a FSDP (characteristic feature observed in glassy structures ¹⁴⁶, as discussed in section (3.1.1)). The position of such FSDP is very sensitive to the detailed shape of the second neighbour atom-atom coordination shell, showing that indeed this structural feature directly reflects the nature of the medium-range order in the disordered material. This behaviour of the model mimics observations on amorphous germanium ¹⁵⁰, which shows a main diffraction peak at a wave

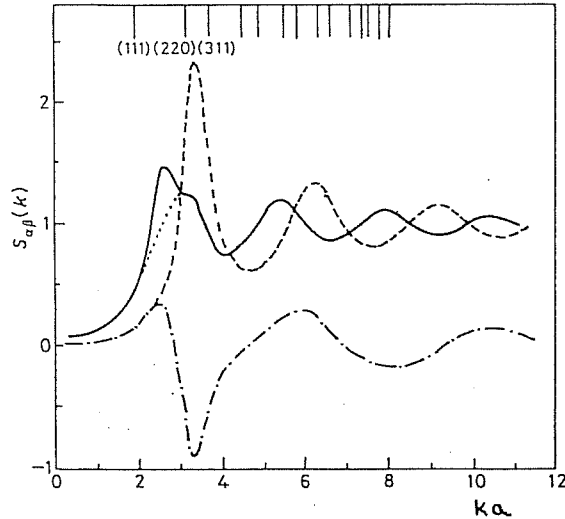


Figure 3.20: *Partial structure factors for a bond model of liquid germanium near freezing. The various curves show the atom atom (full line), atom bond (dashed dot) and bond bond (dashed) structure factors. The vertical bars at the top mark the location of the allowed Bragg reflections from the diamond structure.*

number in correspondence with the shoulder in the liquid structure factor and FSDP in approximate correspondence with the (111) star of reciprocal lattice vectors of the diamond structure. In this viewpoint, the low density of amorphous germanium allows a degree of medium-range order which is strongly reduced in the liquid phase, the latter being kept at a higher density by valence electrons in conducting states.

Using the above insight we discuss now what qualitative features may be expected for equilibrium freezing of the bond particle model and by implication of germanium. We refer first to our earlier discussion on the application of density functional theory to freezing of alkali halides and binary alloys (chapter 1, section 1.6.3). Within the same frame, the microscopic order parameters of the phase transition are the Fourier components ρ_{AG} and ρ_{BG} of the periodic single-particle densities for atoms (A) and bonds (B) in the crystal, \mathbf{G} denoting the reciprocal lattice vectors (RLV). The location of the allowed Bragg reflections from the diamond structure are superposed at the top of fig. 3.20 on the partial liquid structure factors of the of the bond-particle model. There clearly is good correspondence between the (220) and (311) RLV stars and the main features in $S_{\alpha\beta}^{(1)}(k)$. Thus the Fourier components of the periodic crystalline densities at the above RLV's describe "freezing of bonds" driven by tetrahedrally constrained attractions between ionic cores and valence electrons and leading to regular tetrahedra as components of the crystal. The connectivity that these tetrahedral units have in the diamond structure is to be described by the microscopic order parameters associated with the (111) star of RLV. We infer this from the above interpretation of $S_{AA}^{(2)}(k)$ and from the fact that the FSDP at wave number in correspondence with (111) RLV star is well developed in

amorphous germanium. However, formation of such connectivity in the liquid is frustrated by its relatively high density. Hence, crystallization of the liquid into the diamond structure requires volume expansion. On the contrary, crystallization of compacted amorphous germanium is accompanied by volume contraction. In section 4 of this chapter we shall report our detailed results on the freezing of a bond particle model within the density wave theory of freezing, whereas in section 5 we shall discuss our evaluation of freezing for a liquid having the structure of amorphous germanium. In the rest of this section we shall try to give some simple calculation in support of the inferences that we have just made.

The main order parameters of the phase transition, in addition to the percentual density difference $\eta = (\rho_s - \rho_l)/\rho_l$ between solid and liquid at coexistence, are thus expected to be: a) charge density waves (opposite signs for ρ_{AG} and ρ_{BG}) at the (220) and (311) stars, and b) number density waves (equal signs for ρ_{AG} and ρ_{BG}) at the (111) star. For an estimate we proceed within the framework of the density wave theory of freezing, as extended to two-component systems by March and Tosi⁹¹. We recall that the theory yields a set of nonlinear equilibrium equations for the order parameters and an equation expressing equality of the grand thermodynamic potential in the liquid and in the crystal at coexistence. These equations involve knowledge of the isothermal compressibility K_T and of the Ornstein-Zernike direct correlation functions $\tilde{c}_{\alpha\beta}(\mathbf{G})$ in the liquid at wave numbers corresponding to the various stars of RLV. The relevant values of $\tilde{c}_{\alpha\beta}(\mathbf{G})$ are obtained from partial structure factors shown in fig. 3.20 through use of the Pearson-Rushbrook relations and are tabulated in table (3.3). We estimate a value of $K_T \simeq 2.5 \times 10^{-12} \text{cm}^2/\text{dyn}$ for molten germanium, in the apparent lack of experimental data, by estimating the sound velocity u in the liquid from an empirical relation between u and the atomic mass and molar volume¹⁸⁵, which is very well satisfied by the measured values of the sound velocity in molten silicon and tin. This estimate is in good agreement with measured value from sound velocity in molten germanium by Glasove¹⁸⁶.

For an order-of-magnitude estimate of the ratio ρ_{AG}/ρ_{BG} for the microscopic order parameters at the various RLV stars, one may look at the corresponding equilibrium equations after linearization. These give⁹¹

$$\rho_{AG}/\rho_{BG} \simeq \frac{\sqrt{2}\tilde{c}_{AB}(\mathbf{G})}{(\rho_l/\rho_s) - \tilde{c}_{AA}(\mathbf{G})} \simeq \frac{(\rho_l/\rho_s) - \tilde{c}_{BB}(\mathbf{G})}{\tilde{c}_{AB}(\mathbf{G})/\sqrt{2}} \quad (3.3.1)$$

where ρ_{AG} and ρ_{BG} are expressed in units of the respective average partial densities ρ_A and ρ_B (with $\rho_A = \rho_B = n$, n being the atom number density). Using the values of the Ornstein-Zernike functions in table (3.3), it is easily seen that the above ratio is positive at the (111) star and negative at the (220) and (311) stars. The preceding discussion of the phase transition in terms of number density and charge density waves is therefore confirmed at

	AA	AB	BB
$\bar{c}_{\alpha\beta}(111)$	- 2.20	2.50	- 3.20
$\bar{c}_{\alpha\beta}(220)$	0.13	- 0.22	0.24
$\bar{c}_{\alpha\beta}(311)$	- 0.43	- 0.31	0.24

Table 3.3: *Selected values of the direct correlation functions in the bond particle model for molten germanium at $V^* = 7.5$*

this level of approximation. We shall see below (end of section 3.4.2) that the above qualitative picture is also consistent with a volume expansion across the transition from liquid to solid.

3.4 Density Wave Theory of Freezing for a Bond-Particle Model

In the previous sections we have described the bond particle model as adapted to the liquid structure of elemental semiconductors (in particular germanium) and given a simple qualitative picture of the freezing process in such a liquid. Within the framework of the density wave theory of freezing of two-component fluids, as developed for alkali halides and binary alloys by March and Tosi⁹² (see chapter 1, section 1.6.3), we are going to evaluate in this section the relation between liquid structure in the bond-particle model and crystallization of elemental semiconductors. We start with brief discussion of the partial structure factors and partial correlation functions for binary fluids.

3.4.1 Pearson - Rushbrooke Relations and Bahatia-Thornton Structure Factors for Two Component Systems

The structure of a binary fluid mixture of A and B particles requires for its description three radial distribution functions ($g_{AA}(r)$, $g_{BB}(r)$ and $g_{AB}(r)$, say). Pearson and Rushbrooke¹⁸⁷ introduced relations between the partial distribution functions $g_{\alpha\beta}(r)$ and the partial direct correlation functions $c_{\alpha\beta}(r)$ generalizing the Ornstein-Zernike relation. These are (for $\alpha, \beta = 1, 2$)

$$h_{\alpha\beta}(r) = c_{\alpha\beta}(r) + \sum_{\gamma} \rho_{\gamma} \int d\mathbf{r}' c_{\alpha\beta}(\mathbf{r} - \mathbf{r}') h_{\alpha\beta}(r') \quad (3.4.1)$$

where $h_{\alpha\beta} = g_{\alpha\beta} - 1$, and ρ_γ 's are the number densities of species γ ($\rho_\gamma = \langle N_\gamma \rangle / V$). At the same time the partial structure factor for a two-component system are defined by

$$S_{\alpha\beta}(k) = \delta_{\alpha\beta} + 4\pi(\rho_\alpha\rho_\beta)^{1/2} \int_0^\infty [g_{\alpha\beta}(r) - 1] \frac{\sin kr}{kr} r^2 dr \quad . \quad (3.4.2)$$

Substituting eqn.(3.4.1) in eqn.(3.4.2), one gets

$$\begin{aligned} S_{11}(k) &= \frac{1 - \bar{c}_{22}(k)}{(1 - \bar{c}_{11}(k))(1 - \bar{c}_{22}(k)) - \bar{c}_{12}^2(k)} \\ S_{22}(k) &= \frac{1 - \bar{c}_{11}(k)}{(1 - \bar{c}_{11}(k))(1 - \bar{c}_{22}(k)) - \bar{c}_{12}^2(k)} \\ S_{12}(k) &= \frac{\bar{c}_{12}(k)}{(1 - \bar{c}_{11}(k))(1 - \bar{c}_{22}(k)) - \bar{c}_{12}^2(k)} \end{aligned} \quad (3.4. 3)$$

where $\bar{c}_{\alpha\beta}(k)$ are the Fourier transform of the direct correlation function $c_{\alpha\beta}(r)$.

Bahatia and Thornton¹⁸⁸ have shown that the scattering function for a binary structure factors $S_{NN}(\mathbf{k})$, $S_{NC}(\mathbf{k})$ and $S_{CC}(\mathbf{k})$ which are defined as

$$\begin{aligned} S_{NN}(\mathbf{k}) &= N^{-1} \langle \rho(\mathbf{k})\rho(-\mathbf{k}) \rangle \\ S_{CC}(\mathbf{k}) &= N \langle \Delta(\mathbf{k})\Delta(-\mathbf{k}) \rangle \\ S_{NC}(\mathbf{k}) &= Re \langle \rho(\mathbf{k})\Delta(-\mathbf{k}) \rangle \quad , \end{aligned} \quad (3.4. 4)$$

where $\rho(\mathbf{k})$ is the Fourier transform of the total singlet density $\rho(\mathbf{r}) = \rho_1(\mathbf{r}) + \rho_2(\mathbf{r})$ and $\Delta(\mathbf{k})$ is the Fourier transform of a density difference $\Delta(\mathbf{r})$ weighted with the concentrations c_1 and $c_2 = 1 - c_1$, namely

$$\Delta(\mathbf{r}) = c_2\rho_1(\mathbf{r}) - c_1\rho_2(\mathbf{r}) \quad . \quad (3.4.5)$$

The structure factor (3.4.4) are linear combinations of the $S_{\alpha\beta}(k)$ in eqn.(3.4.2), and appropriate Ornstein-Zernike function can be correspondingly defined. In particular, in the long-wavelength limit $\mathbf{k} \rightarrow 0$ one obtains

$$\begin{aligned} S_{CC}(0) &= Nk_B T / (\delta^2 G / \delta c^2)_{T,P,N} \\ S_{NN}(0) &= (N/V)k_B T K_T + \delta^2 S_{CC}(0) \\ S_{NC}(0) &= -\delta S_{CC}(0) \quad , \end{aligned} \quad (3.4. 6)$$

where K_T is the isothermal compressibility, G is the Gibbs free energy and δ is a dilation factor defined by

$$\delta = \frac{v_1 - v_2}{c_1 v_1 + c_2 v_2} = \frac{N}{V}(v_1 - v_2) \quad , \quad (3.4.7)$$

where v_1 and v_2 are the partial molar volumes, per atom of the two species. If the partial molar volumes v_1 and v_2 are equal then $S_{NC}(0) = 0$ and $S_{NN}(0)$ has the form

$$S_{NN}(0) = (N/V)k_B T K_T \quad . \quad (3.4.8)$$

In fact, in most alloys δ is very small and considering $S_{NC}(0) \simeq 0$ is a reasonable approximation. From eqn.(3.4.4) it is clear that in the long-wave length limit $S_{NN}(0)$ and $S_{NC}(0)$ represent, respectively, the mean square fluctuation in the particle number and in concentration and $S_{NC}(0)$ is the correlation between these two fluctuations.

In the case of ionic systems it is convenient to work with the charge density $Q(\mathbf{r}) = \rho_1(\mathbf{r}) - \rho_2(\mathbf{r})$ that replaces the $\Delta(\mathbf{r})$, as we have already discussed (see chapter 1, section 1.6.3).

3.4.2 Density Wave Theory of Freezing for a Two Component System

We turn now to the freezing of an elemental semiconductor regarded as two-component system of atoms and bond particles. Following the approach already presented summarily in section 1.6.3, the theory is formulated in terms of the thermodynamic potential Ω as a functional of the single particle densities $\rho_A(\mathbf{r})$ and $\rho_B(\mathbf{r})$. A set of coupled equilibrium equations for these densities are obtained by requiring that Ω be a minimum. For coexistence between liquid (l) and solid (s) phases, the difference $\Delta\Omega = \Omega_s - \Omega_l$ must vanish. The equations involve the knowledge of the isothermal compressibility K_T and of the partial Ornstein-Zernike direct correlation functions in the liquid at wave numbers corresponding to the various stars of RLV.

The equations for the density profiles (see eqn.(1.6.8)) are

$$\frac{\nabla \rho_i(\mathbf{r})}{\rho_i(\mathbf{r})} = \sum_{j=A,B} \int d\tau c_{ij}(\mathbf{r}_1, \mathbf{r}) \nabla \rho_j(\mathbf{r}) \quad (i = A, B). \quad (3.4.9)$$

Following the work of Lovett⁴⁰, one can integrate eqn.(3.4.9) under the assumption that $c_{ij}(\mathbf{r}_1, \mathbf{r})$ depends only on $|\mathbf{r}_1 - \mathbf{r}|$ as in a liquid. The result is

$$\ln \rho_i(\mathbf{r}_1) = \sum_{j=A,B} \int d\tau c_{ij}(|\mathbf{r}_1 - \mathbf{r}|) \rho_j(\mathbf{r}) + \mu_i \quad , \quad (3.4.10)$$

where μ_i is a constant of integration. It has shown that ⁹¹, given the partial liquid direct correlation functions c_{ij} , this equation exhibits a periodic solution $\rho_{is}(\mathbf{r})$ for the solid phase in coexistence with the homogeneous solution ρ_{il} , when the constant μ_i is the same in the two phases. Then the difference between eqn.(3.4.10) for periodic and homogeneous singlet densities is

$$\ln \left(\frac{\rho_{is}(\mathbf{r}_1)}{\rho_{il}} \right) = \sum_{j=A,B} \int d\tau c_{ij}(|\mathbf{r}_1 - \mathbf{r}|) [\rho_{js}(\mathbf{r}) - \rho_{jl}] \quad (3.4.11)$$

as reported in section (1.6.3) from the truncated cluster expansion. The corresponding equation for the difference $\Delta\Omega$ in grand potentials is

$$\begin{aligned} \frac{\Delta\Omega}{k_B T} &= \sum_{j=A,B} \int d\tau \left(\rho_{is}(\mathbf{r}) \ln \left[\frac{\rho_{is}(\mathbf{r}_1)}{\rho_{il}} \right] - [\rho_{is}(\mathbf{r}) - \rho_{il}] \right) \\ &- \frac{1}{2} \sum_{i,j=A,B} \int \int d\tau_1 d\tau_2 [\rho_{is}(\mathbf{r}_1) - \rho_{il}] c_{ij}(|\mathbf{r}_1 - \mathbf{r}_2|) [\rho_{js}(\mathbf{r}_2) - \rho_{jl}] \end{aligned} \quad (3.4.12)$$

Varying $\Delta\Omega$ with respect to the periodic singlet densities, it is readily verified that eqn.(3.4.12) leads back to eqn.(3.4.11) as the Euler equation of a variational problem. Next if we substitute in eqn.(3.4.12) the term $\ln[\rho_{is}(\mathbf{r})/\rho_{il}]$ from eqn.(3.4.11) we have

$$\begin{aligned} \frac{\Delta\Omega}{k_B T} &= - \sum_{j=A,B} \int d\tau [\rho_{is}(\mathbf{r}) - \rho_{il}] + \\ &+ \frac{1}{2} \sum_{i,j=A,B} \int \int d\tau_1 d\tau_2 [\rho_{is}(\mathbf{r}_1) + \rho_{il}] c_{ij}(|\mathbf{r}_1 - \mathbf{r}_2|) [\rho_{js}(\mathbf{r}_2) - \rho_{jl}] \end{aligned} \quad (3.4.13)$$

(see eqn.(1.6.10)). This quantity vanishes at coexistence, at which the periodic singlet densities are to be obtained from eqn.(3.4.11).

We introduce next the Fourier expansions of the periodic singlet densities by

$$\rho_{is}(\mathbf{r}) = \rho_{il} \left(1 + \eta + \sum_{\mathbf{G} \neq 0} \rho_{i\mathbf{G}} \exp[i\mathbf{G} \cdot \mathbf{r}] \right) \quad (i = A, B) \quad , \quad (3.4.14)$$

where $\eta = (\rho_s - \rho_l)/\rho_l$ is the fractional density change. With the further definition of the Fourier transform of the direct correlation functions,

$$c_{ij}(r) = \frac{1}{V \sqrt{\rho_{il} \rho_{jl}}} \sum_{\mathbf{k}} \bar{c}_{ij}(\mathbf{k}) \exp[i\mathbf{k} \cdot \mathbf{r}] \quad (i, j = A, B) \quad , \quad (3.4.15)$$

we have the equilibrium conditions for the $\mathbf{G} \neq 0$ components of the densities,

$$\int d\tau \ln\left\{1 + \frac{\rho_{il}}{\rho_{is}} \sum_{\mathbf{G}' \neq 0} \rho_{i\mathbf{G}'} \exp[i\mathbf{G}' \cdot \mathbf{r}]\right\} \exp[-i\mathbf{G} \cdot \mathbf{r}] = V \sum_{i,j=A,B} \frac{\rho_{jl}}{\sqrt{\rho_{il}\rho_{jl}}} \rho_{j\mathbf{G}} \tilde{c}_{ij}(\mathbf{G}) \quad (3.4.16)$$

After linearization of the left-hand side and integration we get eqn.(3.3.1), that was used in section (3.3.3) for a qualitative discussion of the ratios $\rho_{A\mathbf{G}}/\rho_{B\mathbf{G}}$.

The corresponding expression for $\Delta\Omega$ is

$$\begin{aligned} \frac{\Delta\Omega}{k_B T} = & - (\rho_s - \rho_l)V + \frac{V}{2} \left(\frac{\rho_s^2}{\rho_l^2} - 1 \right) \sum_{i,j=A,B} \sqrt{\rho_{il}\rho_{jl}} \tilde{c}_{ij}(0) \\ & + \frac{V}{2} \sum_{i,j=A,B} \sum_{\mathbf{G} \neq 0} \sqrt{\rho_{il}\rho_{jl}} \tilde{c}_{ij}(\mathbf{G}) \rho_{i\mathbf{G}} \rho_{j\mathbf{G}} \end{aligned} \quad (3.4.17)$$

The particular combination of $\tilde{c}_{ij}(0)$ in eqn.(3.4.17) is related to the isothermal compressibility by

$$1 - \sum_{i,j=A,B} \frac{\sqrt{\rho_{il}\rho_{jl}}}{\rho_l} \tilde{c}_{ij}(0) = \frac{1}{\rho_l k_B T K_T} \quad (3.4.18)$$

The equality of the grand potentials in the two phases ($(\Delta\Omega/Nk_B T) = 0$) with $\rho_A = \rho_B/2 = n$ yields

$$\frac{\eta}{nk_B T_m K_T} = \frac{1}{2} \sum_{\mathbf{G} \neq 0} [\tilde{c}_{AA}(\mathbf{G})\rho_{A\mathbf{G}}^2 + 2\sqrt{2}\tilde{c}_{AB}(\mathbf{G})\rho_{A\mathbf{G}}\rho_{B\mathbf{G}} + 2\tilde{c}_{BB}(\mathbf{G})\rho_{B\mathbf{G}}^2] \quad (3.4.19)$$

The measured value of η for germanium is -5% and hence the left-hand side of eqn.(3.4.19) is of order -2.4 . Then, given the signs of the corresponding Ornstein-Zernike functions in table (3.3), the contributions to the sum of the right-hand side from charge density waves at the (220) and (311) stars are positive. On the other hand, the signs and magnitudes of the Ornstein-Zernike functions at the (111) star in table (3.3) show that the corresponding contribution to the right-hand side of eqn.(3.4.19) is large and negative. A balance between these contributions, which is obviously very delicate, will have to lead to the indicated negative value for the left-hand side.

3.4.3 Results and Discussion

Figure 3.21 shows the diamond-type crystal structure of germanium after decoration of the interatomic bonds by bond particles (this is actually known

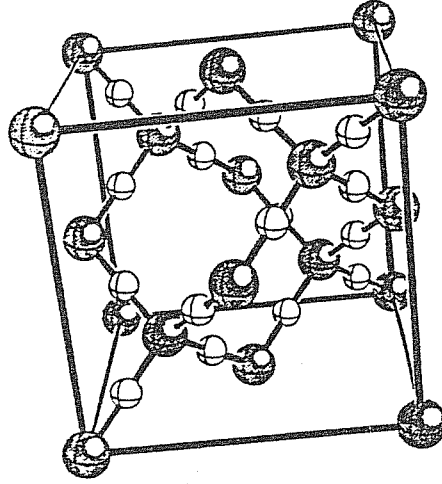


Figure 3.21: Cubic cell of crystalline germanium showing decoration of interatomic bonds by bond particles. From ref.[183]

in crystallography as the ideal β -cristobalite structure for SiO_2 ¹⁸⁹). This figure is helpful in constructing the Fourier transforms of the single-particle densities for atoms and bonds, as we do immediately below. Bearing in mind that the structure in fig.(3.21) can be viewed as formed by a multiplicity of fcc sublattices (two such sublattices for atoms and four for bonds), we shall express the $\rho_{i\mathbf{G}}$'s ($i = A, B$) as products of density components appropriate to an fcc sublattice ($n_{i\mathbf{G}}$ say, with $i = A, B$) times phase factors containing the phase relation between the various sublattices.

Explicitly, we write

$$\rho_{As}(\mathbf{r}) = \rho_{Al}(1 + \eta \sum_{\mathbf{G} \neq 0} n_{AG} \exp[i\mathbf{G} \cdot (\mathbf{r} + \sum_{n=1}^2 \mathbf{h}_n^{(A)})]) \quad (3.4.20)$$

$$\rho_{Bs}(\mathbf{r}) = \rho_{Bl}(1 + \eta \sum_{\mathbf{G} \neq 0} n_{BG} \exp[i\mathbf{G} \cdot (\mathbf{r} + \sum_{n=1}^4 \mathbf{h}_n^{(B)})]) \quad (3.4.21)$$

where $\mathbf{h}_n^{(A)}$ are the vector positions of the atoms in the unit cell ($\mathbf{h}_1^{(A)} = (0, 0, 0)a$, $\mathbf{h}_2^{(A)} = (1/4, 1/4, 1/4)a$) and $\mathbf{h}_n^{(B)}$ are the vector position of the bonds ($\mathbf{h}^{(B)} = (1/8, 3/8, 3/8)a; (3/8, 1/8, 3/8)a; (3/8, 3/8, 1/8)a$), a being the side of the cube. Specifically we have for the contribution to the density profiles coming from the first three stars of RLV's the following expressions:

$$\begin{aligned} \rho_A^{(111)}(\mathbf{r}) &= \rho_{Al}(1 + \eta + 8n_{AG}[\cos x \cos y \cos z - \sin x \sin y \sin z]) \\ \rho_B^{(111)}(\mathbf{r}) &= \rho_{Bl}(1 + \eta + 8\sqrt{2}n_{BG}[\cos x \cos y \cos z - \\ &\quad - \sin x \sin y \sin z]) \end{aligned} \quad (3.4.22)$$

$$\begin{aligned} \rho_A^{(220)}(\mathbf{r}) &= \rho_{Al}(1 + \eta + 8n_{AG}[\cos 2x \cos 2y + \cos 2x \cos 2z + \cos 2y \cos 2z]) \\ \rho_B^{(220)}(\mathbf{r}) &= \rho_{Bl}(1 + \eta) \end{aligned} \quad (3.4.23)$$

$$\begin{aligned}
\rho_A^{(311)}(\mathbf{r}) &= \rho_{Al}(1 + \eta + n_{AG}[\cos 3x \cos y \cos z + \cos x \cos 3y \cos z \\
&\quad + \cos x \cos y \cos 3z + \sin 3x \sin y \sin z \\
&\quad + \sin x \sin 3y \sin z + \sin x \sin y \sin 3z]) \\
\rho_B^{(311)}(\mathbf{r}) &= \rho_{Bl}(1 + \eta - 8\sqrt{2}n_{BG}[\cos 3x \cos y \cos z + \cos x \cos 3y \cos z \\
&\quad + \cos x \cos y \cos 3z + \sin 3x \sin y \sin z \\
&\quad + \sin x \sin 3y \sin z + \sin x \sin y \sin 3z]) \quad (3.4. 24)
\end{aligned}$$

It is instead convenient to reexpress $\Delta\Omega$ in terms of the total density $\rho(\mathbf{r}) = \rho_A(\mathbf{r}) + \rho_B(\mathbf{r})$ and the difference density $\Delta(\mathbf{r})$ weighted with the concentrations (see eqn.(3.4.5)). We introduce first the density-concentration correlation functions $c_{NN}(r), c_{NC}(r)$ and $c_{CC}(r)$ as in ref.[93] with the concentration $c_1 = 1/3$ for atoms and $c_2 = 2/3$ for bonds:

$$\begin{aligned}
c_{NN}(r) &= c_1 c_{AA}(r) + 2c_1 c_2 c_{AB}(r) + c_2^2 c_{BB}(r) \\
c_{NC}(r) &= c_1 c_2 [c_1 c_{AA}(r) + (c_1 - c_2) c_{AB}(r) - c_2 c_{BB}(r)] \\
c_{CC}(r) &= c_1^2 c_2^2 [c_{AA}(r) - c_{AB}(r) + c_{BB}(r)] \quad . \quad (3.4. 25)
\end{aligned}$$

In terms of these quantities we have

$$\begin{aligned}
\frac{\Delta\Omega}{k_B T} &= - \int d\mathbf{r} [\rho(\mathbf{r}) - \rho_l] + \frac{1}{2} \int \int d\mathbf{r}_1 d\mathbf{r}_2 \{ [\rho(\mathbf{r}_1) + \rho_l] c_{NN}(|\mathbf{r}_1 - \mathbf{r}_2|) [\rho(\mathbf{r}_2) - \rho_l] \\
&\quad + \frac{1}{c_1 c_2} [\rho(\mathbf{r}_1) + \rho_l] c_{NC}(|\mathbf{r}_1 - \mathbf{r}_2|) \Delta(\mathbf{r}_2) \\
&\quad + \frac{1}{c_1 c_2} \Delta(\mathbf{r}_1) c_{NC}(|\mathbf{r}_1 - \mathbf{r}_2|) [\rho(\mathbf{r}_2) - \rho_l] \\
&\quad + \frac{1}{c_1^2 c_2^2} \Delta(\mathbf{r}_1) c_{CC}(|\mathbf{r}_1 - \mathbf{r}_2|) \Delta(\mathbf{r}_2) \} \quad (3.4. 26)
\end{aligned}$$

The equations that follow from eqn.(3.4.11) and (3.4.25), and that we have actually used in our calculations, are finally as follows:

$$\begin{aligned}
1 + \eta &= \frac{1}{2} \{ \exp[\sum_{j=A,B} \alpha_j^0 \eta] V^{-1} \int d\mathbf{r} \exp[\sum_{j=A,B} D_j(\mathbf{r})] + \\
&\quad + \exp[\sum_{i=A,B} \alpha_i^0 \eta] V^{-1} \int d\mathbf{r} \exp[\sum_{i=A,B} D_i(\mathbf{r})] \} \quad (3.4. 27)
\end{aligned}$$

$$n_{iG} H_i = \exp[\sum_{j=A,B} \alpha_j^0 \eta] V^{-1} \int d\mathbf{r} \exp[-i\mathbf{G} \cdot \mathbf{r} + \sum_{j=A,B} D_j(\mathbf{r})] \quad . \quad (3.4.28)$$

Here, we have defined the following quantities:

$$\alpha_j^0 = \frac{\rho_{jl}}{\sqrt{\rho_{il}\rho_{jl}}} \tilde{c}_{ij}(0) \quad (3.4.29)$$

$$\alpha_j(\mathbf{G}) = \frac{\rho_{jl}}{\sqrt{\rho_{il}\rho_{jl}}} \tilde{c}_{ij}(\mathbf{G}) \quad (3.4.30)$$

$$D_j(\mathbf{r}) = \sum_{\mathbf{G} \neq 0} \alpha_j(\mathbf{G}) n_{j\mathbf{G}} H_j \exp[i\mathbf{G} \cdot \mathbf{r}] \quad (3.4.31)$$

and

$$H_j = \sum_n \exp[i\mathbf{G} \cdot \mathbf{h}_n^{(j)}] \quad (3.4.32)$$

We have included in our calculations the first three stars of RLV, the relevant values of the $\tilde{c}_{\alpha\beta}(\mathbf{G})$ being obtained directly from the partial structure factors shown in fig.(3.20) through use of the Pearson-Rushbrooke relations (see table (3.3)). On the other hand, we have tried to adapt the behaviour of the model in the long-wavelength limit to real *Ge* by taking the isothermal compressibility from measurements on liquid *Ge* ($K_T = 2.5 \times 10^{-12} \text{ cm}^2/\text{dyn}^{186}$). This determines $c_{NN}(0)$ according to eqn.(3.4.18) and equivalently a linear combination of α_A^0 and α_B^0 through

$$\frac{1}{3}\alpha_A^0 + \frac{2}{3}\alpha_B^0 = 1 - \frac{1}{\rho_l k_B T K_T} \quad (3.4.33)$$

We are also faced with the need of having separate values of α_A^0 and α_B^0 . In this connection, the model indicates that the dominant contribution to eqn.(3.4.33) comes from α_B^0 . The specific choice of α_A^0 should therefore be essentially unimportant, we estimate $\alpha_A^0 \simeq 2.7$ from the HNC solution of the bond particle model. Nevertheless, throughout our calculations we have not been able to satisfy the equilibrium equation for η (eqn.(3.4.27)) with the required accuracy. We have therefore discarded this equation and examined the solution of the remaining equations with the assumed value $\eta = -0.05$, which corresponds to the volume change of real *Ge* on freezing.

In our calculations the density profiles $\rho_{is}(\mathbf{r})$ of the solid phase are approximately represented by superpositions of Gaussians centered at the various lattice sites, with widths that are to be calculated variationally (one Gaussian for atoms and one for bonds on an fcc sublattice). We first include the order parameters at the (111) star and at the (220) star and find the two Gaussian widths that approximately satisfy the four equilibrium equations at these two stars. At this point we go to the coexistence condition $(\Delta\Omega/Nk_B T) = 0$ and find that this is not satisfied, $\Delta\Omega$ being of the order of few $k_B T$. Clearly, we should reevaluate the structure at a different value of the coupling strength $V/k_B T$, in order to determine the coexistence point. We have not carried out such a massive program of numerical structure

evaluation, but simply examined what would be the change in the most sensitive structural parameter, i.e. $\bar{c}_{BB}(111)$, that would be needed to obtain phase coexistence. A moderate increase in the magnitude of this quantity relative to the value in table (3.3), to $\bar{c}_{BB}(111) \simeq -4$, would satisfy the coexistence condition. The result of this calculations is an estimate of the Gaussian width, which (according to the definitions given in section 2.5.1), turn out to be $\alpha_A^{-1/2} \simeq 0.4\text{\AA}$ and $\alpha_B^{-1/2} \simeq 1.1\text{\AA}$. These values correspond to Lindemann ratios (see section 2.5.1) having the values

$$L_A \simeq 0.16 \quad , \quad L_B \simeq 0.55 \quad . \quad (3.4.34)$$

The estimated value of the Lindemann ratio for atoms is therefore of the same order of magnitude as for simple fcc or bcc lattices, whereas the localization of the bond particles in the hot solid at melting is appreciably more spread out. In addition, from the phase factors between the various sublattices it follows that order in the (111) star, in the Gaussian approximation, is described by a density wave, whereas the order at the (220) star is just an atom density wave.

We turn next to include the (311) star. The main features of the calculations and their results remain as indicated just above, except that the magnitude of $\bar{c}_{BB}(111)$ should be decreased to $\bar{c}_{BB}(111) \simeq -2$, in order to satisfy the coexistence condition. An illustration of the numerical solution for $\bar{c}_{BB}(111) = -3$ is given in fig. 3.22. The width of the Gaussians for bonds is essentially unchanged, while that for atoms is found to be $\alpha_A^{-1/2} \simeq 0.7\text{\AA}$, corresponding to a rather large value for the Lindemann ratio, $L_A \simeq 0.33$. Again, the phase factors between the various sublattices are such that order in the (311) star is described in the Gaussian approximation as a charge density wave.

In conclusion, the microscopic liquid structure of the bond particle model at coupling strength $V^* \simeq 7.5$, where the atom-atom structure is in approximated agreement with the observed liquid structure of *Ge*, is broadly consistent with a freezing mechanism in which density waves at the (111) star, atomic density waves at the (220) star and charge density waves at the (311) star are spontaneously generated, as well as with the fact that the volume change on freezing is negative. In more pictorial terms, one is led to view the freezing of *Ge* as driven by the freezing of the bonds (i.e. by the metal-to-semiconductor transition in the system of valence electrons) in a tetrahedral bond configuration inducing local tetrahedral interatomic coordination. The long-range order of the crystal is associated with relative order in such tetrahedral units, forming a very open structure which requires volume dilation. However, the estimated Lindemann ratios that emerge from our calculations are rather large, at least by comparison with typical values for monatomic systems crystallizing in fcc or bcc Bravais structures.

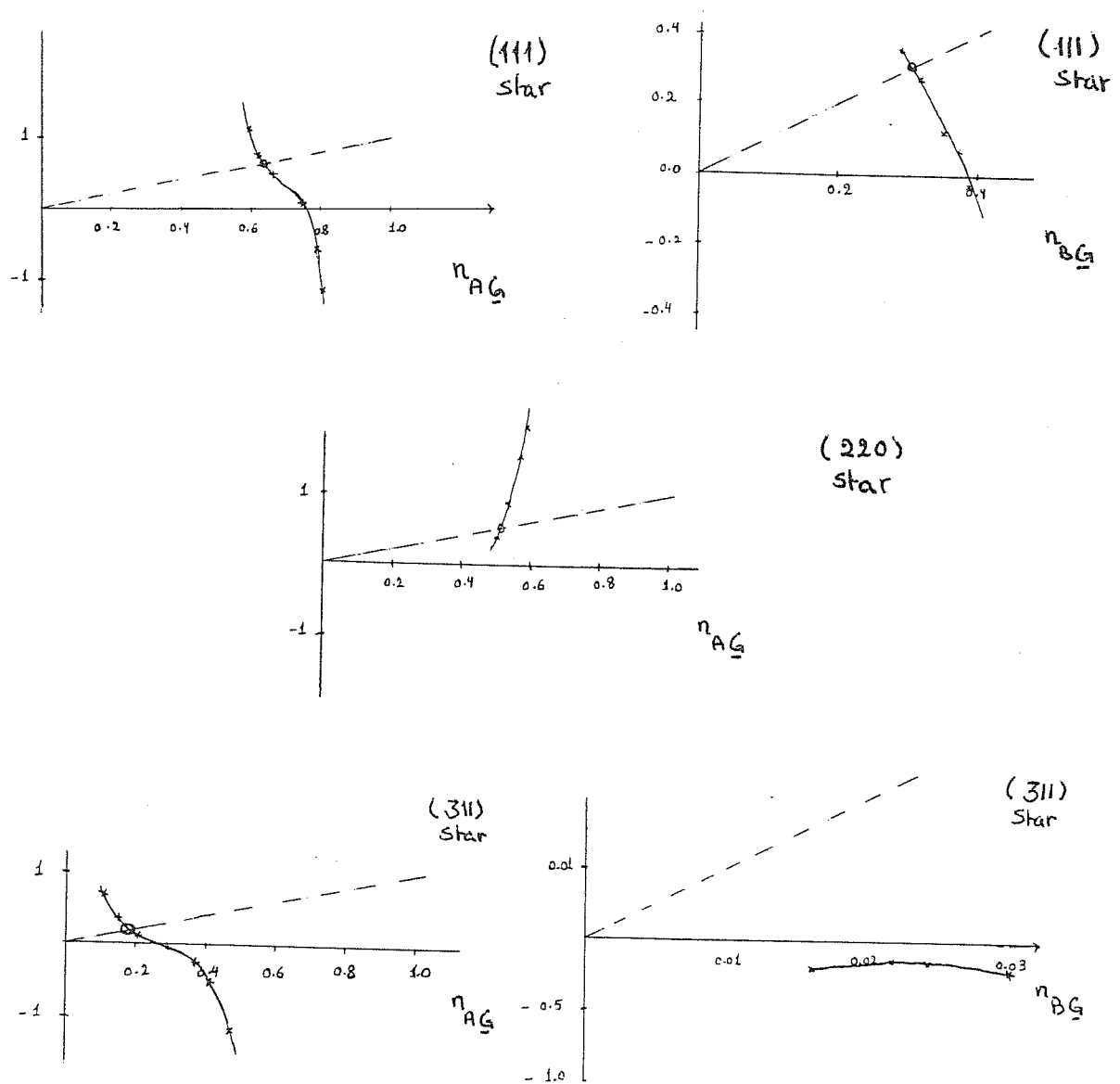


Figure 3.22: An illustration of the numerical solution for $\bar{c}_{BB}(111) = -3$ for the different order parameters $n_{iG}; i = A, B$. The y-axis and the x-axis represents, respectively the left- and right-hand side of the equilibrium eqn.(3.4.28). The dashed lines indicate when both sides of the equation are equal. Full curves are the values of the right-hand side. The crossing point represents the solution of the equilibrium eqn.(3.4.28). In the case with n_{BG} at the (311) star it was impossible to reach the solution.

3.5 Evaluation of Freezing for a Liquid Having the Structure of Amorphous Germanium

In the preceding sections we have discussed qualitatively and numerically the freezing of a bond-particle model applied in a special case to germanium. We have seen that the microscopic order parameters associated with the (220) and (311) star are responsible for “freezing of bonds” and leading to regular tetrahedra as components of the crystal, whereas the connectivity that these tetrahedral units have in the diamond structure is related to the microscopic order parameters associated with the (111) star. In this section, we are going to evaluate the freezing of a one-component liquid having the structure of amorphous germanium. This evaluation is interesting in relation to the role that we have attributed to the (111) star, when one recalls that the FSDP in the diffraction pattern of amorphous germanium lies in correspondence with this RLV star.

We should comment on the reason why we consider in the present context only the atomic component and omit consideration of the atom-bond and bond-bond partial structure factors. The latter have been evaluated by Stenhouse et al ¹⁹⁰ for amorphous *Si* from a continuous random network model of the atomic pair structure. Their calculation shows that both $S_{AB}(k)$ and $S_{BB}(k)$ show a prominent peak in correspondence with the FSDP in $S_{AA}(k)$, as well as the main features associated with ‘relative’ ordering of atoms and bonds (a valley in $S_{AB}(k)$ and a peak in $S_{BB}(k)$ in approximate correspondence with the main peak in $S_{AA}(k)$). Thus, consistently with the semiconducting nature of the amorphous material, the bonds are already frozen in it and can only follow the atomic component as it crystallizes. We therefore expect that an explicit inclusion of the bonds in the present calculation would not alter its conclusions, except that it would further stabilize the crystalline state relative to the disordered state.

The microscopic order parameters of the phase transition are the Fourier components $\rho_{\mathbf{G}}$ ’s of the periodic single-particle density in the crystal. The set of equilibrium equations needed to locate the phase transition have already been given in chapter 2, i.e. the set of equations (2.4.13) for the microscopic parameters $\rho_{\mathbf{G}}$, eqn.(2.4.14) for the volume change and eqn.(2.4.15) to assure equality of the grand potential in the two phases. These equations involve the knowledge of the isothermal compressibility K_T and the Ornstein-Zernike direct correlation function $\tilde{c}(\mathbf{G})$ in the fluid at wave numbers corresponding to the various stars of RLV. The relevant values of the $\tilde{c}(\mathbf{G})$ (see table (3.4)) are obtained from the experimental structure factor reported by Etherington et al ¹⁵⁰ for amorphous *Ge* and shown in fig. 3.23. From elastic constant data by Grimsditch et al ¹⁹¹ on amorphous *Si* we estimate $K_T(\text{amorphous}) \equiv$

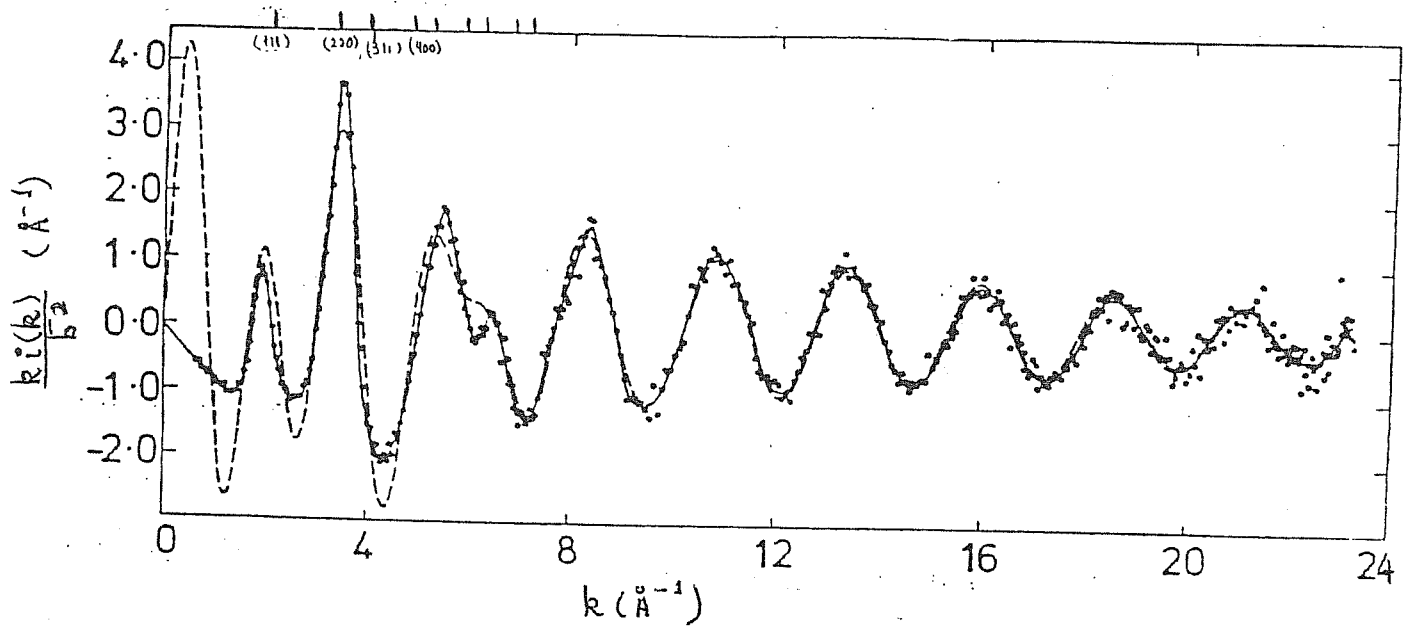


Figure 3.23: The reduced interference function $ki(k)/\bar{b}^2$. Dots are experimental data, full line is hand smoothed line and dashed curve is peak fit to the first two peaks in the total correlation function. The location of the first few allowed Bragg reflections from the diamond structure are superposed at the top. From ref.[191].

$(3 \div 2)K_T(\text{crystal})$ and assume that this is also approximately applicable for Ge , yielding K_T in the range $(4.6 \times 10^{-12} \div 3.1 \times 10^{-12})\text{cm}^2/\text{dyn}$.

Figure (3.23) shows the reduced interference function as measured by Etherington et al ¹⁵⁰ which is directly related to structure factor $S(k)$ [i.e. $S(k) = (i(k)/\bar{b}^2) + 1$] and the location of the first few allowed Bragg reflections from the diamond structure are superposed at the top of the figure. The first step in our calculations is to include the first three RLV stars [(111), (220) and (311)] using two different values of $\bar{c}(0)$ (the direct correlation function in the long-wavelength limit from our estimated range of K_T). Convergence has been achieved for the set of equations for the order parameters ρ_G 's which are tabulated in table (3.5) with the value of the volume change η . The difference in the grand potential $\Delta\Omega$ was negative, which indicates that the crystal is more stable when the disordered system has the assumed structure. The following observations can be made (i) the profile is very closely Gaussian; (ii) the values of the various ρ_G 's are close to 1, i.e. the mean square displacements are rather low; (iii) the value of $\eta = 0.0273 \div 0.0431$ is reasonable, since the density difference between compacted amorphous Ge and crystalline Ge is $\eta_{exp} \simeq 0.035$.

We have next enlarged the set of order parameters to include up to 9 stars, covering complete cycle in the structure factor. We find that

<i>Multiplicity</i>	<i>StarG</i>	<i>LengthA</i>	$S(k)$	$\bar{c}(k)$
8	111	1.923	1.410	0.291
12	220	3.141	1.520	0.342
24	311	3.683	1.510	0.338
6	400	4.440	0.614	- 0.602
24	331	4.840	0.800	- 0.250
24	422	5.440	1.330	0.248
8	333	5.770	1.123	0.110
12	440	5.280	1.034	0.033
48	531	6.570	1.011	0.011

Table 3.4: *The different values of the structure factor $S(k)$ and the direct correlation function $\bar{c}(k)$ at wave numbers corresponding to the various stars of RLV. As obtained from fig 3.23 (ref.[191]).*

we always get a solution for the order parameters ρ_G 's and η which are qualitatively reasonable, while the values of $\Delta\Omega$ is approaching zero. The star-dependent Lindemann ratio are somewhat larger but still essentially constant. The approximate vanishing of $\Delta\Omega$ in this calculation arises from a balance between (a) the order parameter at the fourth star, i.e. the (400) star, which corresponds to a trough in $\bar{c}(k)$ and hence disfavors crystallization, and (b) the order parameters at the other stars, which favour crystallization.

In conclusion, the main point that we should stress is that a one-component fluid system having the liquid structure of amorphous *Ge* would crystallize with a volume contraction, being essentially driven by the order parameters at the RLV stars that we have considered in dealing with the liquid-solid transition of the bond particle model in section (3.3) and (3.4). In particular, our present calculation gives support to the role that we have attributed there to the (111) star.

$\bar{c}(0) = -230.0$	$\eta = 0.0273$	$\bar{c}(0) = -150.0$	$\eta = 0.043$
$\rho_{\mathbf{G}(111)} = 0.977$	$L_{(111)} = 0.116$	$\rho_{\mathbf{G}(111)} = 0.994$	$L_{(111)} = 0.115$
$\rho_{\mathbf{G}(220)} = 0.906$	$L_{(220)} = 0.113$	$\rho_{\mathbf{G}(220)} = 0.923$	$L_{(220)} = 0.112$
$\rho_{\mathbf{G}(311)} = 0.865$ $\Delta\Omega = -0.55$	$L_{(311)} = 0.113$	$\rho_{\mathbf{G}(311)} = 0.880$ $\Delta\Omega = -0.60$	$L_{(311)} = 0.112$

Table 3.5: *The various parameters as calculated using two different choices of the $\bar{c}(0)$, when only the first three RLV were included in the calculations.*

SUMMARY

The main results of this work can be summarized as follows:

1) Freezing of the classical-one-component plasma on a rigid neutralizing background into bcc structure has been re-evaluated, within the recent progress in computer simulation for the thermodynamic properties of this model fluid. The value of the coupling parameter Γ_c at the phase transition is approximately the same as from previous calculation of Rovere and Tosi⁸⁰. The difficulties of the theory relating to the order parameter at the (200) star of reciprocal lattice vectors is also considered from two alternative point of view, namely (i) the fourier transform of the periodic crystalline density (the microscopic order parameter) at this star of RLV may be very small, or (ii) this order parameter may be driven by the others in particular those associated with the (110) star, and such a cooperative effect may be simulated by raising the value of the two-body direct correlation function at the (200) star to an effectively higher value.

The microscopic order parameters, excepting the (200) one, follow a Gaussian behaviour and yield Lindemann ratios in reasonable agreement with simulation results by Pollock and Hansen²³. The Lindemann ratio appropriate to the (200) star falls in the general pattern set by the others when the viewpoint (ii) is taken. Freezing of the OCP into the fcc structure is also considered and found to be unfavoured.

2) Freezing of an OCP on a deformable background (OCP-DB) into the bcc lattice has been evaluated by a parallel approach. The main qualitative changes which accompany the appearance of a finite volume change across the phase transition are (i) a decrease in the value of Γ_c , i.e. reduced stability of the fluid phase as first pointed by Pollock and Hansen²³, (ii) an increase in the entropy of melting and (iii) a narrowing of the single particle distribution around each lattice site in the hot solid.

3) Freezing of alkali metals as screened ionic plasmas has been evaluated, the freezing of the OCP-DB into the bcc lattice being our starting point. The consequences of the two alternative viewpoints in (1) above have been examined by asking which value of the order parameter, or alternatively of the two-body direct correlation function, would be compatible with a value of Γ_c lying in the range appropriate to alkali metals at standard pressure. Our results suggest that the phase transition in the alkali metals may also be assisted by some ordering in the conduction electrons, which is indicated by differences of X-ray and neutron scattering intensities from liquid *Na* as analysed by Dobson¹³⁹. However, the possibility also suggests itself that anharmonicity in hot crystal may appear as a premelting phenomenon through a rapid decrease of scattering intensity at the (200) Bragg diffraction

spots.

4) Freezing of bond-particle model for liquid germanium has been evaluated. The microscopic order parameters of the phase transition are the Fourier components of the periodic single-particle densities for atoms (ρ_{AG}) and bonds (ρ_{BG}) in the crystal. The location of the allowed Bragg reflections from the diamond structure (i.e. the (220) and (311) RLV stars) are in good correspondence with the main features in the partial structure factors of the bond-particle model. Thus the Fourier components of the periodic crystalline densities of the above RLV's describe "freezing of bonds" driven by tetrahedrally constrained attractions and leading to local tetrahedral coordination. The connectivity that such tetrahedral units have in the diamond structure is mainly described by the microscopic order parameters associated with the (111) star of RLV. We mainly infer this from the fact that the first sharp diffraction peak (FSDP) at a wave number in correspondence with the (111) RLV star is well developed in amorphous germanium. However, formation of such connectivity in the liquid is frustrated by its relatively high density. Hence, crystallization of the liquid into the diamond structure requires a volume expansion. On the contrary, crystallization of compact amorphous germanium is accompanied by volume contraction.

From a qualitative discussion, the main order parameters of the phase transition, in addition to the percentual density difference between solid and liquid at coexistence, are thus expected to be: a) charge waves at the (200) and (311) stars; and b) number density waves at the (111) star. Our quantitative calculations are consistent with a volume expansion across the transition from liquid to solid, in which density waves at the (111) star, atomic waves at the (220) star and charge density waves at the (311) star are spontaneously generated. However, the estimated Lindemann ratios that emerge from our calculations are rather large at least by comparison with typical values for monatomic system crystallizing in the fcc or bcc structures.

Finally, evaluation of freezing of a one-component fluid system having the liquid structure of amorphous germanium has also been considered. Crystallization is essentially driven by the order parameters at the (111), (220) and (311) RLV stars, and is accompanied by a volume contraction. Our calculation gives support to the role that we have attributed to the (111) star in the liquid-solid transition of the bond particle model.

Bibliography

- [1] F.A.Lindemann, Z. Physik **11** (1910) 609.
- [2] C. Kittel "Introduction To Solid State Physics" 5th ed. John Wiley and Sons Inc. N.Y. 1976.
- [3] J.M. Ziman "Principles Of The Theory Of Solids" 2nd ed. Cambridge 1972.
- [4] T.E. Faber "Theory Of Liquid Metals" Cambridge 1972.
- [5] J.N. Shapiro, Phys. Rev. **B 1** (1970) 3982.
- [6] D.K. Chaturvedi, M. Rovere, G. Senatore and M.P. Tosi, Physica **B 111** (1981) 11.
- [7] D.L. Martin, Phys. Rev. **A 139** (1965) 150.
- [8] H.M. Van Horn, Phys. Lett. **A 28** (1969) 706.
- [9] M. Ross, Phys. Rev. **184** (1969) 233.
- [10] W.G. Hoover, S.G. Gray and K.W. Johnson, J. Chem. Phys. **55** (1971) 1128.
- [11] J.P. Hansen and Loup Verlet, Phys. Rev. **184** (1969) 151.
- [12] J.P. Hansen and D. Shiff, Mol. Phys. **25** (1973) 1281.
- [13] Y. Waseda "The Structure Of Non-Crystalline Materials" (New York, McGraw-Hill 1980).
- [14] B.J. Alder and T.E. Wanwright, J. Chem. Phys. **27** (1957) 1208.
- [15] L.D. Landau and E.M. Lifshitz, "Statistical Physics", Pergamon Press, Oxford 1969.
- [16] T.H. Berlin and E. Montroll, J. Chem. Phys. **20** (1952) 75.
- [17] W.G. Hoover and M. Ross, Contemp. Phys. **12** (1971) 339.

- [18] A.J.C. Ladd and L.V. Woodcock, Chem. Phys. Lett. **51** (1977) 155
- [19] A.J.C. Ladd and L.V. Woodcock, Mol. Phys. **36** (1978) 611
- [20] W.B. Street, H.J. Raveche and R.D. Mountain, J. Chem. Phys. **61** (1974) 1960.
- [21] J.H. Hansen, Phys. Rev. A **2** (1970) 221.
- [22] J.H. Hansen, Phys. Rev. A **8** (1973) 3096.
- [23] E.L. Pollock and J.P. Hansen, Phys. Rev. A **8** (1973) 3110.
- [24] W.L. Slattery, G.D. Doolen and H.E. DeWitt, Phys. Rev. A **21** (1980) 2087.
- [25] W.L. Slattery, G.D. Doolen and H.E. DeWitt, Phys. Rev. A **26** (1982) 2255.
- [26] W.G. Hoover and F.H. Ree J. Chem. Phys. **49** (1968) 3609
- [27] J.L. Barrat and J.P. Hansen 'Nato Advanced Study Institute' ed. by A. Polian, P. Loubeyre and N. Boccara. (Plenum Press, New York, N.Y. 1989) NATO ASI Series B **V.186** pp491
- [28] J.D. Weeks, Phys. Rev. B **24** (1981) 1530.
- [29] F.R.N. Nabarro "Theory Of Crystal Dislocations", Clarendon Press, Oxford 1976.
- [30] S.F. Edwards and M. Warner, Phil. Mag. A **40** (1979) 257.
- [31] J.G. Kirkwood and E. Monroe, J. Chem. Phys. **9** (1941) 514.
- [32] M. Baus, Mol. Phys. **53** (1984) 183.
- [33] L. Feijoo and A. Rahman, J. Chem. Phys. **77** (1982) 5687.
- [34] S.V. Tyablikov, J. Exp. Theor. Phys. **17** (1947) 386.
- [35] A.A. Vlasov, J. Exp. Theor. Phys. **8** (1938) 291.
- [36] H.J. Raveché and C.A. Stuart, J. Chem. Phys. **63** (1975) 1099.
- [37] H.J. Raveché and R.F. Kayser, J. Chem. Phys. **68** (1978) 3632.
- [38] J.D. Weeks S.A. Rice and J.J. Kozak, J. Chem. Phys. **52** (1970) 2416.
- [39] B. Jancovici, Physica **31** (1965) 1017.

- [40] R. Lovett, *J. Chem. Phys.* **66** (1977) 1225.
- [41] R. Lovett and E.P. Buff, *J. Chem. Phys.* **72** (1980) 2425.
- [42] V.N. Ryzhov and E.E. Tareeva, *Theor. Math. Phys.* **48** (1981) 835.
- [43] B. Bagchi, C. Cerjan and S.A. Rice, *J. Chem. Phys.* **79** (1983) 5595.
- [44] C. De Dominicis, *J. Math. Phys.* **3** (1962) 983.
- [45] F.H. Stillinger and F.P. Buff, *J. Chem. Phys.* **37** (1962) 1.
- [46] J.L. Lebowitz and J.K. Percus, *J. Math. Phys.* **4** (1963) 116.
- [47] R. Evans, *Adv. Phys.* **28** (1979) 143.; P. Hohenberg and W. Kohn, *Phys. Rev. B* **136** (1964) 864; N.D. Mermin, *Phys. Rev. A* **137** (1965) 1441; W. Kohn and L.J. Sham, *Phys Rev. A* **140** (1965) 1133.
- [48] S. Lundqvist and N.H. March, "Theory Of Inhomogeneous Electron Gas" (New York, N.Y. Plenum Press 1983).
- [49] T.V. Ramakrishnan and M. Yussouff, *Solid State Comm.* **21** (1977) 389; and *Phys. Rev. B* **19** (1979) 2775.
- [50] A.D.J. Haymet and D.W. Oxtoby, *J. Chem. Phys.* **74** (1981) 2559.
- [51] N.H. March and M.P. Tosi, *Phys. Chem. Liquids* **11** (1981) 129.
- [52] G. Senatore and M.P. Tosi, *N. Cimento B* **56** (1980) 169.
- [53] R. Lovett, C.Y. Mou and E.P. Buff, *J. Chem. Phys.* **65** (1976) 570.
- [54] A.D.J. Haymet, *J. Chem. Phys.* **78** (1983) 4641.
- [55] A.J.M. Yang, P.D. Fleming and J.H. Gibbs, *J. Chem. Phys.* **64** (1976) 3732.
- [56] L.S. Ornstein and F. Zernike, *Proc. Akad Sci. (Amsterdam)* **17** (1914) 793.
- [57] E. Theile, *J. Chem. Phys.* **39** (1963) 474.
- [58] M.S. Wertheim, *Phys. Rev. Lett.* **10** (1963) 321; *J. Math. Phys.* **5** (1964) 643.
- [59] J.K. Percus and G.J. Yevick, *Phys Rev.* **110** (1958) 1.
- [60] M. Baus and J.L. Colot, *J. Phys. C:Sol. State Phys.* **18** (1985) L365; *Mol. Phys.* **55** (1985) 653.

- [61] J.L. Colot, M. Baus and Xu Hong, *Mol. Phys.* **57** (1986) 809.
- [62] F. Iglói and J. Hafner. *J. Phys.C:Sol. State Phys.* **19** (1986) 5799.
- [63] M. Baus, *J. Phys.: Condensed Matter* **1** (1989) 3131.
- [64] J.F. Lutsko and M. Baus 1989 to be published.
- [65] P. Tarazona. *Phys. Rev. A* **31** (1985) 2672.
- [66] W.A. Curtin and N.W. Ashcroft, *Phys. Rev. A* **32** (1985) 2909.
- [67] O. Gunnarsson, M. Jonson and B. I. Lundquist, *Phys. Rev. B* **20** (1979) 3136.
- [68] A.R. Denton and N.W. Ashcroft, *Phys. Rev. A* **39** (1989) 4701.
- [69] M. Baus, *J. Phys.: condensed Matter* **2** (1990) 2111.
- [70] J.L. Barrat, J.P. Hansen, G. Pastore and E.M. Waisman, *J. Chem. Phys.* **86** (1987) 6360.
- [71] P.R. Harrowell, D. W. Oxtoby and A.D.J. Haymet, *J. Chem. Phys.* **83** (1985) 6058.
- [72] A.D.J. Haymet and D.W. Oxtoby, *J. Chem. Phys.* **84** (1986) 1769.
- [73] L. Verlet and J.J. Weis, *Phys. Rev.* **45** (1972) 939.
- [74] W.G. Hoover, M. Ross, K.W. Johnson, D. Henderson, J.A. Barker and B.C. Brown, *J. Chem. Phys.* **52** (1970) 4931.
- [75] S.G. Brush, H.L. Sahlin and E. Teller, *J. Chem. Phys.* **45** (1966) 2102.
- [76] H.E. De Witt, W.L. Slattery, G.S. Stringfellow, *Proc. Int. Yamada Conf. XXIV on " Strongly Coupled Plasma Physics"* (1989), in press.
- [77] H.M. van Horn, *Phys. Lett A* **28** (1969) 706.
- [78] B. Bagchi, C. cerjan, U. Mohanty and S.A. Rice, *Phys. Rev. B* **29** (1984) 2857.
- [79] A.D. Haymet, *Phys. Rev. Lett.* **52** (1984) 1013.
- [80] M. Rovere, and M.P. Tosi, *J. Phys. C:Sol. State Phys.* **18** (1985) 3445.
- [81] M. Rovere, G. Senatore and M.P. Tosi, " Progress on Electron of Solids" eds. R. Girlanda et al. (1989) 221-238.

- [82] M.P. Tosi, *Solid State Physics* **16** (1964) 1 (New York: Academic), appendix A and references given therein.
- [83] J.L. Barrat, *Europhysics Letters*. **3** (1987) 523.
- [84] J.L. Barrat, J.P. Hansen and G. Pastore, *Mol. Phys.* **63** (1988) 747.
- [85] C. Marshall, B.B. Laird and A.D.J. Haymet, *Chem. Phys. Lett.* **122** (1985) 320.
- [86] W.A. Curtin and N.W. Ashcroft, *Phys. Rev. Lett.* **56** (1986) 2775.
- [87] J.L. Barrat, M. Baus and J.P. Hansen, *Phys. Rev. Lett.* **56** (1986) 1063.
- [88] M. Rovere and M.P. Tosi, *Rep. Prog. Phys.* **49** (1986) 1001.
- [89] N.H. March and M.P. Tosi, *Phys. Chem. Liquids* **10** (1980) 185.
- [90] B.D'Aguanno, M. Rovere, M.P. Tosi and N.H. March, *Phys. Chem. Liquids* **13** (1983) 113.
- [91] N.H. March and M.P. Tosi, *Phys. Chem. Liquids* **11** (1981) 79.
- [92] N.H. March and M.P. Tosi, *Phys. Chem. Liquids* **11** (1981) 129.
- [93] A.B. Bahatya, N.H. March and M.P. Tosi, *Phys. Chem. Liquids* **9** (1980) 229.
- [94] B. D'Aguanno Ph.D. Thesis 1983/1984 International School For Advanced Studies. Trieste, Italy.
- [95] L.J. Barrat, *J. Phys. C:Sol. State Phys.* **20** (1987) 1031.
- [96] L.J. Barrat, M. Baus and J.P. Hansen, *J. Phys. C:Sol. State Phys.* **20** (1987) 1413.
- [97] R.L. McGreevy and E.W.J. Mitchell, *J. Phys. C:Sol. State Phys.* **15** (1982) 5537.
- [98] G. Pastore, P. Ballone and M.P. Tosi, *J. Phys. C:Sol. State Phys.* **19** (1986) 487.
- [99] S.W. de Leeuw, *Mol. Phys.* **36** (1978) 765.
- [100] N.H. March and M.P. Tosi, *Phys. Chem. Liquids* **11** (1981) 89.
- [101] M. Rovere and M.P. Tosi, *Sol. State Comm.* **55** (1985) 1109.
- [102] D.L. Micheal, S.A. Rice And U. Mohanty, *J. Chem. Phys.* **82** (1985) 472.

- [103] T.V. Ramakrishnan, *Pramāna* **22** (1984) 365.
- [104] Y. Singh, *Phys. Rev. A* **30** (1984) 583.
- [105] M. Baus and J.P. Hansen, *Phys. Rep.* **59** (1980) 1.
- [106] H. Minoo, C. Deutsch and J.P. Hansen, *J. Phys. (Paris)* **38** (1977) L191.
- [107] D.K. Chaturvedi, G. Senatore and M.P. Tosi, *Lett. N. Cimento* **30** (1981) 47.
- [108] F. Postogna and M.P. Tosi, *N. Cimento* **55 B** (1980) 399.
- [109] D.K. Chaturvedi, G.Senatore and M.P. Tosi, *N. Cimento* **62 B** (1981) 375.
- [110] D. Pines and P. Nozières, “ *The Theory Of Quantum Liquids*”, Benjamin, New York, 1966.
- [111] N.W. Ashcroft, *J. Phys. C:Sol. State Phys.* **1** (1968) 232.
- [112] D.L. Price, K.S. Singwi and M.P. Tosi, *Phys. Rev. B* **2** (1970) 2983.
- [113] K.S. Singwi, A. Sjölander, M.P. Tosi and R.H. Land, *Phys. Rev. B* **1** (1970) 1044.
- [114] A.J. Greenfield, J. Wellendorf and N. Wiser, *Phys. Rev. A* **4** (1971) 1607.
- [115] G.M.B. Webber and R.W.B. Stephens, in: *Physical Acoustic, Vol IVB*, W.P. Mason ed. (Academic Press, New York, 1968) P.53.
- [116] M. Hasegawa and M. Watabe, *J. Phys. Soc. Japan* **32** (1972) 14.
- [117] G. Pastore and M.P. Tosi, *Physica B* **124** (1984) 383.
- [118] J.D. Weeks, D. Chandler and H.C. Andersen, *J. Chem. Phys.* **54** (1971) 5237; H.C. Andersen, D. Chandler and J.D. Weeks, *J. Chem. Phys.* **56** (1972) 3812.
- [119] M.J. Huijben and W. van der Lugt, *Acta Cryst. A* **35** (1979) 431.
- [120] P. Vashishta and K.S. Singwi, *Phys. Rev. B* **6** (1972) 875; and 4883.
- [121] C.J. Smithells, “*Metals Reference Handbook*”, 5th edition (Butterworth, London, 1978).
- [122] S. Galam and J.P. Hansen, *Phys. Rev. A* **14** (1976) 816.

- [123] M. Ross, H.E. De Witt and W.B. Hubbard, *Phys. Rev. A* **24** (9181) 1016.
- [124] K.K.Mon, R. Gann and D. Stroud, *Phys. Rev. A* **24** (1981) 2145.
- [125] W.H. Young, *J. Phys. F: Met. Phys.* **12** (1982) L19.
- [126] N. Montella, G. Senatore and M.P. Tosi, *Physica B* **124** (1984) 22.
- [127] D.L. Price, *Phys. Rev. A* **4** (1971) 358.
- [128] M. Iwamatsu, R.A. Moore and S. Wang, *Phys. Lett. A* **101** (1984) 97.
- [129] S.N. Khanna and F. Cyrot-Lackman, *J. Physique Lett.* **40** (1979) L45.
- [130] T. Itami and M. Shimoji, *J. Phys. F.:Met. Phys.* **14** (1984) L15.
- [131] C. Ebner, W.F. Saam, and D. Stroud, *Phys. Rev. A* **14** (1976) 2264; W.F. Saam, and C. Ebner, *Phys. Rev. A* **15** (1977) 2566.
- [132] J.P. Hansen and I.R. McDonald “ Theory Of Simple Liquids”, London Academic Press, 1976.
- [133] R. Balescu, “ Equilibrium And Non Equilibrium Statistical Mechanics” (Wiley, 1975).
- [134] B. D’Aguanno, M. Rovere and G. Senatore, *Phys. Chem. Liquids* **16** (1987) 157.
- [135] T.V. Ramakrishnan, *Phys. Rev. Lett.* **48** (1982) 541.
- [136] J.L. Tallon, *Phys. Lett. A* **87** (1982) 361.
- [137] P.M. Morse and H. Feshbach “ Methods Of Theoretical Physics” (McGraw Hill 1953) ch.4.
- [138] H.E. De Witt, *Phys. Rev. A* **14** (1976) 1290.
- [139] P.J. Dobson, *J. Phys. C.: Sol. State Phys.* **11** (1978) L295.
- [140] P.A. Egelstaff, N.H. March and N.C. McGill **52** (1974) 1651.
- [141] Z. Badirkhan, M. Rovere and M.P. Tosi, To be published.
- [142] W. Anderioni, *Helv. Phys. Acta* **58** (1985) 226.
- [143] J.C. Phillips, *Sol. Stat. Comm.* **22** (1977) 549.
- [144] S. Sugai, *Phys. Rev. B* **35** (1987) 1345.

- [145] D.L. Price and J.M. Carpenter, *J. Non-Cryst. Solids* **92** (1987) 153; J.M. Carpenter and D.L. Price, *Phys. Rev. Lett.* **54** (1985) 441.
- [146] S.C. Moss and D.L. Price: in "Physics Of Disordered Materials" ed. by D. Alder, H. Fritzsche and S.R. Ovshinsky, Plenum Press, New York, N.Y. 1985. P77.
- [147] S. Biggin and J.E. Enderby, *J. Phys. C* **14** (1981) 3129; J.A.E. Desa, A.C. Wright, J. Wong and R.N. Sinclair, *J. Non-Cryst. Solids* **51** (1982) 57.
- [148] S. Susman, D.G. Montague, D.L. Price and K.J. Volin: in the course of publication.
- [149] T.A. Postol, C.M. Falco, R.T. Kampwirth, I.K. Schuller and Y.B. Yelon, *Phys. Rev. Lett.* **45** (1980) 648.
- [150] G. Etherington, A.C. Wright, J.T. Wenzel, J.C. Dore, J.H. Clarke and R.N. Sinclair, *J. Non-Cryst. Solids* **48** (1982) 265.
- [151] Y. Waseda and K. Suzuki, *Z. Phys. B* **20** (1975) 339; J.P. Gabathuler and S. Steeb, *Z. Naturforsch A* **34** (1979) 1314.
- [152] V.M. Glazov, S.N. Chizheskaya and N.N. Glagoleva, "Liquid Semiconductors" Plenum Press, New York, N.Y. 1969.
- [153] P.S. Salmon, *J. Phys. F: Metal Phys.* **18** (1988) 2345.
- [154] C. Bergman, C. Bichara, P. Chieux and J. Gaspard, *J. Phys. (Paris)* **21** (1985) C8-97.
- [155] R. Car and M. Parrinello, *Phys. Rev. Lett.* **60** (1988) 204; I. Stich, R. Car and M. Parrinello, *Phys. Rev. Lett.* **63** (1989) 2240.
- [156] G. Galli, R.M. Martin, R. Car and M. Parrinello, *Phys. Rev. Lett.* **62** (1989) 555.
- [157] J. Hafner and G. Kahl, *J. Phys. F* **14** (1984) 2259; W. Jank and J. Hafner, *Europhys. Lett.* **7** (1988); A. Arnold, N. Mauser and J. Hafner, *J. Phys. Condensed Matter* **1** (1989) 965.
- [158] F.H. Stilinger and T.A. Weber, *Phys. Rev. B* **31** (1985) 5262.
- [159] M.D. Kluge, J. Ray and A. Rahman, *Phys. Rev. B* **36** (1987) 4234.
- [160] W.D. Luedtke and U. Landman, *Phys. Rev. B* **37** (1988) 4656.
- [161] P. Vashishta, R.K. Kalia, G.A. Antonio and I. Ebbsjo, *Phys. Rev. Lett.* **62** (1989) 16561.

- [162] P. Ballone, G. Pastore, J.S. Thakur and M.P. Tosi, *Physica B* **142** (1986) 294.
- [163] R.L. McGreevy, *Solid State Phys.* **40** (1987) 247.
- [164] H. Iyetomi and P. Vashishta, *J. Phys. Condensed Matter* **1** (1989) 1679.
- [165] W.R. Smith and I. Nezbeda, *J. Chem. Phys.* **81** (1984) 3694.
- [166] J. Kolafa and I. Nezbeda, *Mol. Phys.* **61** (1987) 161.
- [167] M.S. Wertheim, *J. Chem. Phys.* **88** (1988) 1145.
- [168] A. Ferrante and M.P. Tosi, *J. Phys. Condensed Matter* **1** (1989) 1679.
- [169] J.C. Phillips, "Covalent Bonding In Crystals And Molecules" University of Chicago Press, Chicago Ill 1970.
- [170] J.C. Phillips, *Phys. Rev. Lett.* **19** (1967) 415; *Phys. Rev.* **166** (1968) 832; *Phys. Rev.* **168** (1968) 905, *Phys. Rev.* **168** (1968) 917.
- [171] J.C. Phillips, "Bonds And Bands In Semiconductors", Academic Press N.Y. 1973.
- [172] R.M. Martin, *Phys. Rev. Lett.* **21** (1968) 536. *Phys. Rev.* **186** (1969) 871.
- [173] W. Weber, *Phys. Rev. Lett.* **33** (1974) 371; *Phys. Rev. B* **15** (1977) 4789.
- [174] W.Cochran, *Proc. Royal Soc. A* **253** (1959) 260.
- [175] See for example, F. Herman, *J. Phys. Chem. Sol. Suppl.* **8** (1959) 405.
- [176] D.R. Penn, *Phys. Rev.* **128** (1962) 2093.
- [177] A. Goldberg, M. El- Batanouny and F. Wooten, *Phys. Rev. B* **26** (1982) 6661.
- [178] K. Winer and F. Wooten, *Phys. Stat. Sol. (b)* **136** (1986) 519.
- [179] J.P. Waller and M.L. Cohen, *Phys. Rev. B* **4** (1971) 1877.
- [180] A.R. Ubbelhode, "The Molten State Of Matter" Chichester, Wiley 1978.
- [181] G. Zerah and J.P. Hansen, *J. Chem. Phys.* **84** (1986) 2336.
- [182] M.P. Tosi, *Phys. Scr.* **T29** (1989) 277.

- [183] Z. Badirkhan, A. Ferrante, M. Rovere and M.P. Tosi, *Il Nuovo Cimento D* **12** (1990) 619.
- [184] J.P. Gabathuler and S. Steeb, *Z. Naturf. A* **34** (1979) 1314.
- [185] T. Iida and R.I.L. Guthrie, "The Physical Properties Of Liquid Metals", Clarendon Press, Oxford 1988.
- [186] V.M. Glasov A.A. Aivazov and V.I. Timoshenkov, *Sov. Phys.-Solid State* **18** (1976) 684.
- [187] F.J. Pearson and G.S. Rushebrooke, *Proc. Roy. Soc. Edinburgh A* **64** (1957) 305.
- [188] A.B. Bahatia and D.E. Thornton, *Phys. Rev. B* **2** (1970) 3004.
- [189] See for instance R.W.G. Wyckoff, "Crystal Structure" Vol 1, Interscience, New York, N.Y. 1963.
- [190] B. Stenhouse, P.J. Grout, N.H. March and J.Wenzel, *Phil. Mag.* **36** (1977) 129.
- [191] M. Grimsditch, W. Senn and G. Winterling, M.H. Brodsky, *Sol. Stat. Comm.* **26** (1978) 229.

ACKNOWLEDGEMENTS

I wish to express my appreciation to my supervisor, Prof. M.P. Tosi for his guidance and fruitful discussion throughout these years that led this thesis into conclusion.

It is my pleasure to thank Dr. G. Pastore, Dr. M. Rovere and Prof. G. Senatore for constructive discussions.

I would also like to thank all my colleagues in particular Dr. A. Ferrante for various discussions.

Thanks go to Daniela, Alex and Rosanna for the friendly atmosphere they created.

Finally, I should not forget to thank my family for their encouragement and continuous support.

